

TRANSIENT AXISYMMETRIC MODEL FOR LASER DRILLING

by

Sirilath Jayaman DeSilva

A Dissertation Submitted to the Faculty of the

DEPARTMENT OF AEROSPACE AND MECHANICAL ENGINEERING

**In Partial Fulfillment of the Requirements
For the Degree of**

**DOCTOR OF PHILOSOPHY
WITH A MAJOR IN MECHANICAL ENGINEERING**

In the Graduate College

THE UNIVERSITY OF ARIZONA

2003

UMI Number: 3106978

UMI[®]

UMI Microform 3106978

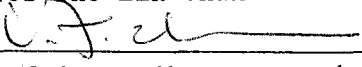
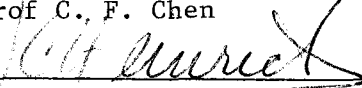
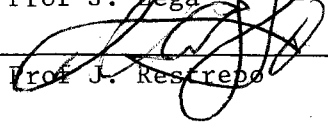
Copyright 2004 by ProQuest Information and Learning Company.
All rights reserved. This microform edition is protected against
unauthorized copying under Title 17, United States Code.

ProQuest Information and Learning Company
300 North Zeeb Road
P.O. Box 1346
Ann Arbor, MI 48106-1346

THE UNIVERSITY OF ARIZONA ©
GRADUATE COLLEGE

As members of the Final Examination Committee, we certify that we have read the dissertation prepared by Sirilath Jayaman DeSilva entitled TRANSIENT AXISYMMETRIC MODEL FOR LASER DRILLING

and recommend that it be accepted as fulfilling the dissertation requirement for the Degree of Doctor of Philosophy

	<u>8/13/03</u>
Prof. Cho Lik Chan	Date
	<u>7/24/03</u>
Prof. C. F. Chen	Date
	<u>7/18/03</u>
Prof. J. C. Heinrich	Date
	<u>8/8/03</u>
Prof. J. Lega	Date
	<u>8/11/03</u>
Prof. J. Restrepo	Date

Final approval and acceptance of this dissertation is contingent upon the candidate's submission of the final copy of the dissertation to the Graduate College.

I hereby certify that I have read this dissertation prepared under my direction and recommend that it be accepted as fulfilling the dissertation requirement.

	<u>8/13/03</u>
Dissertation Director Prof. Cho Lik Chan	Date

STATEMENT BY AUTHOR

This dissertation has been submitted in partial fulfillment of requirements for an advanced degree at The University of Arizona and is deposited in the University Library to be made available to borrowers under rules of the Library.

Brief quotations from this dissertation are allowable without special permission, provided that accurate acknowledgement of source is made. Requests for permission for extended quotation from or reproduction of this manuscript in whole or in part may be granted by the head of the major department or the Dean of the Graduate College when in his or her judgement the proposed use of the material is in the interests of scholarship. In all other instances, however, permission must be obtained from the author.

SIGNED: _____

A handwritten signature in cursive script, appearing to read "S. de Silva", is written over a horizontal line.

ACKNOWLEDGEMENTS

The research project was funded by the Raytheon Corporation as part of the wider laser-material interaction study commissioned by the Department of Defense. Their financial support is greatly appreciated. Apart from that the periodic evaluation and the guidance with regard to the general direction of the project were of great help. As for the people who directly contributed to the success of this work and also played key roles, I would like to acknowledge the following.

I am immensely thankful to Prof. Cho Lik Chan, my major advisor, for all the help, advice and support he has given me in all these past years. His guidance in the technicalities of the project and other insights into the characteristics of laser drilling and its modeling were invaluable and therefore highly appreciated.

I am very grateful to the members of the final examination committee, Prof Chuan. Chen, Prof Juan Heinrich, Prof Joceline Lega and Prof Juan Restrepo, for all the helpful suggestions and guidance given towards the development of this thesis. I am also very thankful for all the valuable time they found from their busy schedules to be in the committee and for their contributions.

I am also very thankful for the oversight and helpful suggestions of Andrew Paul and David Campbell of Raytheon Corporation, who were the grant monitors representing the company.

Finally, and not the least, I would like to thank my mother and brothers and also my friends and well wishers who encouraged and supported me all through these years.

At the end of this acknowledgment, I would like to think of endurance, fortitude and strength that were brought to bear during this arduous task for which I am very grateful for the Providential guidance.

TABLE OF CONTENTS

LIST OF FIGURES	8
LIST OF TABLES	12
ABSTRACT	13
1.0 INTRODUCTION	14
2.0 MATHEMATICAL FORMULATION	25
2.1 Conduction model	26
2.2 Thin layer model	28
2.2.1 Governing equations for the thin layer	29
3.0 NUMERICAL FORMULATION	42
3.1 Conduction formulation	43
3.1.1 BEM formulation	44
3.1.2 FDM formulation	49
3.1.3 Time marching scheme for FDM	54
3.2 Space-Time method for the thin layer equations	56
3.2.1 Boundary conditions for the Space-Time formulation	62
4.0 RESULTS FROM SIMULATIONS	65
4.1 Simulation for the conduction regime	66
4.1.1 Test with a constant heat flux	66
4.1.1.1 Constant heat flux – simulation 1	67
4.1.1.2 Constant heat flux – simulation 2	69
4.1.2 Test with a variable heat flux	74

TABLE OF CONTENTS – Continued

4.1.2.1 Variable heat flux – simulation 1	74
4.1.2.2 Variable heat flux – simulation 2	81
4.1.2.3 Variable heat flux – simulation 3	86
4.3 Convergence test for the conduction regime	91
4.3.1 Convergence test for the BEM-FDM coupled model	91
4.3.2 Convergence test for the BEM model	93
4.3.3 Convergence test for the FDM model	95
4.4 CPU time comparison	98
4.5 Moving boundary simulation	99
4.6 Thin layer simulation	101
4.6.1 Laser power level 1	103
4.6.2 Laser power level 2	106
4.6.3 Laser power level 3	109
4.7 Comparison with 1-D model	111
4.8 Convergence test for the Space-Time method	112
5.0 CONCLUSION AND FUTURE WORK	115
5.1 Conclusion	115
5.2 Future work	118
APPENDIX A	120
APPENDIX B	139
APPENDIX C	143

TABLE OF CONTENTS – Continued

APPENDIX D	145
NOMENCLATURE	149
REFERENCES	152

LIST OF FIGURES

Figure 2.1	Schematic diagram for laser drilling	25
Figure 2.2	Schematic diagram for conduction model	27
Figure 2.3	Thin layer geometric profile	30
Figure 2.4	Thin layer schematic diagram	36
Figure 3.1	BEM and FDM domain decomposition	43
Figure 3.2	Schematic diagram for the conduction regime	44
Figure 3.3	SEs and CEs of space-time grid	59
Figure 4.1	Configuration for the conduction region	66
Figure 4.2	Temperature profile: constant heat flux – simulation 2, level 1	71
Figure 4.3	Relative error – BEM: constant heat flux – simulation 2, level 1	71
Figure 4.4	Relative error – FDM: constant heat flux – simulation 2, level 1	72
Figure 4.5	Temperature profile: constant heat flux – simulation 2, level 2	73
Figure 4.6	Relative error – BEM: constant heat flux – simulation 2, level 2	73
Figure 4.7	Relative error – FDM: constant heat flux – simulation 2, level 2	74
Figure 4.8	Relative error: variable heat flux – simulation 1 level 1, $t = 0.025s$	76
Figure 4.9	Relative error: variable heat flux – simulation 1 level 2, $t = 0.025s$	77
Figure 4.10	Relative error: variable heat flux – simulation 1 level 3, $t = 0.025s$	77
Figure 4.11	Relative error: variable heat flux – simulation 1 level 1, $t = 0.5s$	78
Figure 4.12	Relative error: variable heat flux – simulation 1 level 2, $t = 0.5s$	78
Figure 4.13	Relative error: variable heat flux – simulation 1 level 3, $t = 0.5s$	79
Figure 4.14	Relative error: variable heat flux – simulation 1 level 1, $t = 1.0s$	79

LIST OF FIGURES – Continued

Figure 4.15	Relative error: variable heat flux – simulation 1 level 2, $t = 1.0s$	80
Figure 4.16	Relative error: variable heat flux – simulation 1 level 3, $t = 1.0s$	80
Figure 4.17	Relative error: variable heat flux – simulation 2 level 1, $t = 0.025s$	81
Figure 4.18	Relative error: variable heat flux – simulation 2 level 2, $t = 0.025s$	82
Figure 4.19	Relative error: variable heat flux – simulation 2 level 3, $t = 0.025s$	82
Figure 4.20	Relative error: variable heat flux – simulation 2 level 1, $t = 0.5s$	83
Figure 4.21	Relative error: variable heat flux – simulation 2 level 2, $t = 0.5s$	83
Figure 4.22	Relative error: variable heat flux – simulation 2 level 3, $t = 0.5s$	84
Figure 4.23	Relative error: variable heat flux – simulation 2 level 1, $t = 1.0s$	84
Figure 4.24	Relative error: variable heat flux – simulation 2 level 2, $t = 1.0s$	85
Figure 4.25	Relative error: variable heat flux – simulation 2 level 3, $t = 1.0s$	85
Figure 4.26	Temperature profile: variable heat flux – simulation 3 level 1	88
Figure 4.27	Relative error – BEM: variable heat flux – simulation 3 level 1	88
Figure 4.28	Relative error – FDM: variable heat flux – simulation 3 level 1	89
Figure 4.29	Relative error – BEM: variable heat flux – simulation 3 level 2-3	90
Figure 4.30	Relative error – FDM: variable heat flux – simulation 3 level 2-3	90
Figure 4.31	Convergence for constant flux BEM-FDM model at $r = 0.0$ m	92
Figure 4.32	Convergence for constant flux BEM-FDM model at $r = 0.1$ m	92
Figure 4.33	Convergence for constant flux BEM-FDM model at $r = 0.2$ m	93
Figure 4.34	Convergence for constant flux BEM model at $r = 0.0$ m	94

LIST OF FIGURES – Continued

Figure 4.35	Convergence for constant flux BEM model at $r = 0.1$ m	94
Figure 4.36	Convergence for constant flux BEM model at $r = 0.2$ m	95
Figure 4.37	Convergence for constant flux FDM model at $r = 0.0$ m ; $\Delta t = 5E-5$	96
Figure 4.38	Convergence for constant flux FDM model at $r = 0.1$ m; $\Delta t = 5E-5$	96
Figure 4.39	Convergence for constant flux FDM model at $r = 0.2$ m; $\Delta t = 5E-5$	97
Figure 4.40	Convergence for constant flux FDM model at $r = 0.1$ m; $\Delta t = 5E-6$	97
Figure 4.41	Configuration for the moving boundary	99
Figure 4.42	Moving boundary profiles	101
Figure 4.43	Temperature – Laser power level 1	103
Figure 4.44	Layer thickness part 1 – Laser power level 1	104
Figure 4.45	Layer thickness part 2 – Laser power level 1	105
Figure 4.46	Lateral velocity – Laser power level 1	105
Figure 4.47	Drilling velocity – Laser power level 1	106
Figure 4.48	Temperature – Laser power level 2	107
Figure 4.49	Layer thickness – Laser power level 2	107
Figure 4.50	Lateral velocity – Laser power level 2	108
Figure 4.51	Drilling velocity – Laser power level 2	108
Figure 4.52	Temperature – Laser power level 3	109
Figure 4.53	Layer thickness - Laser power level 3	110
Figure 4.54	Lateral velocity – Laser power level 3	110

LIST OF FIGURES – Continued

Figure 4.55	Drilling velocity – Laser power level 3	111
Figure 4.56	Convergence for φ_1 at $r = 0.2$ - Space-Time method	114
Figure 4.57	Convergence for φ_2 at $r = 0.2$ - Space-Time method	114
Figure A.1	Nodes and elements for the computation of BEM coefficients	124

LIST OF TABLES

Table 4.1	Constant flux simulation $t = 0.025$	68
Table 4.2	Constant flux simulation $t = 0.5$	68
Table 4.3	Constant flux simulation $t = 1.0$	68
Table 4.4	CPU time comparison for different methods	99
Table 4.5	Moving boundary simulation time = 0.01s	100
Table 4.6	Moving boundary simulation time = 0.03s	100
Table 4.7	Comparison of 1-D and 2-D laser drilling models	111

ABSTRACT

A transient axisymmetric model is developed to study the laser drilling phenomenon. Governing equations are the transient axisymmetric 3-D heat conduction equation for the solid substrate and for the liquid molten part, the thin layer model (TLM) equations are utilized. Boundary element method (BEM) is used for the region encompassing the moving boundary and finite difference method (FDM) is utilized for the remainder. BEM and FDM are coupled using flux and temperature at their interface. TLM is obtained using simplified free surface, mass, momentum and energy equations in body intrinsic coordinates. They are simplified by integrating across the layer using profiles for velocity and temperature thus obtaining a 1-D transient hyperbolic system. This is solved by a space-time flux conservation method. The TLM is coupled to the BEM-FDM by the common interface matching conditions. The constitutive equations governing laser interaction with material are used at the liquid-vapor interface.

1.0 INTRODUCTION

The usage of lasers in the material forming process has been a rapidly growing area in the manufacturing technology. Out of these many areas, drilling occupies a particularly distinctive advantage as given by Bass [1983]. This is basically due to the fact that laser drilling is a non-contact process, which allows it to be done from a distance. The other important aspect is that the location of the hole could be done with great precision and could be done at an angle to the surface being drilled, which would be impossible with mechanical drilling methods. The other important advantages are that the holes could be drilled very quickly, and with aspect ratios of depth to diameter that range up to 100:1 are attainable; and the diameters could range from 0.2 μm or less to 1.5 mm. In the laser drilling, material is removed due to vaporization and melt ejection thus the chip production problems which occurs in the mechanical drilling process are avoided. There are certain limitations to laser drilling. Mainly, it could be done only for limited depth, which typically is up to 13 mm for 0.2-0.7 mm diameter holes. For depths greater than 250 μm , a taper in the hole would be produced that can not be corrected by changing the profile of the laser beam. The other disadvantages are the wall roughness and uneven lip of the hole due to resolidified material. Laser drilling also depends on the thermal diffusivity and absorptivity of the material and these could act to limit the aspect ratio of the hole. Considering all the above advantages and limitations it is apparent that laser drilling occupies a very important niche in material processing. It could be utilized for

remote precision drilling where speed, automation and very small hole diameter are the important criteria.

In the process of laser drilling, an intense pulsed laser light is irradiated on the surface of a solid target, which is usually stationary or can be considered quasi stationary compared to the pulse length. At the beginning of the laser pulse, the absorbed laser energy will heat up the substrate to the melting point and subsequently to vaporization temperature. At higher intensities and also for sublimating material the mechanism of drilling would be by vaporization. At very low intensities the energy would basically go to melting the substrate. The pulse length also plays an important role in the interaction of the material with the laser. At very low pulse length around picosecond range the classical heat transfer mechanisms do not apply due to the fact that it approaches the time scale of the mean free path of electrons in a conductor (Bass [1983]). In the present study the intensities are in the range of $\sim 10 \text{ GW/m}^2$ and minimum pulse length in the range of \sim nanosecond. Depending on the intensity and temporal pulse shape of the laser power, vaporization can occur within a small fraction of the pulse duration. Because of the vapor pressure (often referred to as recoil pressure), the vapor is pushed away from the target. At the same time, this recoil pressure also exerts a force on the liquid and expels it side ways. Thus the material is removed from the target both in vapor and liquid forms. The absorbed laser energy is partitioned into: (1) lost into the substrate, (2) latent heat of fusion and vaporization, and (3) energy carried away by the ejection of vapor and liquid.

Considering the previous work in this area, Ready [1965] did a formulation where the material removal was done by vaporization. In his 1-D transient model, the energy from the laser beam is balanced by the heat lost in the substrate due to conduction and latent heat of vaporization. Similarly Hassanein et al [1984] did a 1-D transient model where the material removal was done by vaporization in a vacuum. Allmen [1976] did a 1-D steady state model where the material was removed by vaporization and liquid expulsion. His model accounted for steady state heat transfer, vaporization of the material and the ejection of the liquid that was calculated by volume work. Modeling material removal by vaporization in evaporation controlled limit, Andrews et al [1975] developed a 1-D steady state model to simulate laser material interaction in the drilling process. Afanas'ev et al [1967] similarly developed a 1-D model where the vapor phase momentum was modeled using gas dynamics and an energy balance was implemented across the Knudsen layer. This layer in the gaseous region, characterized by a couple of mean free path lengths in extent from the liquid-vapor interface, is not in local equilibrium due to the anisotropic velocity distribution. Therefore, the continuum hypothesis does not apply in this layer and it behaves as a discontinuity and a shock front requiring special treatment. This model was able to compute the pressure jump across the Knudsen layer and the flow of the vapor. Anisimov [1968] using Mott-Smith solution computed temperature, pressure and density discontinuities across the Knudsen layer in a vacuum. His use of this method is understandable, as the Knudsen layer acts as a shock front. The Mott-Smith solution is basically a method that has been successfully used to solve kinetic equation in the study of shock wave structure with the use of approximations to the gas phase

distribution functions within the discontinuity of the shock front. In the same manner Anisimov et al [1973] using kinetic theory and BGK method computed temperature, pressure and density discontinuities across the Knudsen layer in a vacuum. The BGK method (Bhatnagar, Gross, Krook [1954]) is used to capture the basic characteristics of the kinetic equation with the Boltzman collision term so that it could be evaluated with less computational expense. Similarly Knight [1979] did a 1-D steady state Mott-Smith solution for vapor flow to compute physical quantities across the Knudsen layer as a function of the Mach number.

Considering some of the recent work that have a direct bearing on this present work, Chan and Mazumder [1987] formulated a one-dimensional steady state model for laser drilling. In their work the Knudsen layer is modeled by a Mott-Smith type solution and the material is removed both as vapor and as liquid due to recoil pressure from the vaporization process. They incorporated the material removal rates in the immobilization transformation for the moving boundary. The results of vaporization rate, liquid-expulsion rate, surface temperature and the Mach number for different power levels and material were obtained. Chan [1997] investigated the material removal mechanism by Langmuir's theory, diffusion controlled vaporization model and convection dominated vaporization model in a 1-D steady state laser drilling model. He observed that for most material removal processes, the bulk flow motion driven by the pressure difference given by the convection dominated model, is the primary mechanism of vapor removal. It was also seen that the Langmuir theory predication for material removal was close to that of the convection dominated model even though the surface temperature predicted by it was

higher. Chan [1999] developed a transient one-dimensional model with variable properties. In this model all the material properties are dependent on temperature. It is a model, that combined three physical domains namely solid, liquid and vapor. Boundary immobilization transformation is used in the governing equations due to the moving boundaries. Clausius-Clapeyron equation is used to relate the saturation temperature and pressure right after vaporization and before the Knudsen layer and ideal gas law is assumed. The extended non-equilibrium vaporization model of Anisimov done by Knight [1979] is used to model the density and temperature discontinuity. This model was done for finite thickness of the material and it was an improvement over the constant property case.

The present work represents an ongoing effort to extend the previous one-dimensional models (Chan [1999] and Chan and Mazumder [1987]) to an axisymmetric model. In this work, first the modeling of the conduction region with the moving boundary at the melting interface that accounts for the solid substrate is presented. The solid substrate was modeled using the transient heat conduction equation in cylindrical axisymmetric coordinates. The numerical formulation was developed using a coupled boundary element method (BEM) and a finite difference method (FDM). BEM is known for its direct formulation and accuracy when dealing with complex and moving boundaries while FDM is known for its efficiency in computation. The limitation of BEM is in its inherent computational intensive nature that requires a lot of CPU time for large domains. The fact that it being an integral method which uses the free space Green's function obtained from the auxiliary equation to the transient heat conduction equation

also creates a limitation. As the physical parameter of thermal diffusivity in the Green's function has to be a constant, this necessitates that for accuracy of the BEM formulation, the region that it is applied should be restricted where this limitation to a high degree is valid. Therefore taking advantage of these capabilities and also its limitations, the BEM is used in the narrow region around the moving interface which will have its curvature and length changing with time and also where most of the temporal and spatial temperature variations occur close to the melting temperature. FDM on the other hand being fast and not having the above limitations except the accuracy, which depends on the numerical scheme, is used in the rest of the domain.

The boundary element method is a powerful and a general-purpose method which has been used by many researchers to solve complex physical problems (Banerjee and Butterfield [1981], Beskos [1987], Brebbia et al [1984], and Mukherjee [1982]). It has been employed to solve very tough problems where both conduction and convection dominates, like the 2-D transient conduction-convection equation with variable convective velocity, in a successful manner (Desilva et al [1998]). BEM has been applied to several steady state and transient heat conduction problems, including moving boundary and phase change problems (Curran et al [1986], Fleuries and Predeleanu [1987], O'Neill [1983] and Zabarar and Mukherjee [1987]). The discretization of the boundary can be tailored to any irregular shape, thus it is capable of handling complex geometry. The fact that this is an integral method, which involves the Green's function creates singular and near singular integrals when the field point approaches the source point. This creates not so well behaved integrals that need to be evaluated very

accurately. The end result of this fact is that the final discretized system of equations will be a fully populated matrix, and some of its coefficients would be computationally intensive to evaluate due to the above-mentioned singular nature.

To overcome these earlier mentioned limitations and also the strengths of both the methods, a coupled BEM-FDM numerical scheme is developed to model both the conduction in the solid substrate and the moving interface at the solid-liquid interface. The domain of the conduction region is decomposed in to two parts, which are solved using BEM and FDM separately. The BEM region is basically confined to the area close to the melting interface because of the computationally intensive nature of this method and also due to its restriction on the thermal diffusivity parameter. The rest of the domain, adjacent to the BEM region, thus away from the melting interface, FDM is applied due to its efficiency. This domain decomposition is well illustrated by Fig. 3.1. The two methods are combined at their common interface boundary by the common interface temperature and the continuity of the heat flux.

In the final part of this work, a thin layer model is developed for the liquid region in the melting zone, to simulate the complex process of laser drilling which involves the removal of material through vaporization and hydrodynamic melt ejection. In the work of Battech, Chen and Mazumder [1998] where 2-D axisymmetric laser drilling was modeled, the liquid layer near the axis was analyzed using stagnation flow analysis. But this work was valid only for regions very near the axis. In the later work of Battech, Chen and Mazumder [1999], it was extended to the whole beam radius using integral analysis techniques to model the laser drilling process. But both these studies were quasi-steady

and the conduction in the substrate was modeled assuming conduction over a semi-infinite region. The other limitations were in the laser interaction model that was employed in these studies. This could be characterized as a bulk energy conservation model that neglected discontinuities adjacent to the liquid-vapor interface.

In the present work, a thin layer model (TLM) is derived using the equations for free surface, mass conservation, momentum and energy in 3-D axisymmetric body intrinsic coordinate system. The reasons for this choice of coordinates are due to the axisymmetric nature of the problem and also due to the fact that the thickness of the liquid layer in the direction normal to the boundary being small, compared to the length of the boundary. As the boundary is moving fairly uniformly due to the melting interface, the thin layer could be solved in this coordinate system, which is fixed to the solid-liquid interface, with the assumption of it as an inertial frame. It also simplifies the formulations because the variables of interest are expressed explicitly in the equations. The equations are reduced by neglecting the second order curvature terms and assuming incompressibility. They are further simplified by evaluating the relative magnitudes of the terms and thereby neglecting the insignificant terms. This simplification is carried further by integrating in the thickness direction with the assumption of profiles for the temperature and the lateral velocity consistent with their known characteristics. The transient equations for the thickness, velocity and the temperature obtained from this derivation are hyperbolic in nature and thus need special care in solving. To formulate a solution method for these equations that is stable and non-oscillatory, a space-time method was employed. As this method is implemented for a fixed domain, while the TLM equations

are derived for a time dependent domain due to the moving solid-liquid interface, an immobilization transformation is utilized. This transformation is somewhat analogous to the 1-D laser drilling model of Chan [1999].

Space-time method is a robust method used to solve transient hyperbolic system of equations. Its basic attractiveness is in the simplicity of its mathematical formulation especially for the 1-D case and its built in staggered grid which is one of the techniques used to suppresses oscillations that are inherent when solving transient hyperbolic equations (Molls and Molls [1998]). Many complicated methods have been developed to overcome the above mentioned problems, and they use some form of staggered grid, flux-splitting, characteristics, artificial viscosity etc (Hirsch [1998]). Space-time method is elegant in that the method is a direct consequence of application of it to the flux conservation form of the system of equations. Chang [1995] successfully used this method where he developed the Solution Element and Conservation Element method to solve complicated problems like Navier-Stokes equations. It is also seen from his pioneering work in this area, that the numerical implementation of this method is direct and combining space and time it ensures the conservation of flux in both space and time. Another advantage is that it could be formulated as an explicit scheme with no numerical dissipation and also it could capture sharp gradients as illustrated by the simulation of problems like the shallow water equations in dam breaking model, travelling shock waves etc.

The TLM thus developed is coupled to the adjacent solid substrate that is modeled by the BEM, by the common interface velocity, mass conservation, common melting

temperature and the combined heat flux and moving boundary relationship obtained from the Stefan's boundary condition. This boundary condition basically governs the energy conservation at a moving interface. For the outer region adjacent to the BEM region but away from the melting interface, FDM is utilized for its fast computational ability. The two regions are coupled together at their common boundary by matching the temperature and the heat flux. As the liquid-vapor interface is moving, its normal velocity, the applied laser flux and the heat flux in the liquid region is related by the Stefan's boundary condition. As the Langmuir theory was shown to be acceptable (Chan [1997]), this is used to model the vapor removal at the liquid-vapor interface, and this theory also uses the relationship between surface temperature and vapor pressure from the Clausius-Clapeyron equation.

The coupled BEM-FDM formulation and the derivation of the TLM formulation are given in detail in Chapter 2.0. The details of the numerical formulation of the BEM and the FDM and the numerical solution of the 1-D hyperbolic system that arises from the formulation using the space-time flux conservation method for the TLM equations are given in Chapter 3.0. The coupling of the BEM-FDM and also the coupling of the TLM with the BEM-FDM model are also discussed. Also in this chapter, the solution of this unified model, combined with the above mentioned laser-material interaction relationships, is proposed as a way to simulate the laser drilling process for future work.

To validate the model, the results of the simulations done at varying stages of the model are presented. To check the conduction part of the model, which is done by the BEM-FDM, simulations with varying laser fluxes were done where the analytical

solutions are known. Similarly, to check the moving boundary part, a simulation that was somewhat simpler in nature, was done. In this test the whole domain was kept at the melting temperature and a constant heat flux perpendicular to the melting interface boundary was applied, thereby causing the movement of the interface at a constant normal velocity. To test the TLM segment, it was run with different laser power levels as given in the literature and the results were qualitatively compared. Direct quantitative comparisons with other 2-D models in the literature were not possible as the constitutive equations for laser-material interaction and also the many assumptions done in deriving the model were quite different from similar work done by others.

2.0 MATHEMATICAL FORMULATION

The schematic diagram given in Fig. 2.1 illustrates the basic laser drilling. Here the laser beam interacts with the liquid layer at the top surface, which is a moving boundary governed by the Stefan's boundary condition which governs the energy conservation at a moving interface. The vaporization creates a recoil pressure, which forces the liquid expulsion. The solid-liquid boundary is the melting or the solidifying interface depending on the temperature gradients in the solid and the liquid regions. This interface also moves according to the Stefan's boundary condition. The length scale for the laser beam radius is $\sim 1\text{mm}$ and that for the thickness of the liquid layer is $\sim 10\ \mu\text{m}$.

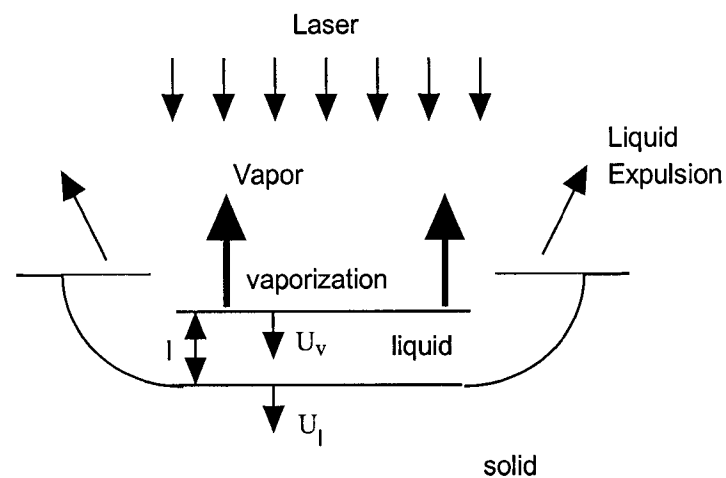


Figure 2.1 Schematic diagram for laser drilling

The solid region is simulated using the conduction model. The liquid layer is modeled using the free surface, continuity, momentum and the energy equations, which are simplified using the thin layer approximations. They are further simplified using integral methods by assuming appropriate profiles for the primary variables. Vaporization model given by the Langmuir theory is used to model the laser interaction with the liquid layer.

2.1 Conduction model

The solid region is modeled using the governing equation for the transient axisymmetric heat conduction equation in cylindrical coordinates.

$$\rho(T)c(T)\frac{\partial T}{\partial t} = \frac{1}{r}\frac{\partial}{\partial r}rk(T)\frac{\partial T}{\partial r} + \frac{\partial}{\partial z}k(T)\frac{\partial T}{\partial z} \quad (2.1)$$

Here $k(T)$ is the thermal conductivity, $\rho(T)$ is the density and $c(T)$ is the specific heat; all of them are characteristic for a particular material and depend on the temperature. The boundary conditions for the conduction model are posed, with reference to Figure 2.2.

$$\text{For } \Gamma_1, k(T)\frac{\partial T}{\partial n} = \tilde{q}(r) - h[T - T_\infty] \quad (2.2)$$

$\tilde{q}(r)$ - laser flux ; h - convective cooling coefficient ; T_∞ - ambient temperature

$$\text{For } \Gamma_2, k(T)\frac{\partial T}{\partial n} = -h[T - T_\infty] \quad (2.3)$$

$$\text{For } \Gamma_3, k(T) \frac{\partial T}{\partial r} = 0 \quad (2.4)$$

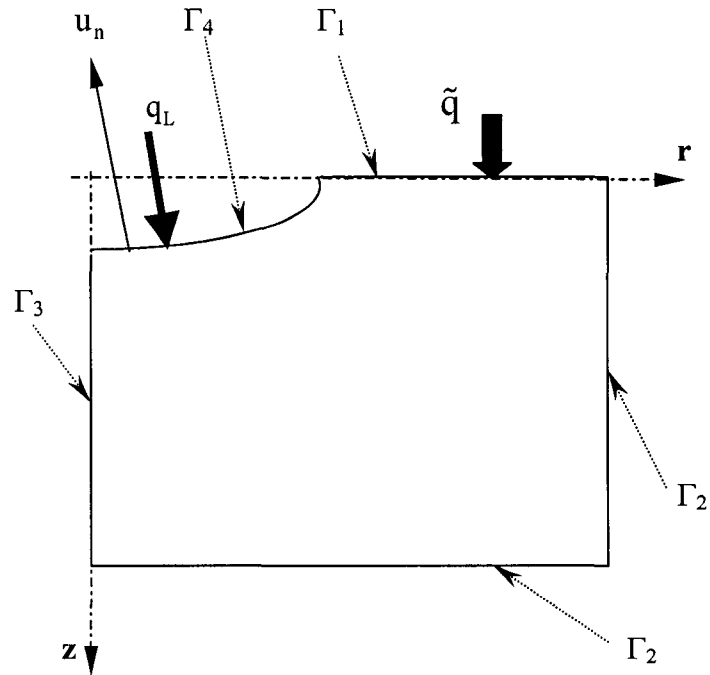


Figure 2.2 Schematic diagram for conduction model

When melting occurs, the moving solid-interface is governed by the Stefan's boundary condition. In the conduction model the heat flux from the liquid side is considered as the applied heat flux in this boundary condition. Here 'n' is the outer normal to the boundary and u_n is the interface velocity in the outer normal direction, q_L is the heat flux from the liquid layer, H_0 is the latent heat of fusion and ρ is the density of the solid material; and Stefan's boundary condition could be expressed as follows.

$$\text{For } \Gamma_4, q_L = k(T) \frac{\partial T}{\partial n} - H_0 \rho u_n \quad (2.5)$$

2.2 Thin layer model

The melt layer is modeled using the thin layer approximations. The justification for the thin layer model is given by the fact that the molten layer thickness in comparison to the radius of the laser beam is exceedingly small. The other reason is that the experimental data justifies this assumption. The flow in the liquid molten melt is basically driven by the external pressure imposed by the recoil from the ejecting gas due to the vaporization of the molten metal from the high temperature that is created by the absorption of the laser energy. Thus the thin layer hypothesis allows the pressure to be considered constant across the thickness of the layer thereby reducing the complications. Due to the above-mentioned nature of the problem the governing equations for the free surface, mass, momentum and the energy in the axisymmetric body intrinsic coordinate system are used. As for the momentum equation, only the lateral velocity equation is considered due to the thin layer approximation. The curvature changes are assumed to be moderate as the model is valid only for shallow depths compared to the length scales and the physical properties are considered to be constant for simplicity.

The assumption of the thin layer also simplifies the formulation of the governing equations as it allows the imposition of consistent profiles for velocity and temperature across the layer. In the case of velocity, the profile was such that it had no slip boundary condition at the solid-liquid interface and no tangential stress boundary condition at the liquid-vapor interface. With respect to the temperature, for simplicity a linear profile was imposed. The fact that the layer is very thin compared to the laser beam radius would somewhat justify this approximation. It is also supported in literature where a similar

profile was used in the modeling of quasi-steady state laser drilling (Batteh, Chen and Mazumder [1999]). Two other profiles that were more complex than this were tried. One was a second order polynomial and the other was an exponential type curve. These two profiles created complications, as were observed during the modeling work, by trying to accommodate the temperature gradient from the Stefan's boundary condition at the liquid-vapor surface. As this gradient is very high during the vaporization part and becomes negative when the laser is turned off, a profile that would accommodate these characteristics and also maintains a temperature gradient at the solid-liquid interface that makes physical sense, would be hard to find. Therefore with these simple profiles, the governing equations could be integrated across the layer to reduce them to one spatial dimension and to obtain a set of 1-D transient equations in the fashion of the boundary integral equations.

2.2.1 Governing equations for the thin layer

The following equations for the free surface, mass conservation, momentum and the energy are considered with reference to Fig. 2.3. Here the coordinate 'x' is along the body, which is the solid-liquid interface and 'y' is perpendicular to it. The radial distance 'r' is in the cylindrical coordinate sense and is measured from the axis of symmetry 'z' as illustrated in the figure. The velocities 'u' and 'v' are in the direction of 'x' and 'y' respectively. Also $V_{\ell v}$ is the normal velocity of the liquid-vapor interface and δ is the thickness of the liquid layer. All equations are given with respect to this body fitted coordinate system.

The kinematic free surface equation (Crapper [1984]) is given by,

$$\frac{\partial \delta}{\partial t} + u \frac{\partial \delta}{\partial x} - V_{\ell v} = 0 \quad (2.6)$$

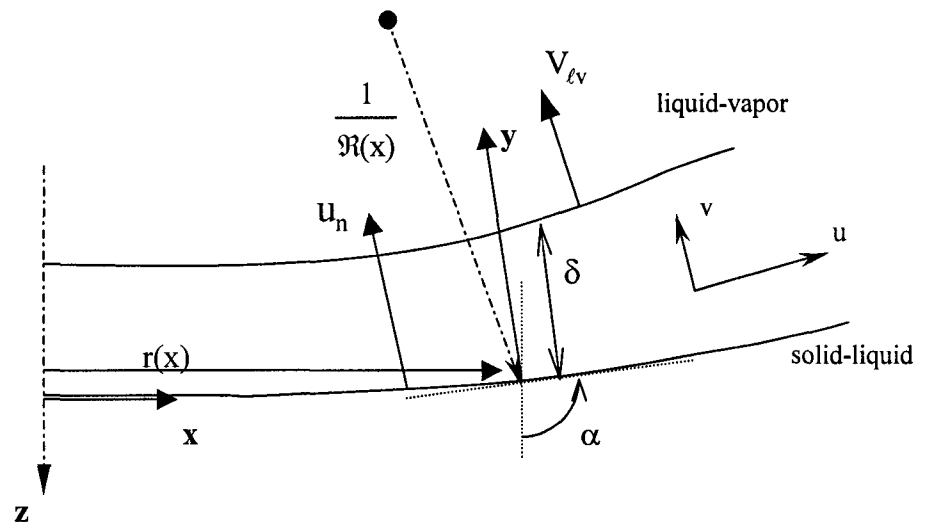


Figure 2.3 Thin layer geometric profile

The continuity, momentum and the energy equations in the axisymmetric body intrinsic coordinate system and for incompressible flow with constant properties are given by (Anderson et al [1984]),

$$\frac{\partial}{\partial x} \{ [r(x) + y \cos \alpha(x)] u \} + \frac{\partial}{\partial y} \{ [r(x) + y \cos \alpha(x)] [1 + y \mathfrak{R}(x)] v \} = 0 \quad (2.7)$$

$$\begin{aligned}
& \frac{\partial u}{\partial t} + \frac{u}{1+y\mathfrak{R}(x)} \frac{\partial u}{\partial x} + v \frac{\partial u}{\partial y} + \frac{uv\mathfrak{R}(x)}{1+y\mathfrak{R}(x)} - g_x + \frac{1}{\rho_\ell} \frac{\partial p}{\partial x} \\
& -v \left\{ \frac{1}{1+y\mathfrak{R}(x)} \frac{\partial}{\partial x} \left(\frac{1}{(1+y\mathfrak{R}(x))(r(x)+y\cos\alpha(x))} \times \right. \right. \\
& \quad \left. \left. \left[\frac{\partial}{\partial x} \{ [r(x)+y\cos\alpha(x)]u \} + \frac{\partial}{\partial y} \{ [r(x)+y\cos\alpha(x)][1+y\mathfrak{R}(x)]v \} \right] \right) \right. \\
& \quad \left. - \frac{1}{r(x)+y\cos\alpha(x)} \frac{\partial}{\partial y} \left[\frac{r(x)+y\cos\alpha(x)}{1+y\mathfrak{R}(x)} \left(\frac{\partial v}{\partial x} - \frac{\partial}{\partial y} [(1+y\mathfrak{R}(x))u] \right) \right] \right\} = 0
\end{aligned} \tag{2.8}$$

$$\begin{aligned}
& \frac{\partial T}{\partial t} + \frac{u}{1+y\mathfrak{R}(x)} \frac{\partial T}{\partial x} + v \frac{\partial T}{\partial y} - \frac{1}{\rho_\ell c_\ell} \Phi - \frac{\kappa_\ell}{(1+y\mathfrak{R}(x))(r(x)+y\cos\alpha(x))} \times \\
& \left\{ \frac{\partial}{\partial x} \left[\frac{r(x)+y\cos\alpha(x)}{1+y\mathfrak{R}(x)} \frac{\partial T}{\partial x} \right] + \frac{\partial}{\partial y} \left[(r(x)+y\cos\alpha(x))(1+y\mathfrak{R}(x)) \frac{\partial T}{\partial y} \right] \right\} = 0
\end{aligned}$$

$$\begin{aligned}
\text{where } \Phi = \mu & \left\{ 2 \left[\left(\frac{1}{1+y\mathfrak{R}(x)} \frac{\partial u}{\partial x} + \frac{v\mathfrak{R}(x)}{1+y\mathfrak{R}(x)} \right)^2 + \left(\frac{\partial v}{\partial y} \right)^2 + \right. \right. \\
& \left. \left(\frac{u(r' - y\alpha(x)'\sin\alpha(x))}{(1+y\mathfrak{R}(x))(r(x)+y\cos\alpha(x))} + \frac{v\cos\alpha(x)}{r(x)+y\cos\alpha(x)} \right)^2 \right] \\
& \left. + \left(\frac{1}{1+y\mathfrak{R}(x)} \frac{\partial v}{\partial x} + \frac{\partial u}{\partial y} - \frac{u\mathfrak{R}(x)}{1+y\mathfrak{R}(x)} \right)^2 \right\}
\end{aligned} \tag{2.9}$$

Here single prime refers to $\frac{\partial}{\partial x}$ and $\mathfrak{R}(x)$ is the curvature of the surface and α is the angle of the tangent to the surface makes with the direction of the symmetry axis as indicated in Fig. 2.3. Here g_x is the gravitational component in the 'x' direction. As for

the physical constants for the liquid layer, density is given by ρ_ℓ , thermal capacity by c_ℓ and thermal diffusivity by κ_ℓ , dynamic viscosity by μ and kinematic viscosity by ν .

To simplify the above governing equations the curvature and the thickness are considered small thus,

$$1 \gg y\mathcal{R}(x), 1 \gg \mathcal{R}(x), r(x) \gg y \cos \alpha(x), 1 \gg \cos \alpha(x) \text{ and } 1 \gg \alpha(x)'. \quad (2.9)$$

As for $r' \sim O(1)$ and $r'' \ll 1$ could be assumed. Therefore neglecting small order terms, the following equations are obtained.

$$\frac{\partial r(x)u}{\partial x} + \frac{\partial r(x)v}{\partial y} = 0 \quad (2.10)$$

$$\frac{\partial u}{\partial t} + u \frac{\partial u}{\partial x} + v \frac{\partial u}{\partial y} - g_x + \frac{1}{\rho_\ell} \frac{\partial p}{\partial x} - \nu \left[\frac{\partial^2 u}{\partial x^2} + \frac{r'}{r} \frac{\partial u}{\partial x} + \frac{\partial^2 u}{\partial y^2} - \left(\frac{r'}{r} \right)^2 u \right] = 0 \quad (2.11)$$

$$\frac{\partial T}{\partial t} + u \frac{\partial T}{\partial x} + v \frac{\partial T}{\partial y} - \kappa_\ell \left[\frac{\partial^2 T}{\partial y^2} + \frac{r'}{r} \frac{\partial T}{\partial x} + \frac{\partial^2 T}{\partial x^2} \right] \quad (2.12)$$

$$- \frac{\mu}{\rho_\ell c_\ell} \left[2 \left(\frac{\partial u}{\partial x} \right)^2 + \left(\frac{\partial v}{\partial y} \right)^2 + 2u^2 \left(\frac{r'}{r} \right)^2 + \left(\frac{\partial v}{\partial x} \right)^2 + 2 \left(\frac{\partial u}{\partial y} \frac{\partial v}{\partial x} \right) + \left(\frac{\partial u}{\partial y} \right)^2 \right] = 0$$

Looking at the relative importance of each term, the above equations could be further simplified. For this the equations are non-dimensionalised as given below, where the physical constants are at the melting temperature and where the reference temperature T_0 is considered as the melting temperature T_m . The non-dimensionalization is done using

the characteristic length, velocity and time scales. Here, drilling velocity V for the velocity perpendicular to the solid-liquid interface, laser pulse length τ for the time, beam radius R for the lateral dimension and layer thickness ε for the dimensions in the thickness direction, are the characteristic scales used.

$$r^* = r/R; \quad x^* = x/R; \quad y^* = (y - y_0)/\delta; \quad \delta^* = \delta/\varepsilon; \quad v^* = v/V; \quad u^* = u\varepsilon/VR; \quad (2.13)$$

$$T^* = T/T_0; \quad t^* = t/\tau; \quad p^* = p/(R^2\mu V/\varepsilon^3); \quad g_x^* = g_x/(g\varepsilon/R);$$

Substituting the above, the non-dimensional forms of the equations governing the free surface, continuity, momentum and the energy are given as follows.

$$\left(\frac{\varepsilon}{V\tau}\right) \frac{\partial \delta^*}{\partial t^*} + u^* \frac{\partial \delta^*}{\partial x^*} - V_{lv}^* = 0 \quad (2.14)$$

$$\frac{\partial r^*(x)u^*}{\partial x^*} + \frac{1}{\delta^*} \frac{\partial r^*(x)v^*}{\partial y^*} = 0 \quad (2.15)$$

$$\begin{aligned} & \left(\frac{\varepsilon}{V\tau}\right) \frac{\partial u^*}{\partial t^*} + u^* \frac{\partial u^*}{\partial x^*} + \frac{1}{\delta^*} v^* \frac{\partial u^*}{\partial y^*} - g_x^* \left[\left(\frac{g\varepsilon}{V^2}\right) \left(\frac{\varepsilon}{R}\right)^2 \right] \\ & + \left(\frac{\mu}{\rho_l \varepsilon V}\right) \left[\frac{\partial p^*}{\partial x^*} - \left(\frac{\varepsilon}{R}\right)^2 \frac{\partial^2 u^*}{\partial x^{*2}} - \left(\frac{\varepsilon}{R}\right)^2 \left(\frac{r''}{r^*}\right) \frac{\partial u^*}{\partial x^*} - \frac{1}{\delta^{*2}} \frac{\partial^2 u^*}{\partial y^{*2}} + \left(\frac{\varepsilon}{R}\right)^2 \left(\frac{r''}{r^*}\right)^2 u^* \right] = 0 \end{aligned} \quad (2.16)$$

$$\begin{aligned}
& \left(\frac{\varepsilon}{V\tau} \right) \frac{\partial T^*}{\partial t^*} + u^* \frac{\partial T^*}{\partial x^*} + \frac{1}{\delta^*} v^* \frac{\partial T^*}{\partial y^*} - \left(\frac{\kappa_\ell}{V\varepsilon} \right) \frac{1}{\delta^{*2}} \frac{\partial^2 T^*}{\partial y^{*2}} - \left(\frac{\kappa_\ell}{V\varepsilon} \right) \left(\frac{\varepsilon}{R} \right)^2 \left(\frac{\partial^2 T^*}{\partial x^{*2}} + \frac{r'^*}{r^*} \frac{\partial T^*}{\partial x^*} \right) \\
& - \left(\frac{\mu}{\varepsilon V \rho_\ell} \right) \left(\frac{V^2}{c_\ell T_0} \right) \left[2 \left(\frac{\partial u^*}{\partial x^*} \right)^2 + \frac{1}{\delta^{*2}} \left(\frac{\partial v^*}{\partial y^*} \right)^2 + 2u^{*2} \left(\frac{r'^*}{r^*} \right)^2 + \left(\frac{\varepsilon}{R} \right)^2 \left(\frac{\partial v^*}{\partial x^*} \right)^2 \right] \\
& \left[+ \frac{2}{\delta^{*2}} \left(\frac{\partial u^*}{\partial y^*} \frac{\partial v^*}{\partial x^*} \right) + \left(\frac{R}{\varepsilon} \right)^2 \frac{1}{\delta^{*2}} \left(\frac{\partial u^*}{\partial y^*} \right)^2 \right] = 0
\end{aligned} \tag{2.17}$$

To evaluate the significance of each term in the equations, non-dimensional groups were evaluated using the typical parameters in laser drilling. The range of values for the parameters τ , ε , R and V were obtained from the experimental data for laser drilling of mild steel and are given below.

$$\tau = 10 \mu\text{s} \sim 1 \text{ s}; \varepsilon = 0.0001 \sim 0.001 \text{ cm}; R = 0.1 \sim 10 \text{ cm}; V = 0.001 \sim 10 \text{ m/s} \tag{2.18}$$

$$T_0 = 1730 \text{ K}; c_\ell = 432 \text{ J/K/Kg}; \rho_\ell = 7879 \text{ kg/m}^3; \mu = 0.0055 \text{ N/m}^2/\text{s}$$

Using the above values for drilling of mild steel, it was observed that for the energy equation, the only terms that could be safely neglected are the terms for lateral conduction and all the terms except the vertical derivative of u velocity in the dissipation function. As for the momentum equation all the viscosity terms which have lateral derivatives of velocities could be neglected. Therefore with these simplifications the following equations are obtained.

$$\frac{\partial \delta}{\partial t} + u \frac{\partial \delta}{\partial x} - V_{lv} = 0 \quad (2.19)$$

$$\frac{\partial r(x)u}{\partial x} + \frac{\partial r(x)v}{\partial y} = 0 \quad (2.20)$$

$$\frac{\partial u}{\partial t} + u \frac{\partial u}{\partial x} + v \frac{\partial u}{\partial y} - g_x + \frac{1}{\rho_\ell} \frac{\partial p}{\partial x} - \nu \frac{\partial^2 u}{\partial y^2} = 0 \quad (2.21)$$

$$\frac{\partial T}{\partial t} + u \frac{\partial T}{\partial x} + v \frac{\partial T}{\partial y} - \kappa_\ell \frac{\partial^2 T}{\partial y^2} - \frac{\mu}{\rho_\ell c_\ell} \left(\frac{\partial u}{\partial y} \right)^2 = 0 \quad (2.22)$$

Eqns. (2.19)-(2.22) were further simplified by integrating across the thin layer. Eqns. (2.19) and (2.20) with the use of Leibnitz theorem will give the evolution equation for the thin layer thickness.

$$\frac{\partial \delta}{\partial t} + \frac{1}{r(x)} \frac{\partial}{\partial x} \int_0^\delta r(x)u \, dy + (v_1 - V_{lv}) - v_0 = 0 \quad (2.23)$$

Here v_1 is the absolute velocity at the liquid-vapor surface and v_0 is the velocity at the solid-liquid surface measured from the coordinate system fixed on that surface. Defining

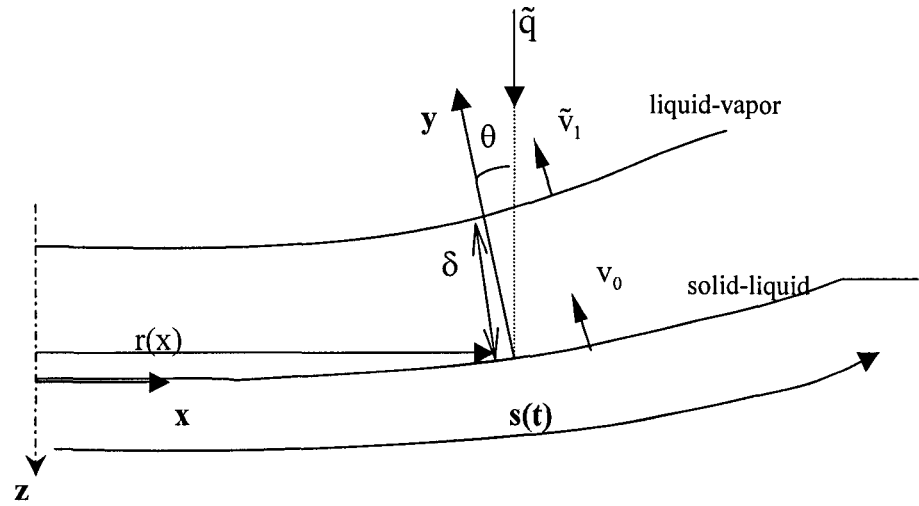


Figure 2.4 Thin layer schematic diagram

\tilde{v}_1 as the velocity relative to the liquid-vapor interface as shown in Fig. 2.4 this could be expressed as,

$$\frac{\partial \delta}{\partial t} + \frac{1}{r(x)} \frac{\partial}{\partial x} \int_0^{\delta} r(x) u \, dy + \tilde{v}_1 - v_0 = 0 \quad (2.24)$$

For the momentum Eqn. (2.21), using no slip boundary condition at the solid-liquid interface and no tangential stress boundary condition at the liquid-vapor interface, and where the subscript 0 and 1 refer to bottom and top interfaces respectively, the following equation could be derived.

$$\frac{\partial}{\partial t} \int_0^{\delta} u dy + \frac{1}{r(x)} \frac{\partial}{\partial x} \int_0^{\delta} r(x) u^2 dy + \tilde{v}_1 u_1 - g_x \delta + \frac{\delta}{\rho_\ell} \frac{\partial p}{\partial x} + v \left(\frac{\partial u}{\partial y} \Big|_0 \right) = 0 \quad (2.25)$$

Similarly, the energy Eqn. (2.22) could be integrated across the layer and it gives the following equation.

$$\frac{\partial}{\partial t} \int_0^{\delta} T dy + \frac{1}{r(x)} \frac{\partial}{\partial x} \int_0^{\delta} T u dy + \tilde{v}_1 T_1 - v_0 T_0 - \kappa_\ell \frac{\partial T}{\partial y} \Big|_0 - \frac{\mu}{\rho_\ell c_\ell} \int_0^{\delta} \left[\left(\frac{\partial u}{\partial y} \right)^2 \right] dy = 0 \quad (2.26)$$

To integrate the thickness, momentum and the energy equations, the following profiles for the temperature and the velocity are assumed that are consistent with the physics of the problem. As for the velocity, no-slip condition at the bottom and no tangential stress at the top are imposed. As for the temperature, a linear profile is imposed, thus at the bottom solid-liquid interface the temperature gradient on the liquid side would be known from this profile. This would give the heat flux from the liquid side for the Stefan's boundary condition given in Eqn. (2.35) and also the heat flux at the solid-liquid interface for the energy equation given by Eqn. (2.26). As for the top interface heat flux on the liquid layer needed in Eqn. (2.26), it would be computed from the Stefan's boundary condition given in Eqn. (2.34). This equation would utilize the applied laser flux and \tilde{v}_1 , the velocity relative and normal to the liquid-vapor interface of the ejecting molten metal due to vaporization. The profiles and the integrals across the layer thickness are given below.

$$T = 2(\bar{T} - T_0)\frac{y}{\delta} + T_0 \quad ; \quad \text{where,} \quad \bar{T} = \frac{T_1 + T_0}{2} \quad (2.27)$$

$$u = \frac{u_1}{\delta^2}(2\delta y - y^2) \quad (2.28)$$

$$\int_0^\delta dy = \delta \quad ; \quad \int_0^\delta u dy = \frac{2}{3}u_1\delta \quad ; \quad \int_0^\delta u^2 dy = \frac{8}{15}u_1^2\delta \quad ; \quad \int_0^\delta \left(\frac{\partial u}{\partial y}\right)^2 dy = \frac{4}{3\delta}u_1^2 \quad (2.29)$$

$$\int_0^\delta T dy = \bar{T}\delta \quad ; \quad \int_0^\delta Tu dy = \frac{5}{6}u_1\bar{T}\delta - \frac{1}{6}u_1T_0\delta$$

Apart from the above integrals, an immobilization transformation was done in the lateral coordinate 'x' due to the time dependent nature of the length of the interface. The need for this is seen from Fig. 2.4. As the drilling proceeds the length of the curved interface increases with time, which is given by $s(t)$. One way to handle this is to fix the spatial dimension of the computational domain using this transformation. This would simplify the domain problem but it would change the governing equations. The immobilization transformation is given below.

$$\varphi = \frac{x}{s(t)} \quad ; \quad \frac{\partial}{\partial t} = \frac{\partial}{\partial t} - \frac{\varphi \dot{s}}{s} \frac{\partial}{\partial \varphi} \quad ; \quad \frac{\partial}{\partial x} = \frac{1}{s} \frac{\partial}{\partial \varphi} \quad , \quad \text{where} \quad \dot{s} = \frac{ds(t)}{dt} \quad (2.30)$$

Using the above transformations, the evolution equations could be reformulated as follows,

$$\frac{\partial \delta}{\partial t} + \frac{1}{r} \frac{\partial}{\partial \varphi} r \left(\frac{2 u_1 \delta}{3 s} - \frac{\varphi \dot{s} \delta}{s} \right) + \frac{1}{r} \frac{\partial r}{\partial \varphi} \frac{\varphi \dot{s} \delta}{s} + \frac{\dot{s} \delta}{s} + \tilde{v}_1 - v_0 = 0 \quad (2.31)$$

$$\begin{aligned} \frac{\partial (u_1 \delta)}{\partial t} + \frac{1}{r} \frac{\partial}{\partial \varphi} r \left(\frac{4 u_1^2 \delta}{5 s} - \frac{\varphi \dot{s} u_1 \delta}{s} + \frac{3 p \delta}{2 \rho_\ell s} \right) + \frac{\varphi \dot{s} u_1 \delta}{r s} \frac{\partial r}{\partial \varphi} + \frac{\dot{s} u_1 \delta}{s} - \frac{3 p}{2 \rho_\ell s} \frac{\partial \delta}{\partial \varphi} \\ - \frac{3 p \delta}{2 r \rho_\ell s} \frac{\partial r}{\partial \varphi} + \frac{3}{2} (\tilde{v}_1 u_1 - g_x \delta) + v \left(\frac{3 u_1}{\delta} \right) = 0 \end{aligned} \quad (2.32)$$

$$\begin{aligned} \frac{\partial (\bar{T} \delta)}{\partial t} + \frac{1}{r} \frac{\partial}{\partial \varphi} r \left(\frac{5 u_1 \bar{T} \delta}{6 s} - \frac{1 u_1 \delta T_0}{6 s} - \frac{\varphi \dot{s} \bar{T} \delta}{s} \right) + \frac{\varphi \dot{s} \bar{T} \delta}{r s} \frac{\partial r}{\partial \varphi} + \frac{\dot{s} \bar{T} \delta}{s} + 2 \bar{T} \tilde{v}_1 \\ - T_0 (\tilde{v}_1 + v_0) - \frac{k_\ell}{\rho_\ell c_\ell} \left[\frac{\partial T}{\partial y} \right]_{\ell-v} + 2 \kappa \frac{\bar{T} - T_0}{\delta} + \frac{\mu}{\rho_\ell c_\ell} \left(\frac{4 u_1^2}{3 \delta} \right) = 0 \end{aligned} \quad (2.33)$$

In this formulation T_0 is the solid-liquid interface melting temperature and $\left[\kappa_\ell \frac{\partial T}{\partial y} \right]_{\ell-v}$ is determined from the imposed net heat flux, \tilde{v}_1 and the Stefan's boundary condition at the liquid-vapor interface as stated earlier. For the Stefan's boundary condition at the top and bottom interfaces the material properties are taken for liquid metal at the melting temperature except where the physical properties without subscript denotes the solid properties at the melting temperature. Here θ denotes the angle that the laser flux \tilde{q} makes with the normal to the interface as shown in Fig. 2.4 and also H_1 and H_0 are the latent heats of vaporization and fusion respectively and 'n' denotes the outer normal at the solid-liquid interface.

The Stefan's boundary condition at the top liquid-vapor interface gives the following.

$$[\tilde{q} \cos \theta] = \left(k_\ell \frac{\partial T}{\partial y} \right)_{\ell-v} + H_1 \rho_\ell \tilde{v}_1 \quad (2.34)$$

Similarly the Stefan's boundary condition at the bottom solid-liquid interface gives the following equation.

$$\left(k_\ell \frac{\partial T_\ell}{\partial y} \right)_{s-\ell} = \left[k \left(\frac{\partial T}{\partial n} \Big|_{s-\ell} \right) \right] + H_0 \rho_\ell v_0 \quad (2.35)$$

The mass balance at the solid-liquid interface basically gives the relationship between the drilling velocity from the movement of the solid-liquid boundary given by u_n as shown in Fig. 2.4, and v_0 , the velocity of the molten material relative to the interface. This is similar to the mass balance of Batteh, Chen and Mazumder [1999].

$$\rho_\ell v_0 = -\rho u_n \quad (2.36)$$

The top surface pressure, velocity and temperature are related by two constitutive equations. The Langmuir theory was observed to model the material removal in an acceptable manner (Chan [1997]). This model is based on the kinetic theory which is used to calculate the number of particles leaving a unit cube of vapor bounded on one

side by the metal. In this theory vaporization rates are found using the Maxwell distribution, ideal gas law and the Clausius-Claperon equation which describes the dependence of vapor pressure on temperature (Allmen [1987]). Therefore the top surface pressure p as a function of the top surface temperature T_1 and the relationship among the velocity v_1 , T_1 and the p are obtained.

$$p = p_a \exp \left[-\frac{H_1}{G} \left(\frac{1}{T_1} - \frac{1}{T_b} \right) \right] \quad (2.37)$$

$$v_1 = \frac{1}{\rho_l \sqrt{2\pi G}} \frac{1}{\sqrt{T_1}} p \quad (2.38)$$

Here p_a is the atmospheric pressure, T_b is the boiling temperature and G is the gas constant. The last two parameters are given for mild steel. Finally the transient governing equations with the conjunction of the Stefan's boundary conditions and the two constitutive equations given above, completes the mathematical model.

3.0 NUMERICAL FORMULATION

The numerical simulation is done in two parts. In the first part the solid region where the conduction model is employed, is divided into two computational domains as shown in Fig. 3.1. The first region close to the moving solid-liquid interface, a BEM formulation was applied to simulate the transient heat conduction with the moving boundary. In the rest of the domain, which is congruent to the BEM region and furthestmost from the moving boundary, the simulation was done using a FDM scheme. The coupled BEM-FDM equations were solved using an implicit Crank-Nicholson method, and their detailed derivations are given in a later section.

In the second part, the thin liquid layer equations of the TLM which models the behavior of the molten liquid that is adjacent to the moving solid-liquid interface of the BEM domain is solved using a Space-Time method. The normal velocity, flux and the temperature at the solid-liquid interface in the BEM formulation are coupled with the TLM formulation using the Stefan's boundary condition, common interface melting temperature and the conservation of mass at the solid-liquid interface. The BEM is an integral method whose integrals depend on the field and source points. If any of these points falls on the moving part of the boundary, the respective integral coefficients that depend on these points in turn will be indirectly dependent on the normal velocity and the profile of the solid-liquid interface. The TLM equations also depend on the moving boundary. Consequently, iterations are needed to obtain the solution for the next time step for the combined BEM-FDM-TLM model.

3.1 Conduction formulation

The conduction solution is implemented by subdividing the solid region into two segments as shown in Fig. 3.1. Figure 3.2 gives the relevant notational information. The boundary conditions along the boundaries Γ_1 to Γ_4 are given by Eqns. (2.2) – (2.5). The common interface boundary for the BEM and the FDM region is given by Γ_C . The ℓ_2 to ℓ_6 are the boundary nodal indices of the BEM formulation while NR1, NR, NZ1 and NZ are that for the FDM formulation. The two methods are coupled along this common boundary by the common temperature and the temperature gradient conditions. The mechanism of implementing this is by using the temperature from the FDM along this boundary to compute the temperature gradient from the BEM. This is used to impose a heat flux condition on the FDM elements along the common interface boundary.

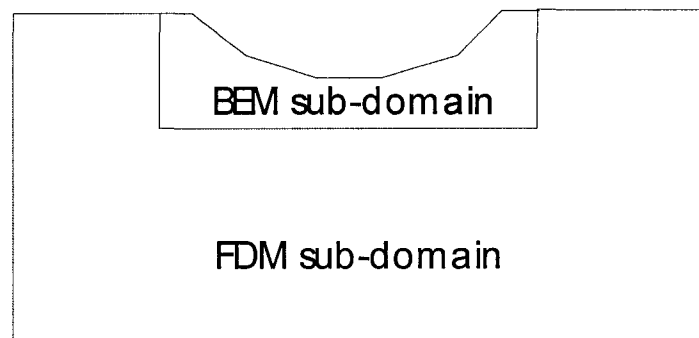


Figure 3.1 BEM and FDM domain decomposition

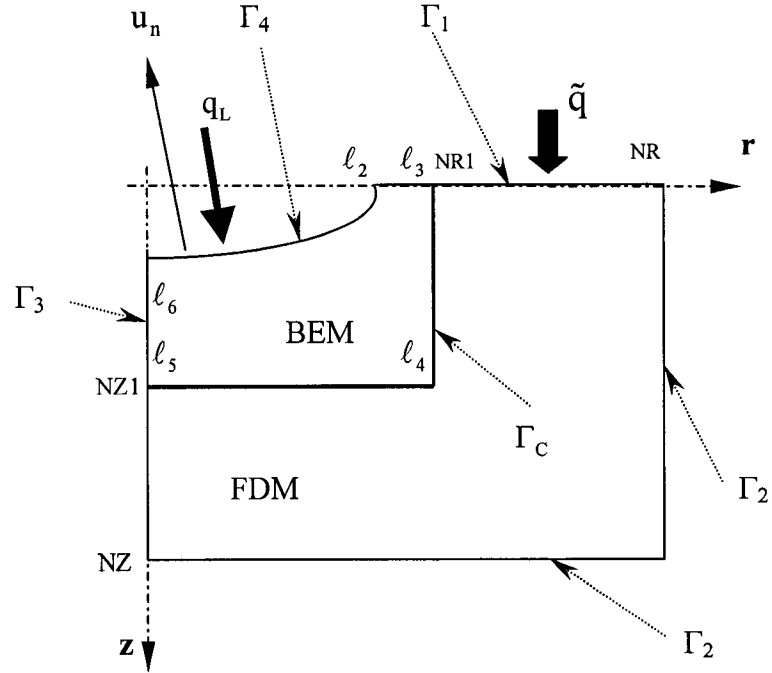


Figure 3.2 Schematic diagram for the conduction region

3.1.1 BEM formulation

Consider Eqn. (2.1), where the thermal diffusivity, $\kappa = k/\rho c$ is considered a constant for the BEM formulation. This consideration is required for this method thus making it valid for a small region near the interface where the temperature variations are minimal. Taking weighted residual formulation of the transient heat conduction equation,

$$\int_{t=0}^{\tau} \int_{\Omega(t)} G \left[\frac{\partial \Gamma}{\partial t} - \kappa \left(\frac{1}{r} \frac{\partial}{\partial r} r \frac{\partial \Gamma}{\partial r} + \frac{\partial}{\partial z} \frac{\partial \Gamma}{\partial z} \right) \right] d\Omega dt = 0 \quad (3.1)$$

Integrating by parts and using the auxiliary problem associated with the transient heat conduction equation,

$$-\frac{\partial G}{\partial t} = \kappa \left(\frac{1}{r} \frac{\partial}{\partial r} r \frac{\partial G}{\partial r} + \frac{\partial}{\partial z} \frac{\partial G}{\partial z} \right) - \delta(r-r_i) \delta(z-z_i) \delta(t-\tau) \quad (3.2)$$

The equation for the boundary integral formulation is given as follows.

$$T(r_i, z_i, \tau) = - \int_{t=0}^{\tau} \left\{ \int_{\Gamma(t)} \kappa G \frac{\partial T}{\partial n} d\Gamma + \int_{\Gamma(t)} \left(-\kappa \frac{\partial G}{\partial n} + u_n G \right) T d\Gamma \right\} dt - \int_{\Omega(0)} T G d\Omega \quad (3.3)$$

Considering the fact that the normal velocity is relevant only in the moving part of the boundary, the above equation could be reformulated as follows, where Γ_s and Γ_m are stationary and moving boundaries respectively and T_m is the melting temperature.

$$T(r_i, z_i, \tau) = - \int_{t=0}^{\tau} \left\{ \int_{\Gamma_s(t)} \kappa G \frac{\partial T}{\partial n} d\Gamma + \int_{\Gamma_s(t)} \kappa \left(-\frac{\partial G}{\partial n} \right) T d\Gamma \right\} dt - \int_{t=0}^{\tau} \left\{ \int_{\Gamma_m(t)} \left(\kappa \frac{\partial T}{\partial n} + u_n T_m \right) G d\Gamma + \int_{\Gamma_m(t)} \kappa \left(-\frac{\partial G}{\partial n} \right) T_m d\Gamma \right\} dt - \int_{\Omega(0)} T G d\Omega \quad (3.4)$$

Substituting the boundary conditions, with the Γ_c denoting the common interface boundary between the FDM and BEM regions with reference to Fig. 3.2,

$$\begin{aligned}
T(r_i, z_i, \tau) = & - \int_{t=0}^{\tau} \left\{ \int_{\Gamma_1(t)} \kappa \left[-\frac{h}{k} G + \left(-\frac{\partial G}{\partial n} \right) \right] T d\Gamma + \int_{\Gamma_1(t)} \frac{\kappa}{k} [hT_\infty + \tilde{q}] G d\Gamma \right\} dt \\
& - \int_{t=0}^{\tau} \left\{ \int_{\Gamma_c} \kappa G \frac{\partial T}{\partial n} d\Gamma + \int_{\Gamma_c} \kappa \left(-\frac{\partial G}{\partial n} \right) T d\Gamma \right\} dt - \int_{t=0}^{\tau} \int_{\Gamma_4(t)} \kappa \left(-\frac{\partial G}{\partial n} \right) T d\Gamma dt \\
& - \int_{t=0}^{\tau} \left\{ \int_{\Gamma_5(t)} \left(\frac{\kappa H_0 \rho}{k} + T_m \right) G u_n d\Gamma + \int_{\Gamma_5(t)} \kappa \left(-\frac{\partial G}{\partial n} \right) T_m d\Gamma + \int_{\Gamma_5(t)} \frac{\kappa}{k} G q_L d\Gamma \right\} dt \\
& - \int_{\Omega(0)} T G d\Omega
\end{aligned} \tag{3.5}$$

This boundary integral equation can be used to calculate the temperature within the domain as long as both the temperature and the normal gradient of temperature on the boundary are known. In a well-posed problem either the temperature, or the normal temperature gradient, or a combination of the two is prescribed on the boundary. For the moving part of the boundary, the temperature on it is assumed as the constant melting temperature (T_m) and the normal temperature gradient is related to the normal velocity by the Stefan's boundary condition. To compute the unknown quantities (temperature or normal temperature gradient or normal velocity of the moving boundary) along the boundary, the source point (r_i, z_i, τ) is placed on the boundary and thereby obtaining a boundary integral equation. The stationary boundary is discretized into linear spatial elements and they are constant with time except for the two edge elements that are next to

the moving boundary. The moving boundary is discretized using cubic spline elements. The advantage of using these elements is that at the common node between the elements there is no discontinuity of the heat flux normal to the boundary or the normal velocity. The method of computing these boundary integrals and the domain integrals are given in Appendix A. Due to the singular behavior of some of these integrals, special techniques had to be adopted. As the integrands decay very fast with distance and time, and because they take a long time to evaluate, it is very important to stop computing the integrals when they become insignificant in magnitude. This could be achieved by first computing the upper bound of their absolute values very efficiently as given in Appendix A. The importance of this is further enumerated when the total number of boundary and domain integrals are considered. For a $n \times n$ grid the number of boundary integrals coefficients are $\sim 8n^3$ and the number of domain integrals coefficients are $\sim 4n^4$. Therefore it is obvious that when the grid discretization becomes finer and thus the number of grids become larger the computational time would increase very rapidly.

With respect to Fig. 3.2, let the number of nodes for the stationary boundary corresponding to points between ℓ_2 and ℓ_6 , and the moving boundary be given as N and M respectively and let the superscript 1 and 2 refer to the initial and final time respectively. The final matrix equation for the integral Eqn. (3.5), with the Stefan's boundary condition imposed on the moving boundary, can be represented as follows,

$$\begin{aligned}
& \sum_{j=1}^N A_{ji}^2 T_j^2 + \sum_{j=1}^N B_{ji}^2 \left(\frac{\partial T}{\partial n} \right)_j^2 + \sum_{j=1}^M E_{ji}^2 u_{nj}^2 + \sum_{j=1}^M F_{ji}^2 T_m + \sum_{j=1}^M C_{ji}^2 q_L^2 \\
& = - \sum_{j=1}^N A_{ji}^1 T_j^1 - \sum_{j=1}^N B_{ji}^1 \left(\frac{\partial T}{\partial n} \right)_j^1 - \sum_{j=1}^M E_{ji}^1 u_{nj}^1 - \sum_{j=1}^M F_{ji}^1 T_m - \sum_{j=1}^M C_{ji}^1 q_L^1 - D_i^1
\end{aligned} \tag{3.6}$$

Incorporating the relevant boundary conditions given by Eqns. (2.2)-(2.4) on parts of the boundary indicated in Eqn. (3.5), the above system of equations could be represented by block matrix form. Where $[\tilde{A}^2]$ and $[\tilde{B}^2]$ are the coefficient matrices from the final time, while $\{\tilde{R}^{12}\}$ is the row vector from the contributions from the domain and boundary integrals at the initial time, and also any contributions from the known boundary values from the boundary conditions in the final time boundary integrals. Any of the coefficients in the square matrices and row vector, that are related to the moving boundary, whether due to the source point or the field points lying on this boundary, will depend on the boundary velocity and thereby on time as will be seen later.

Thus Eqn. (3.6) could be represented as follows,

$$\{\tilde{P}^2\}[\tilde{A}^2] = \{\tilde{Q}^2\}[\tilde{B}^2] + \{\tilde{R}^{12}\} \tag{3.7}$$

Post multiplying by the inverse,

$$\{\tilde{P}^2\} = \{\tilde{Q}^2\}[\tilde{B}^2][\tilde{A}^2]^{-1} + \{\tilde{R}^{12}\}[\tilde{A}^2]^{-1} \tag{3.8}$$

Therefore this could be represented as,

$$\{\tilde{P}^2\} = \{\tilde{Q}^2\}[\tilde{C}] + \{\tilde{D}\} \tag{3.9}$$

Where,

$$\{\tilde{\mathbf{P}}^2\} = \{T_{\ell_2} \dots T_{\ell_3-1} \mathbf{q}_{\ell_3}^{\text{bem}} \dots \mathbf{q}_{\ell_5}^{\text{bem}} T_{\ell_5+1} \dots T_{\ell_6} \mathbf{u}_{n1} \dots \mathbf{u}_{nM}\}$$

$$\{\tilde{\mathbf{Q}}^2\} = \{0 \dots 0 T_{\ell_3} \dots T_{\ell_5} 0 \dots \dots 0\}$$

Along Γ_C : $\mathbf{q}_\ell^{\text{bem}} = \partial T / \partial n$, and could be expressed from the matrix Eqn. (3.9) as,

$$\mathbf{q}_\ell^{\text{bem}} = \sum_{j=\ell_3}^{\ell_5} \tilde{\mathbf{c}}_{j\ell} T_j + \tilde{\mathbf{d}}_\ell \quad (3.10)$$

And further, where $\tilde{\mathbf{c}}$ are the elements of matrix $\tilde{\mathbf{C}}$, define,

$$\mathbf{q}_\ell^{\text{bem_dia}} = \tilde{\mathbf{c}}_{\ell\ell} T_\ell$$

$$\mathbf{q}_\ell^{\text{bem_offdia}} = \sum_{\substack{j=\ell_3 \\ j \neq \ell}}^{\ell_5} \tilde{\mathbf{c}}_{j\ell} T_j + \tilde{\mathbf{d}}_\ell \quad (3.11)$$

Therefore $\mathbf{q}_\ell^{\text{bem}}$ could be decomposed as,

$$\mathbf{q}_\ell^{\text{bem}} = \mathbf{q}_\ell^{\text{bem_dia}} + \mathbf{q}_\ell^{\text{bem_offdia}} \quad (3.12)$$

Thus at the interface of the FDM and the BEM boundary, $\mathbf{q}_\ell^{\text{bem}}$ could be imposed as a flux boundary condition on the FDM formulation as seen in the next subsection.

3.1.2 FDM formulation

Substituting the finite difference form of the Laplacian using central difference, the transient heat conduction equation could be given as,

$$\begin{aligned} \rho(T_{i,j})c(T_{i,j}) \frac{\partial T_{i,j}}{\partial t} &= \frac{1}{z_{j+1/2} - z_{j-1/2}} \left(k_{i,j+1/2} \frac{T_{i,j+1} - T_{i,j}}{z_{j+1} - z_j} - k_{i,j-1/2} \frac{T_{i,j} - T_{i,j-1}}{z_j - z_{j-1}} \right) \\ &+ \frac{1}{r_i} \frac{1}{r_{i+1/2} - r_{i-1/2}} \left(r_{i+1/2} k_{i+1/2,j} \frac{T_{i+1,j} - T_{i,j}}{r_{i+1} - r_i} - r_{i-1/2} k_{i-1/2,j} \frac{T_{i,j} - T_{i-1,j}}{r_i - r_{i-1}} \right) \end{aligned} \quad (3.13)$$

The above equation can be written in the energy balance form as,

$$\begin{aligned} \rho(T_{i,j})c(T_{i,j}) \frac{\partial T_{i,j}}{\partial t} &\left[\pi(r_{i+1/2}^2 - r_{i-1/2}^2)(z_{j+1/2} - z_{j-1/2}) \right] = \\ &\pi(r_{i+1/2}^2 - r_{i-1/2}^2) \left(k_{i,j+1/2} \frac{T_{i,j+1} - T_{i,j}}{z_{j+1} - z_j} - k_{i,j-1/2} \frac{T_{i,j} - T_{i,j-1}}{z_j - z_{j-1}} \right) \\ &+ 2\pi(z_{j+1/2} - z_{j-1/2}) \left(r_{i+1/2} k_{i+1/2,j} \frac{T_{i+1,j} - T_{i,j}}{r_{i+1} - r_i} - r_{i-1/2} k_{i-1/2,j} \frac{T_{i,j} - T_{i-1,j}}{r_i - r_{i-1}} \right) \end{aligned} \quad (3.14)$$

Dividing by the volume gives the formulation for any internal point (i, j),

$$\begin{aligned} \rho(T_{i,j})c(T_{i,j}) \frac{\partial T_{i,j}}{\partial t} &= \frac{1}{z_{j+1/2} - z_{j-1/2}} \left(k_{i,j+1/2} \frac{T_{i,j+1} - T_{i,j}}{z_{j+1} - z_j} - k_{i,j-1/2} \frac{T_{i,j} - T_{i,j-1}}{z_j - z_{j-1}} \right) \\ &+ \frac{2}{r_{i+1/2}^2 - r_{i-1/2}^2} \left(r_{i+1/2} k_{i+1/2,j} \frac{T_{i+1,j} - T_{i,j}}{r_{i+1} - r_i} - r_{i-1/2} k_{i-1/2,j} \frac{T_{i,j} - T_{i-1,j}}{r_i - r_{i-1}} \right) \end{aligned} \quad (3.15)$$

For the points on the boundary, the boundary conditions are incorporated in the above discretized equation and this modifies the FDM formulation.

At the outer radius $r = r_{NR}$, convective cooling condition,

$$q = k(T) \frac{\partial T}{\partial r} = -h(T - T_\infty) \text{ is applied thus,}$$

$$\begin{aligned} \rho(T_{NR,j})c(T_{NR,j})\frac{\partial T_{NR,j}}{\partial t} = & \frac{1}{z_{j+1/2} - z_{j-1/2}} \left(k_{NR,j+1/2} \frac{T_{NR,j+1} - T_{NR,j}}{z_{j+1} - z_j} - k_{NR,j-1/2} \frac{T_{NR,j} - T_{NR,j-1}}{z_j - z_{j-1}} \right) \\ & + \frac{2}{r_{NR}^2 - r_{NR-1/2}^2} \left(-r_{NR} h(T_{NR,j} - T_{\infty}) - r_{NR-1/2} k_{NR-1/2,j} \frac{T_{NR,j} - T_{NR-1,j}}{r_{NR} - r_{NR-1}} \right) \end{aligned} \quad (3.16)$$

At the bottom surface $z = 0$ ($j = 1$), convective cooling and heat flux from the laser beam are applied,

$$q = -k(T) \frac{\partial T}{\partial z} = -h(T - T_{\infty}) + \tilde{q}$$

$$\begin{aligned} \rho(T_{i,1})c(T_{i,1})\frac{\partial T_{i,1}}{\partial t} = & \frac{1}{z_{j+1/2}} \left(k_{i,1+1/2} \frac{T_{i,2} - T_{i,1}}{z_2 - z_1} - h(T_{i,1} - T_{\infty}) + \tilde{q} \right) \\ & + \frac{2}{r_{i+1/2}^2 - r_{i-1/2}^2} \left(r_{i+1/2} k_{i+1/2,j} \frac{T_{i+1,1} - T_{i,1}}{r_{i+1} - r_i} - r_{i-1/2} k_{i-1/2,1} \frac{T_{i,1} - T_{i-1,1}}{r_i - r_{i-1}} \right) \end{aligned} \quad (3.17)$$

At the top surface $Z = \text{thickness}$ ($j = NZ$), convective cooling is applied,

$$q = -k(T) \frac{\partial T}{\partial z} = -h(T - T_{\infty})$$

$$\begin{aligned} \rho(T_{i,NZ})c(T_{i,NZ})\frac{\partial T_{i,NZ}}{\partial t} = & \frac{1}{z_{NZ} - z_{NZ-1/2}} \left(-k_{i,NZ-1/2} \frac{T_{i,NZ} - T_{i,NZ-1}}{z_{NZ} - z_{NZ-1}} - h(T_{i,NZ} - T_{\infty}) \right) \\ & + \frac{2}{r_{i+1/2}^2 - r_{i-1/2}^2} \left(r_{i+1/2} k_{i+1/2,NZ} \frac{T_{i+1,NZ} - T_{i,NZ}}{r_{i+1} - r_i} - r_{i-1/2} k_{i-1/2,NZ} \frac{T_{i,NZ} - T_{i-1,NZ}}{r_i - r_{i-1}} \right) \end{aligned} \quad (3.18)$$

For the outer edge two corner points, at $r = r_{NR}$ and $z = 0$ ($i = NR, j = 1$),

$$\begin{aligned} \rho(T_{NR,1})c(T_{NR,1}) \frac{\partial T_{NR,j}}{\partial t} &= \frac{1}{z_{1+1/2}} \left(k_{NR,1+1/2} \frac{T_{NR,1+1} - T_{NR,1}}{z_2 - z_1} - r_{NR} h(T_{NR,1} - T_\infty) + \tilde{q} \right) \\ &+ \frac{2}{r_{NR}^2 - r_{NR-1/2}^2} \left(-r_{NR-1/2} k_{NR-1/2,1} \frac{T_{NR,j} - T_{NR-1,j}}{r_{NR} - r_{NR-1}} - r_{NR} h(T_{NR,1} - T_\infty) \right) \end{aligned} \quad (3.19)$$

At $r = r_{NR}$, and $z = \text{thickness}$ ($i = NR, j = NZ$),

$$\begin{aligned} \rho(T_{NR,NZ})c(T_{NR,NZ}) \frac{\partial T_{NR,NZ}}{\partial t} &= \frac{1}{z_{NZ-1/2}} \left(-k_{NR,NZ-1/2} \frac{T_{NR,j} - T_{NR,j-1}}{z_j - z_{j-1}} - h(T_{NR,NZ} - T_\infty) \right) \\ &\frac{2}{r_{NR}^2 - r_{NR-1/2}^2} \left(-r_{NR-1/2} k_{NR-1/2,NZ} \frac{T_{NR,NZ} - T_{NR-1,NZ}}{r_{NR} - r_{NR-1}} - r_{NR} h(T_{NR,NZ} - T_\infty) \right) \end{aligned} \quad (3.20)$$

At $i = 1; j = NZ1 + 1, \dots, NZ - 1$,

$$\begin{aligned} \rho(T_{1,j})c(T_{1,j}) \frac{\partial T_{1,j}}{\partial t} &= \frac{1}{z_{j+1/2} - z_{j-1/2}} \left(k_{1,j+1/2} \frac{T_{1,j+1} - T_{1,j}}{z_{j+1} - z_j} - k_{1,j-1/2} \frac{T_{1,j} - T_{1,j-1}}{z_j - z_{j-1}} \right) \\ &+ \frac{2}{r_{1+1/2}^2} \left(r_{1+1/2} k_{1/2,j} \frac{T_{2,j} - T_{1,j}}{r_2 - r_1} \right) \end{aligned} \quad (3.21)$$

At $i = 1; j = NZ$,

$$\begin{aligned} \rho(T_{1,NZ})c(T_{1,NZ}) \frac{\partial T_{1,NZ}}{\partial t} &= \frac{1}{z_{NZ} - z_{NZ-1/2}} \left(-k_{1,NZ-1/2} \frac{T_{1,NZ} - T_{1,NZ-1}}{z_{NZ} - z_{NZ-1}} - h(T_{1,NZ} - T_\infty) \right) \\ &+ \frac{2}{r_{1+1/2}^2} \left(r_{1+1/2} k_{1/2,NZ} \frac{T_{2,NZ} - T_{1,NZ}}{r_2 - r_1} \right) \end{aligned} \quad (3.22)$$

For the interface of the BEM and the FDM boundary the formulation incorporates the temperature gradient from the BEM formulation given in the earlier subsection.

At $i = 1, j = \text{NZ1}$,

$$\rho(T_{1,\text{NZ1}})c(T_{1,\text{NZ1}}) \frac{\partial T_{1,\text{NZ1}}}{\partial t} = \frac{1}{z_{\text{NZ1}+1/2} - z_{\text{NZ1}}} \left(k_{1,\text{NZ}+1/2} \frac{T_{1,\text{NZ1}+1} - T_{1,\text{NZ1}}}{z_{\text{NZ1}+1} - z_{\text{NZ1}}} - k_{1,\text{NZ1}} q_{\ell 5}^{\text{bem}} \right) + \frac{2}{r_{1+1/2}^2} \left(r_{1+1/2} k_{1/2,\text{NZ1}} \frac{T_{2,\text{NZ1}} - T_{1,\text{NZ1}}}{r_2 - r_1} \right) \quad (3.23)$$

At $i = 2, \dots, \text{NR1} - 1; j = \text{NZ1}$,

$$\rho(T_{i,\text{NZ1}})c(T_{i,\text{NZ1}}) \frac{\partial T_{i,\text{NZ1}}}{\partial t} = \frac{1}{z_{\text{NZ1}+1/2} - z_{\text{NZ1}}} \left(k_{i,\text{NZ}+1/2} \frac{T_{i,\text{NZ1}+1} - T_{i,\text{NZ1}}}{z_{\text{NZ1}+1} - z_{\text{NZ1}}} - k_{i,\text{NZ1}} q_{\ell 5+1-i}^{\text{bem}} \right) + \frac{2}{r_{i+1/2}^2 - r_{i-1/2}^2} \left(r_{i+1/2} k_{i+1/2,\text{NZ1}} \frac{T_{i+1,\text{NZ1}} - T_{i,\text{NZ1}}}{r_{i+1} - r_i} + r_{i-1/2} k_{i-1/2,\text{NZ1}} \frac{T_{i-1,\text{NZ1}} - T_{i,\text{NZ1}}}{r_i - r_{i-1}} \right) \quad (3.24)$$

At $i = \text{NR1}, j = \text{NZ1}$,

$$\rho(T_{\text{NR1},\text{NZ1}})c(T_{\text{NR1},\text{NZ1}}) \frac{\partial T_{\text{NR1},\text{NZ1}}}{\partial t} = \frac{(r_{\text{NR1}+1/2}^2 - r_{\text{NR1}-1/2}^2)}{v} \left(k_{\text{NR1},\text{NZ1}} \frac{T_{\text{NR1},\text{NZ1}+1} - T_{\text{NR1},\text{NZ1}}}{z_{\text{NZ1}+1} - z_{\text{NZ1}}} \right) + \frac{(r_{\text{NR1}+1/2}^2 - r_{\text{NR1}}^2)}{v} \left(k_{\text{NR1},\text{NZ1}} \frac{T_{\text{NR1},\text{NZ1}-1} - T_{\text{NR1},\text{NZ1}}}{z_{\text{NZ1}} - z_{\text{NZ1}-1}} \right) + \frac{(r_{\text{NR1}}^2 - r_{\text{NR1}-1/2}^2)}{v} \left(-k_{\text{NR1},\text{NZ1}} q_{\ell 4}^{\text{bem}} \right) + \frac{2(z_{\text{NZ1}+1/2} - z_{\text{NZ1}-1/2})}{v} \left(r_{\text{NR1}+1/2} k_{\text{NR1}+1/2,\text{NZ1}} \frac{T_{\text{NR1}+1,\text{NZ1}} - T_{\text{NR1},\text{NZ1}}}{r_{\text{NR1}+1} - r_{\text{NR1}}} \right) + \frac{2(z_{\text{NZ1}+1/2} - z_{\text{NZ1}})}{v} \left(r_{\text{NR1}-1/2} k_{\text{NR1}-1/2,\text{NZ1}} \frac{T_{\text{NR1}-1,\text{NZ1}} - T_{\text{NR1},\text{NZ1}}}{r_{\text{NR1}} - r_{\text{NR1}-1}} \right) + \frac{2(z_{\text{NZ1}} - z_{\text{NZ1}-1/2})}{v} \left(r_{\text{NR1}} k_{\text{NR1},\text{NZ1}} \frac{T_{\text{NR1}-1,\text{NZ1}} - T_{\text{NR1},\text{NZ1}}}{r_{\text{NR1}} - r_{\text{NR1}-1}} \right) \quad (3.25)$$

where $v = (r_{NR1+1/2}^2 - r_{NR1-1/2}^2)(z_{NZ1+1/2} - z_{NZ1}) + (r_{NR1+1/2}^2 - r_{NR1}^2)(z_{NZ1} - z_{NZ1-1/2})$

At $i = NR1, j = 1$

$$\begin{aligned} \rho(T_{NR1,1})c(T_{NR1,1}) \frac{\partial T_{NR1,1}}{\partial t} = & \frac{1}{z_{1+1/2}} \left(k_{NR1,1+1/2} \frac{T_{NR1,2} - T_{NR1,1}}{z_2 - z_1} - h(T_{NR1,1} - T_\infty) + \tilde{q} \right) \\ & + \frac{2}{(r_{NR1+1/2}^2 - r_{NR1}^2)} \left(r_{NR1+1/2} k_{NR1+1/2,1} \frac{T_{NR1+1,1} - T_{NR1,1}}{r_{NR1+1} - r_{NR1}} + r_{NR1} (-k_{NR1,1} q_{\ell 3}^{bem}) \right) \end{aligned} \quad (3.26)$$

At $i = NR1; j = 2, \dots, NZ1 - 1$

$$\begin{aligned} \rho(T_{NR1,j})c(T_{NR1,j}) \frac{\partial T_{NR1,j}}{\partial t} = & \frac{1}{z_{j+1/2} - z_{j-1/2}} \left(k_{NR1,j+1/2} \frac{T_{NR1,j+1} - T_{NR1,j}}{z_{j+1} - z_j} + k_{NR1,j-1/2} \frac{T_{NR1,j-1} - T_{NR1,j}}{z_j - z_{j-1}} \right) \\ & + \frac{2}{(r_{NR1+1/2}^2 - r_{NR1}^2)} \left(r_{NR1+1/2} k_{NR1+1/2,j} \frac{T_{NR1+1,j} - T_{NR1,j}}{r_{NR1+1} - r_{NR1}} + r_{NR1} (-k_{NR1,j} q_{\ell 3-1+j}^{bem}) \right) \end{aligned} \quad (3.27)$$

3.1.3 Time marching scheme for FDM

The basic solution scheme adopted for marching in time is the Crank-Nicholson method. This is an $O(\Delta t^2, \Delta x^2)$ accurate method. The scheme is implicit and stable for any Δt value and it is imposed on the FDM part of the problem and due to coupling at the common boundary, the BEM part comes into the equation indirectly. The discretized equation is given below in operator form for the point (i, j) .

$$\frac{T_{i,j}^{k+1} - T_{i,j}^k}{\Delta t} = \alpha \left(\frac{1}{\rho c} \nabla^2 T \right)_{i,j}^{k+1} + (1-\alpha) \left(\frac{1}{\rho c} \nabla^2 T \right)_{i,j}^k \quad (3.28)$$

where $\alpha = 1/2$ for the Crank-Nicholson method. The discretized form of the ∇^2 that was derived from the FDM formulation given in the earlier subsection is substituted for each point. All quantities at previous time step 'k' are known and therefore could be evaluated. As for the time step 'k+1', all the $T_{i,j}$ terms are moved to the left-hand side (LHS) and the rest are moved to the right-hand side and evaluated at the previous iterate values. Thus the $T_{i,j}$ is updated. Where the discretized equation has the q^{bem} term, it would be split as shown earlier in Eqn. (3.12) to $q^{\text{bem_dia}}$ and $q^{\text{bem_offdia}}$. The former term contains the coefficient that multiplies to the $T_{i,j}$ ($\equiv T_\ell$ in BEM) and thus could be incorporated in the LHS, and the latter could be evaluated at the previous iterate temperature values.

Every iteration cycle of the FDM gives an update of the temperatures at the common boundary and using them the BEM system of equations given by Eqn. (3.6) is solved, thus updating its unknowns. In the moving boundary of the BEM domain, these updated u_n velocities, will change the boundary profile and thereby the boundary integrals associated with it as field points or source points. This brings a time dependence for this integral coefficients and thereby an implicitness to the BEM formulation. The iterations are done until convergence is obtained. After that, at internal points corresponding to the nodes of the domain elements of the current BEM domain, the temperature values are computed. These and the earlier computed boundary values are used as initial values for the domain integral and the boundary integral respectively, in the next time step.

3.2 Space-Time method for the thin layer equations

This method is based on the publications of Molls and Molls [1998] and Chang [1995]. In their work, this method is basically applied to transient 1-D hyperbolic systems in Cartesian coordinates. In the present work the method has been extended to the axisymmetric case where a transient 1-D hyperbolic system is solved. To apply this method, the evolution equations are first recast so that the Green's theorem could be applied in the space-time domain. Define the following primary variables.

$$\phi_1 = \delta \quad ; \quad \phi_2 = u_1 \delta \quad ; \quad \phi_3 = \bar{T} \delta \quad (3.29)$$

Substituting in the transient governing Eqns. (2.31)-(2.33), the following system is obtained.

$$\begin{aligned}
& \frac{\partial}{\partial t} \begin{pmatrix} \phi_1 \\ \phi_2 \\ \phi_3 \end{pmatrix} + \frac{1}{r} \frac{\partial}{\partial \varphi} r \begin{bmatrix} \left(\frac{2}{3} \phi_2 - \varphi \dot{\phi}_1 \right) \frac{1}{s} \\ \left(\frac{4}{5} \frac{\phi_2^2}{\phi_1} - \varphi \dot{\phi}_2 + \frac{3 p \phi_1}{2 \rho_\ell} \right) \frac{1}{s} \\ \left(\frac{5}{6} \frac{\phi_3 \phi_2}{\phi_1} - \frac{1}{6} \phi_2 T_0 - \varphi \dot{\phi}_3 \right) \frac{1}{s} \end{bmatrix} \\
&= \begin{bmatrix} -\frac{\dot{\phi}_1}{s} - (\tilde{v}_1 - v_0) \\ -\frac{\dot{\phi}_2}{s} + \frac{3 p}{2 \rho_\ell s} \frac{\partial \phi_1}{\partial \varphi} - \frac{3 \tilde{v}_1 \phi_2}{2 \phi_1} + \frac{3}{2} g_x \phi_1 \\ -v \left(\frac{3 \phi_2}{\phi_1^2} \right) \\ -\frac{\dot{\phi}_3}{s} - 2 \frac{\tilde{v}_1 \phi_3}{\phi_1} + T_0 (\tilde{v}_1 - v_0) + \kappa_\ell \left. \frac{\partial T}{\partial y} \right|_{\ell-v} \\ -2 \kappa_\ell \frac{\phi_3}{\phi_1^2} + 2 \kappa_\ell \frac{T_0}{\phi_1} + \frac{\mu}{\rho_\ell c_\ell} \left(\frac{4}{3} \frac{\phi_2^2}{\phi_1^3} \right) \end{bmatrix} + \frac{1}{r} \begin{bmatrix} -\frac{\partial r}{\partial \varphi} \frac{\varphi \dot{\phi}_1}{s} \\ \left(\frac{3 p \phi_1}{2 \rho_\ell s} - \frac{\varphi \dot{\phi}_2}{s} \right) \frac{\partial r}{\partial \varphi} \\ -\frac{\varphi \dot{\phi}_3}{s} \frac{\partial r}{\partial \varphi} \end{bmatrix} \quad (3.30)
\end{aligned}$$

Let the above system of equations be denoted for brevity in the form given below and integrate it in a space-time domain giving due consideration to the fact of its axisymmetry in space.

$$\iint_{\Lambda} \left\{ \frac{\partial}{\partial t} [\phi_j] + \frac{1}{r} \frac{\partial}{\partial \varphi} r [f_j] \right\} r d\varphi dt = \iint_{\Lambda} \left\{ [S_j] + \frac{1}{r} [R_j] \right\} r d\varphi dt \quad (3.31)$$

Using the Green's theorem, the left-hand side could be expressed as a boundary integral. And applying it to an element defined as the conservation element (CE) and its boundary as $S(CE)$, this could be expressed as follows.

$$\oint_{S(CE)} [\mathbf{r} \mathbf{f}_j] dt - [\phi_j] r d\phi = \iint_{CE} [S_j] r d\phi dt + \iint_{CE} [R_j] d\phi dt \quad (3.32)$$

To integrate this expression, each argument is expanded around a mesh point in a Taylor series as done by Molls (1998) and it would be valid within the solution element that is defined for that mesh point. The solution element (SE) could be chosen in many different ways, but in this work it is defined to make the computation simpler and the resulting equations as explicit as possible. For any point (i,n) in the space-time domain and valid within the solution element encompassing it, the Taylor series expansions of the functions in Eqn. (3.32) up to first order is given by the following equations.

$$(\phi_j) = (\phi_j)_i^n + (\phi_{j\phi})_i^n (\phi - \phi_i) + (\phi_{jt})_i^n (t - t_n) + O(\Delta\phi^2, \Delta t^2) \quad (3.33)$$

$$(\mathbf{f}_j) = (\mathbf{f}_j)_i^n + (\mathbf{f}_{j\phi})_i^n (\phi - \phi_i) + (\mathbf{f}_{jt})_i^n (t - t_n) + O(\Delta\phi^2, \Delta t^2) \quad (3.34)$$

$$(S_j) = (S_j)_i^n + (S_{j\phi})_i^n (\phi - \phi_i) + (S_{jt})_i^n (t - t_n) + O(\Delta\phi^2, \Delta t^2) \quad (3.35)$$

$$(R_j) = (R_j)_i^n + (R_{j\phi})_i^n (\phi - \phi_i) + (R_{jt})_i^n (t - t_n) + O(\Delta\phi^2, \Delta t^2) \quad (3.36)$$

The SE and CE with respect to the grid points are shown in Fig. 3.3. It is seen that for the point (i,n) , the SE is the domain given by,

$$\{(\varphi_{i-1/2}, \varphi_{i+1/2}) \times [t_n, t_{n+1/2})\} \cup \{(t, \varphi) : t \in [t_{n-1/2}, t_n], \varphi = \varphi_i\}.$$

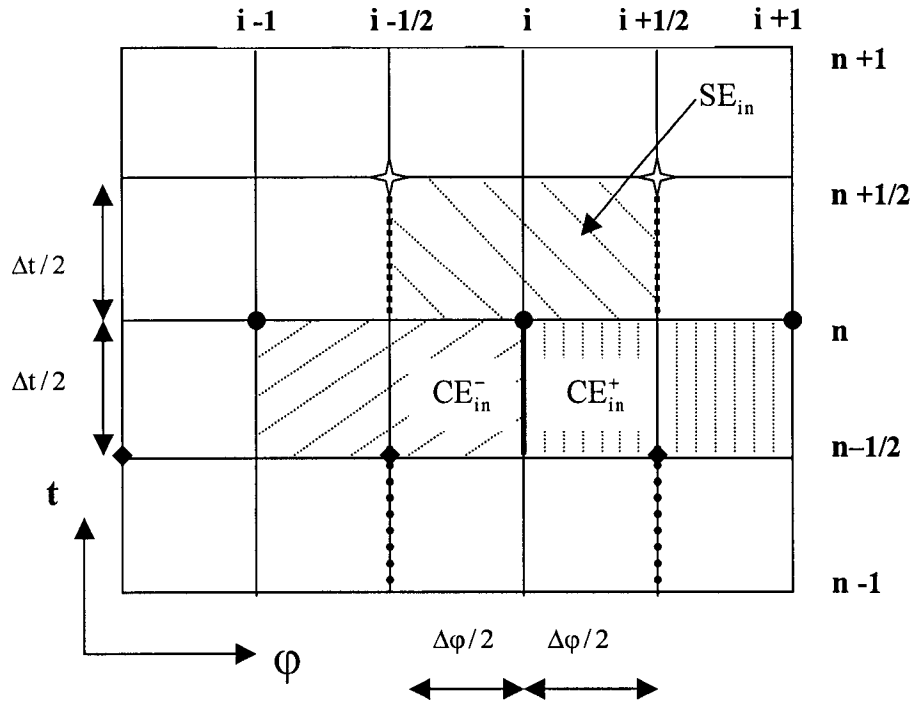


Figure 3.3 SEs and CEs of space-time grid

To obtain a flux conservation equation for the point (i,n) , the integral Eqn. (3.32) is applied to the domains CE_{in}^+ and CE_{in}^- separately. This would give two separate equations for each primary variable at the point (i,n) . Combining these two equations, it would be possible to get an explicit equation for each $(\phi_j)_i^n$. But, unlike in the 1-D

Cartesian case, the axisymmetric case has 'r' in the spatial integration, therefore this would introduce an additional derivative term $(\phi_{j\varphi})_i^n$ as seen below.

Apply the integration to the CE_{in}^+ domain element and where the appropriate Taylor series expansion is used for each of the integrand in Eqn. (3.32). The point of expansion for the Taylor series depends on the solution element where this integrand lies. Thus the following discrete form is obtained. In this case the integrations with respect to time and space are simple to perform due to the use of Taylor series polynomials. The spatial integration coefficients 'A's are obtained from the spatial integration of the Taylor polynomial and are given in Appendix B.

$$(\phi_j)_i^n [A_0^+]_i^n + (\phi_{j\varphi})_i^n [A_1^+]_i^n - r_i (f_j)_i^n \frac{\Delta t}{2} + r_i (f_{jt})_i^n \frac{\Delta t^2}{8} + (B_j)_{i+1/2}^{n-1/2} = (D_j)_{i+1/2}^{n-1/2} \quad (3.37)$$

Here $(B_j)_{i+1/2}^{n-1/2}$ is the contribution to the boundary integral from the previous half time step and staggered forward half step in space while $(D_j)_{i+1/2}^{n-1/2}$ is the contribution from the domain integral based on the same space and time step. They are defined below.

$$\begin{aligned} (B_j)_{i+1/2}^{n-1/2} = & -(\phi_j)_{i+1/2}^{n-1/2} [A_0^+]_{i+1/2}^{n-1/2} - (\phi_{j\varphi})_{i+1/2}^{n-1/2} [A_1^+]_{i+1/2}^{n-1/2} \\ & + r_{i+1/2} (f_j)_{i+1/2}^{n-1/2} \frac{\Delta t}{2} + r_{i+1/2} (f_{jt})_{i+1/2}^{n-1/2} \frac{\Delta t^2}{8} \end{aligned} \quad (3.38)$$

$$\begin{aligned}
(D_j)_{i+1/2}^{n-1/2} &= \frac{\Delta t}{2} \left[(S_j)_{i+1/2}^{n-1/2} [A_0^+]_{i+1/2}^{n-1/2} + (S_{j\phi})_{i+1/2}^{n-1/2} [A_1^+]_{i+1/2}^{n-1/2} \right] + \frac{\Delta t^2}{8} (S_{jt})_{i+1/2}^{n-1/2} [A_0^+]_{i+1/2}^{n-1/2} \\
&+ \frac{\Delta t}{2} \left[(R_j)_{i+1/2}^{n-1/2} [A_2^+]_{i+1/2}^{n-1/2} + (R_{j\phi})_{i+1/2}^{n-1/2} [A_3^+]_{i+1/2}^{n-1/2} \right] + \frac{\Delta t^2}{8} (R_{jt})_{i+1/2}^{n-1/2} [A_2^+]_{i+1/2}^{n-1/2}
\end{aligned} \tag{3.39}$$

Similarly for the CE_{in}^- element the conservation equation could be derived as given below.

$$(\phi_j)_i^n [A_0^-]_i^n + (\phi_{j\phi})_i^n [\tilde{A}_1^-]_i^n + r_i (f_j)_i^n \frac{\Delta t}{2} - r_i (f_{jt})_i^n \frac{\Delta t^2}{8} + (B_j)_{i-1/2}^{n-1/2} = (D_j)_{i-1/2}^{n-1/2} \tag{3.40}$$

Here $(B_j)_{i-1/2}^{n-1/2}$ and $(D_j)_{i-1/2}^{n-1/2}$ are defined as earlier.

$$\begin{aligned}
(B_j)_{i-1/2}^{n-1/2} &= -(\phi_j)_{i+1/2}^{n-1/2} [A_0^-]_{i-1/2}^{n-1/2} - (\phi_{j\phi})_{i-1/2}^{n-1/2} [A_1^-]_{i-1/2}^{n-1/2} \\
&- r_{i-1/2} (f_j)_{i-1/2}^{n-1/2} \frac{\Delta t}{2} - r_{i-1/2} (f_{jt})_{i-1/2}^{n-1/2} \frac{\Delta t^2}{8}
\end{aligned} \tag{3.41}$$

$$\begin{aligned}
(D_j)_{i-1/2}^{n-1/2} &= \frac{\Delta t}{2} \left[(S_j)_{i-1/2}^{n-1/2} [A_0^-]_{i-1/2}^{n-1/2} + (S_{j\phi})_{i-1/2}^{n-1/2} [A_1^-]_{i-1/2}^{n-1/2} \right] + \frac{\Delta t^2}{8} (S_{jt})_{i-1/2}^{n-1/2} [A_0^-]_{i-1/2}^{n-1/2} \\
&+ \frac{\Delta t}{2} \left[(R_j)_{i-1/2}^{n-1/2} [A_2^-]_{i-1/2}^{n-1/2} + (R_{j\phi})_{i-1/2}^{n-1/2} [A_3^-]_{i-1/2}^{n-1/2} \right] + \frac{\Delta t^2}{8} (R_{jt})_{i-1/2}^{n-1/2} [A_2^-]_{i-1/2}^{n-1/2}
\end{aligned} \tag{3.42}$$

Summing Eqns. (3.37) and (3.40), gives the final discretized equation.

$$\begin{aligned}
& \left([A_0^+]_i^n + [A_0^-]_i^n \right) (\phi_j)_i^n + \left([A_1^+]_i^n + [A_1^-]_i^n \right) (\phi_{j\phi})_i^n \\
&= (D_j)_{i+1/2}^{n-1/2} - (B_j)_{i+1/2}^{n-1/2} + (D_j)_{i-1/2}^{n-1/2} - (B_j)_{i-1/2}^{n-1/2}
\end{aligned} \tag{3.43}$$

In this equation the LHS gives not only the $(\phi_j)_i^n$, but also the derivative of the primary variable with respect to ϕ at the 'n'th time step, $(\phi_{j\phi})_i^n$, which needs to be computed using the forward and backward formula given in Chang (1995). Therefore this necessitates an iterative process. The RHS of the equation could be explicitly computed and the method of evaluating the different derivatives of the terms in it that comes from the coefficients of the Taylor series expansion of integrands in Eqn. (3.32), are given in Appendix B.

3.2.1 Boundary conditions for the Space-Time formulation

To solve the system of thin layer equations in this space-time formulation requires initial and boundary conditions. It is realistic to set the initial velocity in the whole layer as zero. To get the initial temperature and the thickness of the layer, the conduction model is run until the surface area around the axis reaches a temperature above that of the melting temperature. The region above this temperature will give the liquid volume of the thin layer and this could be used to compute its thickness. The temperature profile will give the initial values and the interface between solid and the liquid region will give the initial condition for it.

The boundary conditions at the symmetric axis and the out flow end are required for this model. Even though this is a transient 1-D hyperbolic system, for the implementation of the numerical scheme, it is required to provide boundary conditions at the outflow boundary. It is of paramount importance that these boundary conditions do not introduce

artificial reflections thus creating oscillations and ultimately instabilities. It is also important for the accuracy of the results that they do not impede the smooth outflow of the molten material. At the symmetric axis, zero lateral gradients for the temperature and the thickness, and zero values for the velocity are imposed. Therefore, this boundary condition in the primary variables of the space-time method can be given as,

$$\begin{aligned}
 \text{At } r = 0 \Rightarrow x = 0 \Rightarrow \varphi = 0: \quad \frac{\partial \delta}{\partial x} = 0 \Rightarrow \frac{\partial \phi_1}{\partial \varphi} = 0 \\
 u_1 = 0 \Rightarrow \phi_2 = 0 \\
 \frac{\partial \bar{T}}{\partial x} = 0 \Rightarrow \frac{\partial \phi_3}{\partial \varphi} = 0
 \end{aligned} \tag{3.44}$$

As for the open boundary where the outflow of the melt ejection happens, a second derivative condition is imposed. The justification of this is based on the fact that this would make any gradients continuous and also it is straightforward to implement. Similar conditions are seen imposed on outflow boundary conditions in the compressible flow simulations whose governing equations are similar to the thin layer equations. This implementation of the boundary condition removed the reflections occurring at this edge of the boundary in a very simple manner. The boundary conditions at the outflow boundary can be given as,

$$\begin{aligned}
\text{At } x = s(t) \Rightarrow \varphi = 1: \quad \frac{\partial^2 \delta}{\partial x^2} = 0 &\Rightarrow \frac{\partial^2 \phi_1}{\partial \varphi^2} = 0 \\
\frac{\partial^2 u_1}{\partial x^2} = 0 &\Rightarrow \frac{\partial^2 \phi_2}{\partial \varphi^2} = 0 \\
\frac{\partial^2 \bar{T}}{\partial x^2} = 0 &\Rightarrow \frac{\partial^2 \phi_3}{\partial \varphi^2} = 0
\end{aligned} \tag{3.45}$$

The implementation of this boundary condition is achieved by computing the primary variables at the end node using a third order backward differencing scheme as given below for the point N at the end of the spatial domain.

$$(\phi_j)_N = \frac{1}{2} \left[5(\phi_j)_{N-1} - 4(\phi_j)_{N-2} + (\phi_j)_{N-3} \right] \quad \text{where } j=1,3 \tag{3.46}$$

4.0 RESULTS FROM SIMULATIONS

Results from the simulations to test the different parts of the model are given in this chapter. The first test was to check the conduction part of the model. This verified the effectiveness of the FDM and the BEM formulations and the coupling of the two methods. In these tests for the model verification, varying heat fluxes were applied from the bottom surface and the rest of the surfaces were kept insulated as shown in Fig. 4.1. As seen from this figure the BEM region is a small area within the larger region where the rest of the outer area comprises the FDM region. The dimensional notations and the boundary conditions are given with the figure. These tests were basically designed to simulate the heat conduction problem with two different cases of applied laser flux. In the first case, the applied laser flux was modeled as a constant heat flux and in the second case as a heat flux varying with radial distance. In both the cases the results were compared to the analytical solutions which are given in Appendix C. In the next simulation the moving boundary part of the code was tested. In this test a very simple case of constant heat flux was applied along the moving boundary and the whole region was initially kept at the melting temperature as illustrated in Fig. 4.41. This special test case has an analytical solution. The above test cases were designed to validate the coupled BEM-FDM model. To increase the confidence in the model, convergence of the results with grid refinement was also computed for the constant heat flux case.

To test the TLM part of the model, it was run with various laser fluxes ranging from $1.5 \times 10^{10} \text{ W/m}^2$ to $5.0 \times 10^{10} \text{ W/m}^2$. The initial conditions and the dimension of the

laser spot size are given in Sec. 4.6. The test was done for mild steel and the solid substrate was considered as a semi-infinite domain for heat conduction. The whole solid-liquid interface was considered as flat with no curvature effects. The simulations were run until steady state was obtained. This part was done using the Space-Time numerical method. To check this method's efficacy, it was utilized to solve a simplified set of shallow water equations, which had analytical solutions. The convergence of the results with grid refinement was computed to show the effectiveness of this method.

4.1 Simulation for the conduction regime

Initial condition: $T(r, z, 0) = T_0$

Boundary conditions:

$$-k \frac{\partial T}{\partial z} = Q \quad \text{at } z = 0;$$

$$\frac{\partial T}{\partial n} = 0 \quad \text{rest of the boundaries}$$

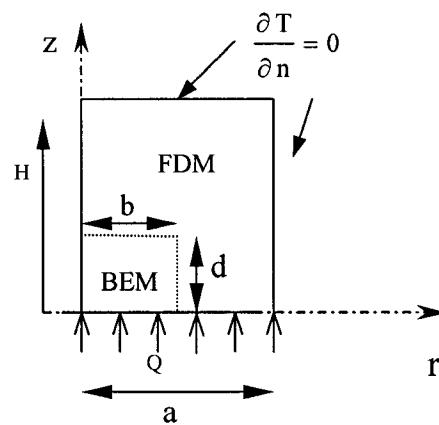


Figure 4.1 Configuration for the conduction regime

4.1.1 Test with a constant heat flux

In this case a constant heat flux Q with reference to Fig. 4.1 was applied from the bottom surface. Simulations were done with different parameters to verify the numerical formulation.

4.1.1.1 Constant heat flux - simulation 1

The simulation was done for the following values of,

$$H = 0.2 \text{ m}, a = 0.2 \text{ m}, d = 0.1 \text{ m}, b = 0.1 \text{ m}, k = 1 \text{ W/m/K}, \kappa = 1 \text{ m}^2/\text{s},$$

$$Q = Q_0 = 1 \text{ W/m}^2, T_0 = 1 \text{ K}$$

For both the FDM and the BEM $\Delta r = 0.01 \text{ m}$; $\Delta z = 0.01 \text{ m}$ constant grid size and a time step of $\Delta t = 0.00005 \text{ s}$ were used. The convergence criterion for the iterations in the FDM was set at average absolute error $\leq 1.0\text{E-}10$. The results were compared with the analytical results computed from the solution for the finite domain case given in Appendix C. Tables 4.1 - 4.3 give both the tabulated values from the model and the analytical solution for the different time intervals. It is seen that the relative error is $\sim 0.5\%$ initially from Table 4.1 for $t = 0.025 \text{ s}$ and goes up to $\sim 1.3\%$ as seen from Table 4.2 for $t = 0.5 \text{ s}$ and finally to $\sim 1.4\%$ from Table 4.3 for $t = 1.0 \text{ s}$. The increase in the relative error is understandable, where due to the simulation for a longer time period, the error accumulates from the increasing number of time steps. On the other hand the reduction of error with grid refinement as seen later from the convergence test, is a very important and a favorable characteristic. From these results it could be verified that the constant heat flux case performs to an acceptable accuracy and that the coupled BEM-FDM model is basically satisfactory in nature.

Temperature values for $t = 0.025s$						
z	Analytical	$r = 0.0$	$r = 0.05$	$r = 0.1$	$r = 0.15$	$r = 0.2$
0.00	1.191581	1.195953	1.195888	1.194996	1.194252	1.194058
0.01	1.181832	1.186212	1.186129	1.185238	1.184500	1.184306
0.02	1.172586	1.177041	1.176867	1.175976	1.175243	1.175052
0.03	1.163841	1.168310	1.168089	1.167205	1.166482	1.166294
0.05	1.147856	1.152226	1.151980	1.151131	1.150446	1.150270
0.08	1.127646	1.131635	1.131395	1.130682	1.130116	1.129970

Table 4.1 Constant flux simulation $t = 0.025s$

Temperature values for $t = 0.5s$						
z	Analytical	$r = 0.0$	$r = 0.05$	$r = 0.1$	$r = 0.15$	$r = 0.2$
0.00	3.566667	3.610338	3.610262	3.609331	3.608675	3.608505
0.01	3.556927	3.600597	3.600504	3.599571	3.598922	3.598753
0.02	3.547667	3.591425	3.591241	3.590310	3.589664	3.589496
0.03	3.538917	3.582692	3.582461	3.581536	3.580900	3.580736
0.05	3.522917	3.566603	3.566347	3.565458	3.564857	3.564703
0.08	3.502667	3.546001	3.545755	3.545005	3.544511	3.544382

Table 4.2 Constant flux simulation $t = 0.5s$

Temperature values for $t = 1.0s$						
z	Analytical	$r = 0.0$	$r = 0.05$	$r = 0.1$	$r = 0.15$	$r = 0.2$
0.00	6.066667	6.147085	6.146996	6.146016	6.145449	6.145302
0.01	6.056917	6.137344	6.137238	6.136257	6.135697	6.135550
0.02	6.047667	6.128174	6.127977	6.126998	6.126440	6.126295
0.03	6.038917	6.119444	6.119201	6.118228	6.117678	6.117536
0.05	6.022917	6.103363	6.103096	6.102160	6.101642	6.101509
0.08	6.002667	6.082780	6.082525	6.081733	6.081311	6.081199

Table 4.3 Constant flux simulation $t = 1.0s$

4.1.1.2 Constant heat flux - simulation 2

To create a more practically relevant simulation, the following case was done where the physical parameters are for mild steel and the size dimensions of the body with reference to Fig. 4.1 closely resemble that of laser drilling of objects. The BEM area was kept very small to less than 2.5% of the total area to reduce the computational resources.

$$a = 0.001 \text{ m}, d = 5 \times 10^{-6} \text{ m}, b = 5 \times 10^{-5} \text{ m}, k = 52.3 \text{ W / m / K}, \kappa = 1.536 \times 10^{-5} \text{ m}^2 / \text{s}, \\ Q_0 = 10^{10} \text{ W / m}^2, T_0 = 300 \text{ K}$$

As for the H, the depth in the z-direction, was chosen such that for all practical purposes it would mimic an infinite domain. This was done to reduce the number of computational elements and thereby reduce the computational time and memory requirements. The simulations were run until the laser incident surface temperature came close to the melting temperature. Therefore the computations were done for a time period of 3.0×10^{-6} seconds . As for the spatial discretizations, the following two levels were used:

$$\text{Level 1: } \Delta r = 2.5 \times 10^{-6} ; \Delta z = 2.5 \times 10^{-7} ; \text{ Level 2: } \Delta r = 1.25 \times 10^{-6} ; \Delta z = 1.25 \times 10^{-7}.$$

For the level 1, the time steps used were 10^{-7} s and 10^{-8} s and for the level 2 in addition to these time steps, two additional time steps of $\Delta t = 10^{-9}$ s and 10^{-10} s were used. The selection of these time steps was mainly dictated by the diffusion length scale ($\sim \sqrt{\kappa \Delta t}$) limitation on the FDM formulation. Here κ is the thermal diffusivity. The other reason is the time scale for reaching the melting temperature on the laser incident surface is of the

order $\sim 10^{-6}$ s. Therefore to resolve any transient characteristics $\Delta t \ll 10^{-6}$ s. The following are the diffusion length scales for the different time steps.

$$\Delta t = 10^{-7} \quad \text{length scale} \sim 1.2 \times 10^{-6}; \quad \Delta t = 10^{-8} \quad \text{length scale} \sim 3.8 \times 10^{-7}$$

$$\Delta t = 10^{-9} \quad \text{length scale} \sim 1.2 \times 10^{-7}; \quad \Delta t = 10^{-10} \quad \text{length scale} \sim 0.38 \times 10^{-7}$$

For the level 1 coarse grid discretization, Fig. 4.2 gives the profiles of temperature at the laser incident surface for the different Δt values. For comparison the analytical value is also given, which is computed from the constant flux infinite domain solution given in Appendix C. Fig. 4.3 gives the relative error for the BEM segment and similarly Fig 4.4 gives the relative error for the FDM segment. The relative error was broken into two figures so that it could be seen more clearly. It is seen from Fig. 4.3 that the error is less than 0.4% for both the time steps in the FDM region with the least error for the $\Delta t = 10^{-8}$ s as its diffusion length is less than the Δz value compared to the $\Delta t = 10^{-7}$ s case. As these cases are equivalent to the 1-D heat transfer case the Δr value does not come into consideration. On the other hand in the BEM region the relative error does not go down in the same fashion. The smaller time step means the maximum temperature variation would occur at a smaller length scale governed by the diffusion length scale. As the BEM is an integral method, it would bring a higher error in the domain integrals for a fixed discretization. This is seen from the relative error in the BEM area given by Fig. 4.3, where the error for the $\Delta t = 10^{-8}$ s is more than that for the $\Delta t = 10^{-7}$ s. Due to the coupling, this error influences the error in the FDM area that is near the BEM region as seen from Fig. 4.4.

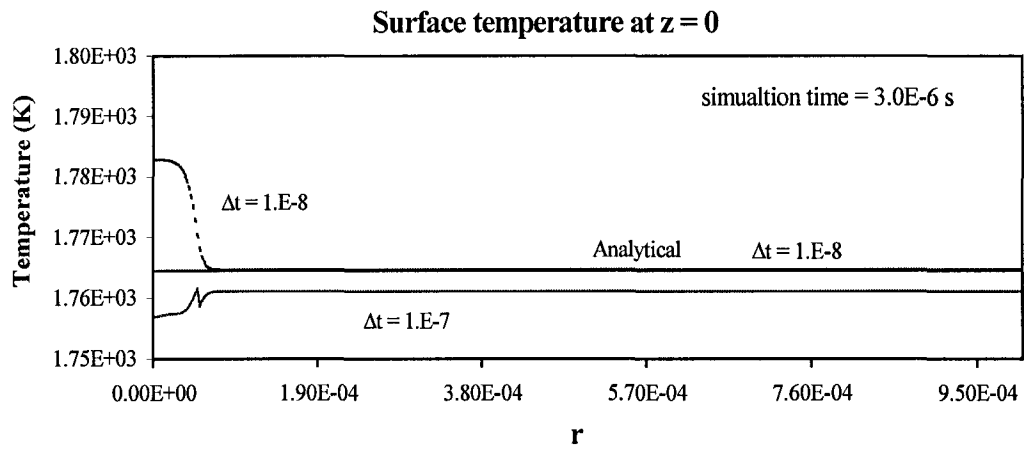


Figure 4.2 Temperature profile: constant heat flux – simulation 2, level 1

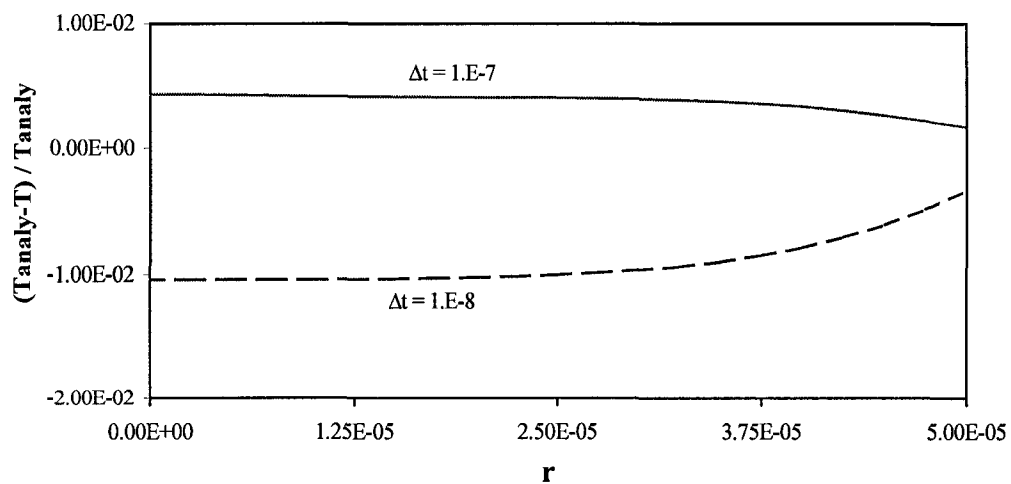


Figure 4.3 Relative error – BEM: constant heat flux – simulation 2, level 1

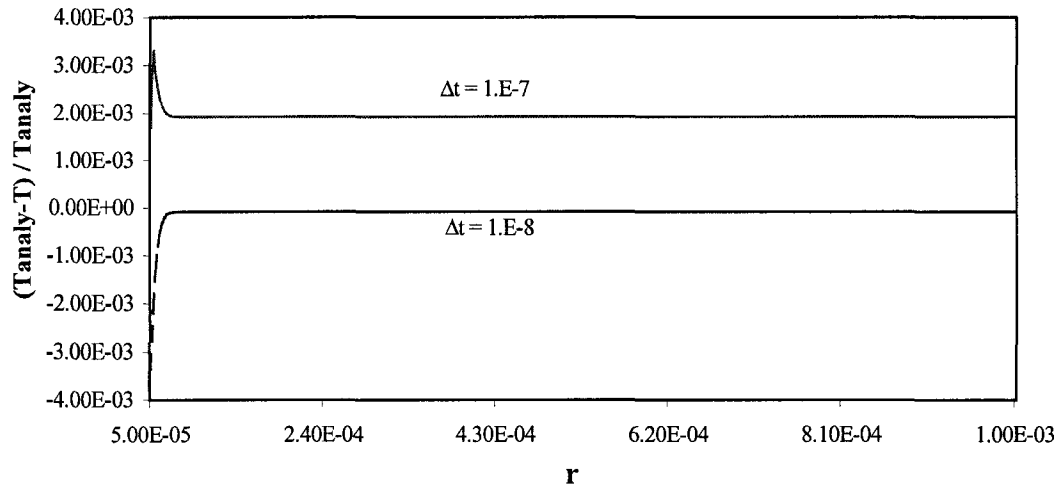


Figure 4.4 Relative error – FDM: constant heat flux – simulation 2, level 1

Similar to the earlier case, Figs. 4.5, 4.6 and 4.7 give the temperature profiles, the relative error in the BEM segment and the relative error in the FDM segment respectively for the level 2 discretization. It is apparent that the characteristics are similar for both the discretization levels. As the time step is reduced from $\Delta t = 10^{-7}$ s to $\Delta t = 10^{-10}$ s, the relative error in the FDM region goes down from $\sim 0.5\%$ to $\sim 0.2\%$ in the region away from the BEM segment. The highest error is for the $\Delta t = 10^{-7}$ s case. This could be attributed to having its diffusion length scale considerably larger than the Δz value. In the BEM segment and at the area near the BEM-FDM boundary the coupling effect is seen in an enhanced manner. As explained earlier, the larger time step would allow the better evaluation of integrals in the BEM and thus reduce error, which is seen from Fig. 4.6. It is seen that the largest maximum relative error is for the $\Delta t = 10^{-10}$ s and it is $\sim 16\%$. For $\Delta t = 10^{-8}$ s and $\Delta t = 10^{-7}$ s the relative error is $\sim 0.3\%$ and for $\Delta t = 10^{-9}$ s it is

~ 3%, which shows some form of compensation from each of the methods of their strengths and weaknesses.

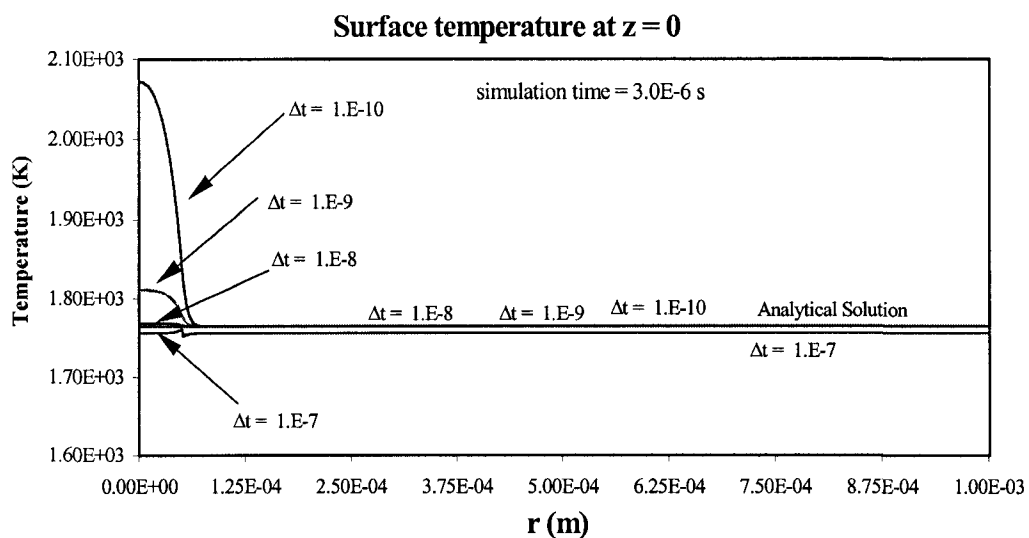


Figure 4.5 Temperature profile: constant heat flux – simulation 2 level 2

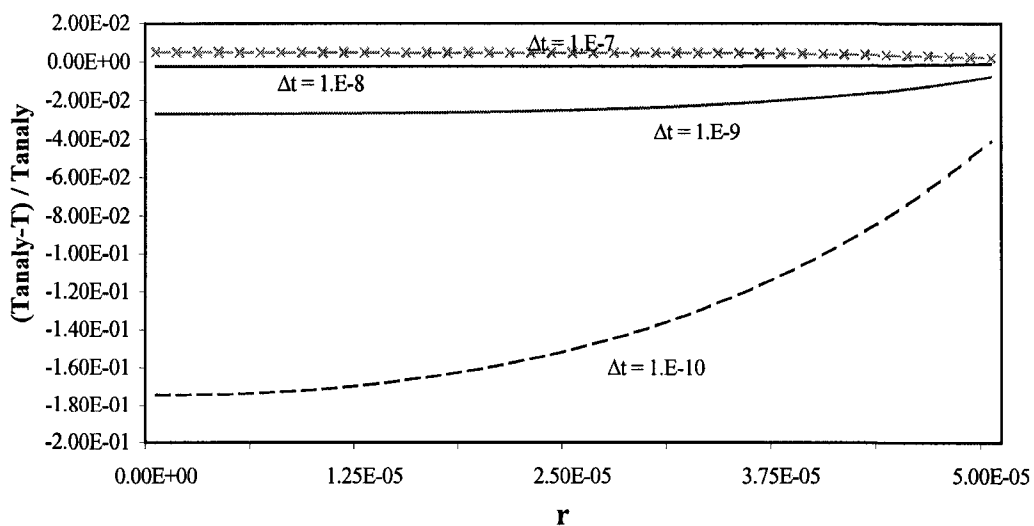


Figure 4.6 Relative error – BEM: constant heat flux – simulation 2, level 2

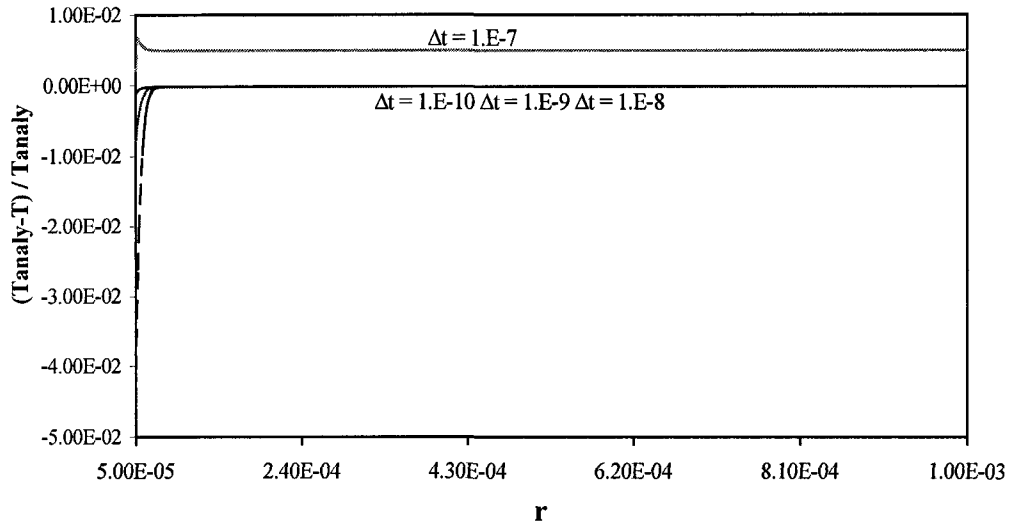


Figure 4.7 Relative error – FDM: constant flux – simulation 2, level 2

4.1.2 Test with a variable heat flux

In this case the heat flux Q , applied at the bottom boundary as given in Fig. 4.1, is varied according to the following equation,

$$-k \frac{\partial T}{\partial z} = Q = Q_0 \left\{ 1 - \left[3 \left(\frac{r}{a} \right)^2 - 2 \left(\frac{r}{a} \right)^3 \right] \right\} \quad \text{at } z = 0$$

This would model the variable heat flux of laser drilling with the maximum value of Q_0 at the axis. Several sets of simulations with different parameters were done as illustrated in the coming subsections.

4.1.2.1 Variable heat flux - simulation 1

This simulation was done with the following parameters:

$$H = 0.2 \text{ m}, a = 0.2 \text{ m}, d = 0.1 \text{ m}, b = 0.1 \text{ m}, k = 1 \text{ W/m/K}, \kappa = 1 \text{ m}^2/\text{s},$$

$$Q_0 = 8 \times 10^{-3} \text{ W/m}^2, T_0 = 1 \text{ K}$$

A time step of $\Delta t = 0.00005 \text{ s}$ was used in the computations. As for the spatial discretizations, the following three levels were used for both the BEM and the FDM regions: Level 1: $\Delta r = 0.01 \text{ m}; \Delta z = 0.01 \text{ m}$, Level 2: $\Delta r = 0.005 \text{ m}; \Delta z = 0.005 \text{ m}$ and Level 3: $\Delta r = 0.0025 \text{ m}; \Delta z = 0.0025 \text{ m}$. The results are compared with the analytical result given in Appendix C for the finite domain case. In this simulation the relative errors are plotted with respect to the radial distance and due to the initial condition the analytical value is of the order $\sim O(1)$. Simulations were done for three time intervals and at each interval, plots were done for three 'z' levels of $z = 0.0, 0.01, 0.02$ and 0.03 m . This was repeated for the three levels of spatial discretizations. It is seen from the plots that the relative error varies radially with the lowest being furthestmost from the axis. This is true for all the 'z' levels and for all the time intervals. This is expected from the flux condition as the applied heat flux diminishes in a radial fashion. For the time interval, $t = 0.25 \text{ s}$, it is seen from Figs. 4.8 - 4.10, that the maximum relative error goes down from 0.003% to 0.0002% with finer discretization. As for the time interval $t = 0.5 \text{ s}$, it is apparent from Figs. 4.11 - 4.13, that this ranges from 0.03% to 0.002% and as for the time interval $t = 1.0 \text{ s}$, given by Figs. 4.14 - 4.16, it varies from 0.06% to 0.003%. One of the reasons for the decrease in the error with the grid refinement is due to the second order method used in the FDM. This method as explained earlier has a diffusion length scale limit for the maximum refinement of the spatial discretization for a given time step. For this simulation it would be $\sim 0.00707 \text{ m}$ and this could be a problem at the level 3 of

the refinement where $\Delta r = 0.0025$; $\Delta z = 0.0025$. As the imposed maximum flux is small and also due to its radial variation, the heat flux would be very small on the applied heat flux boundary of the FDM region, therefore this problem is not that apparent in this case. The other important point is that the BEM does not have this constraint. As for the BEM, the refinement would give a more accurate evaluation of the boundary integrals and domain integrals, especially the ones near the flux boundary where there is a steep variation of the temperature. Thus the coupling of this two schemes is a balancing act.

The increase in error with time is due to the error accumulation from the number of time steps. Then there is also the fact that the coupling between the FDM and BEM could also have an effect on the final error. The overall low relative error shows the acceptable performance of the BEM-FDM coupled model under the variable flux condition.

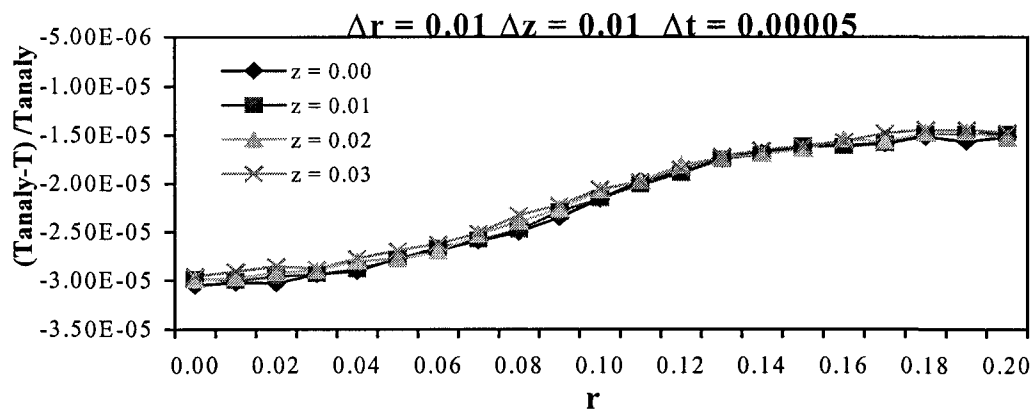


Figure 4.8 Relative error: variable heat flux – simulation 1 level 1, $t = 0.025s$

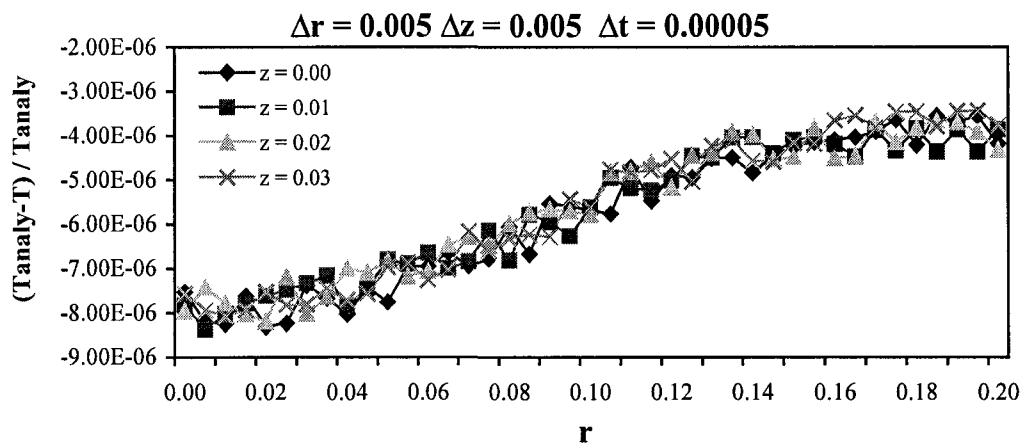


Figure 4.9 Relative error: variable heat flux – simulation 1 level 2, $t = 0.025s$

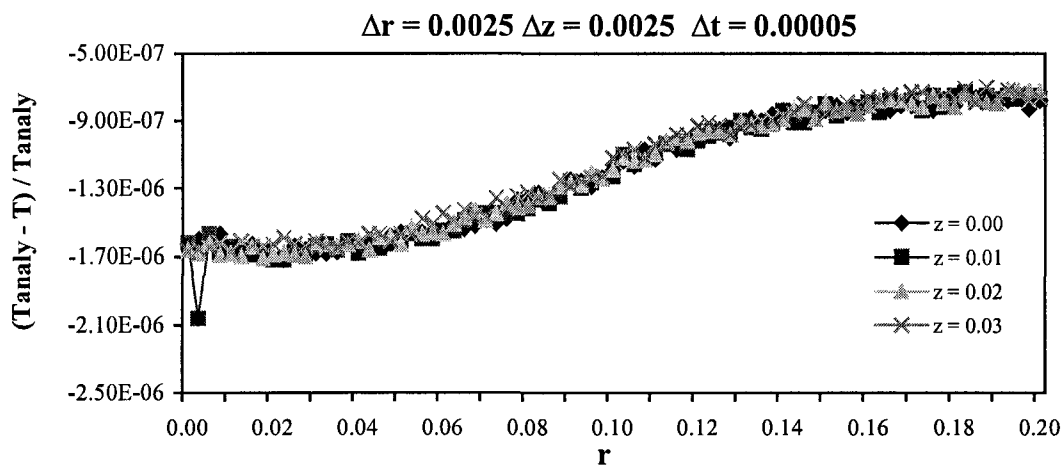


Figure 4.10 Relative error: variable heat flux – simulation 1 level 3, $t = 0.025s$

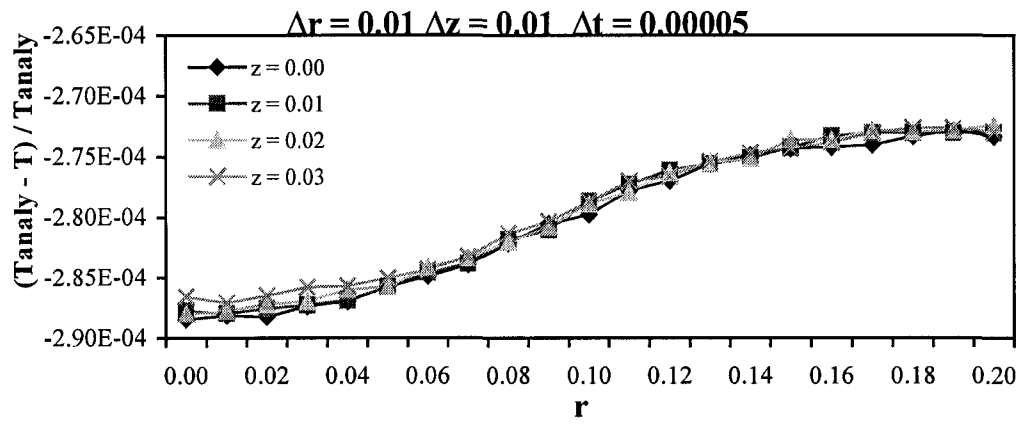


Figure 4.11 Relative error: variable heat flux – simulation 1 level 1, $t = 0.5s$

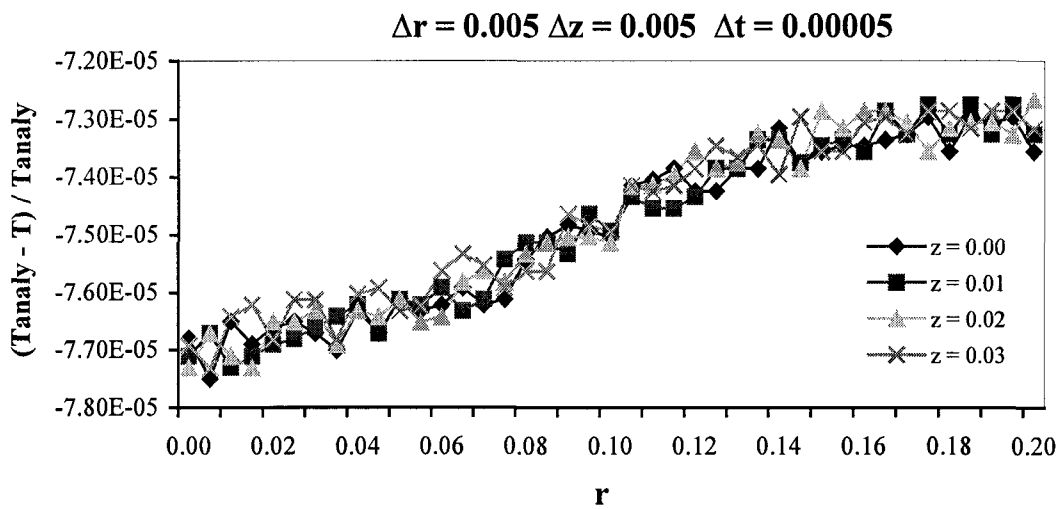


Figure 4.12 Relative error: variable heat flux – simulation 1 level 2, $t = 0.5s$

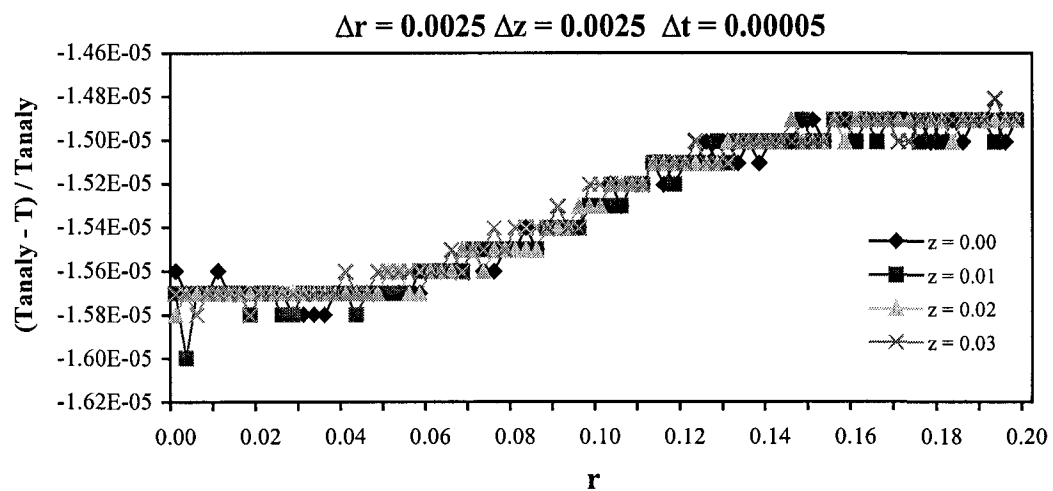


Figure 4. 13 Relative error: variable heat flux – simulation 1 level 3, $t = 0.5s$

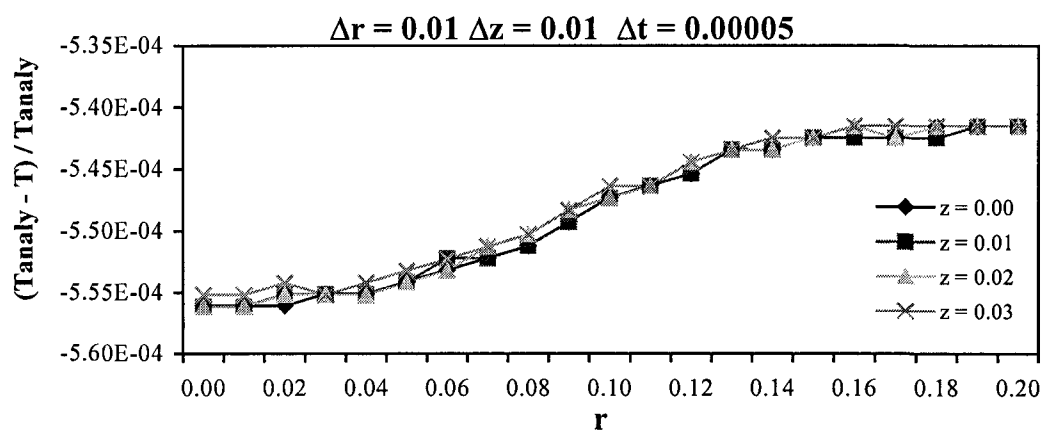


Figure 4. 14 Relative error: variable heat flux – simulation 1 level 1, $t = 1.0s$

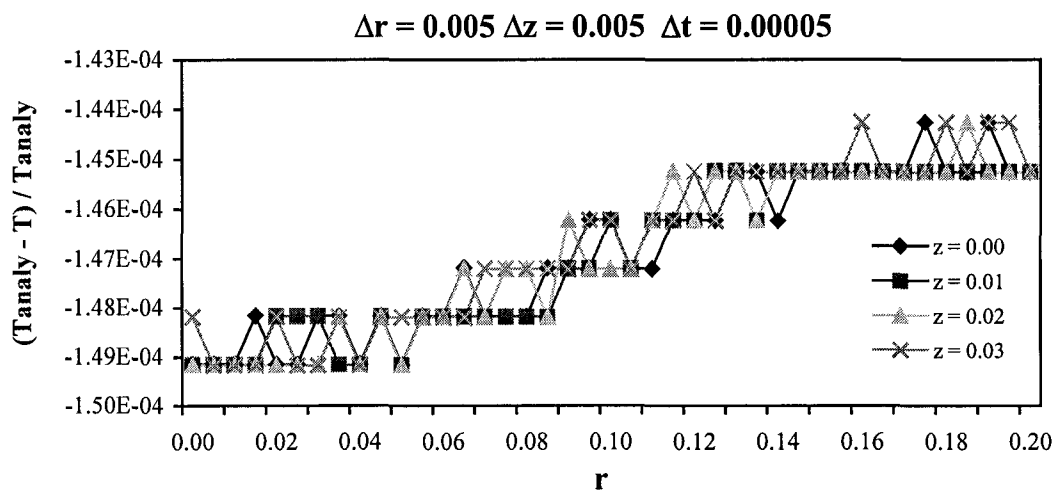


Figure 4.15 Relative error: variable heat flux – simulation 1 level 2, $t = 1.0s$

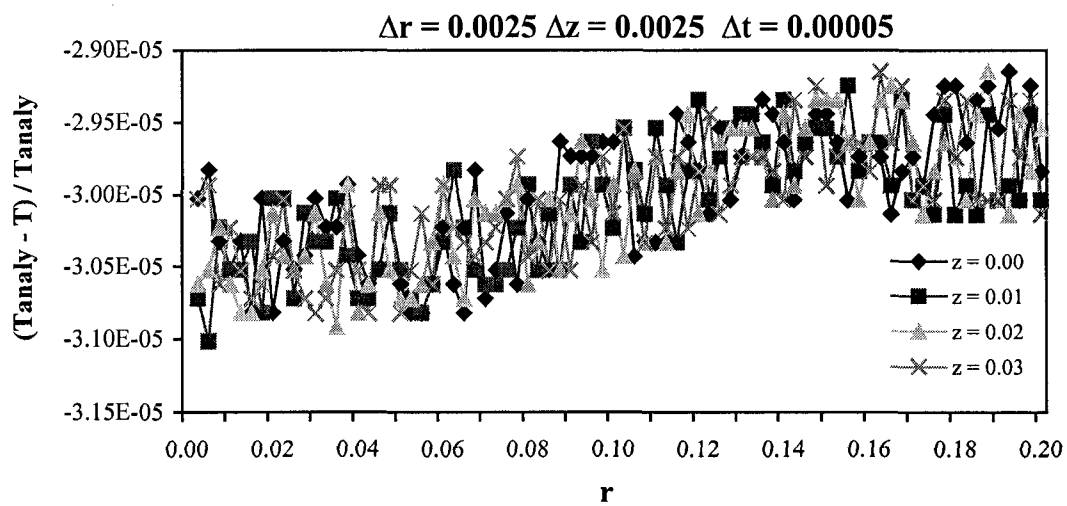


Figure 4.16 Relative error: variable flux – simulation 1 level 3, $t = 1.0s$

4.1.2.2 Variable heat flux - simulation 2

This simulation was done with the following parameters:

$$H = 0.2 \text{ m}, a = 0.2 \text{ m}, d = 0.1 \text{ m}, b = 0.1 \text{ m}, k = 1 \text{ W/m/K}, \kappa = 1 \text{ m}^2/\text{s},$$

$$Q_0 = 1.0 \text{ W/m}^2, T_0 = 1 \text{ K}$$

A time step of $\Delta t = 0.00005 \text{ s}$ was used in the computations. As for the spatial discretizations, following three levels were used for the BEM and the FDM regions:

Level 1: $\Delta r = 0.01$; $\Delta z = 0.01$, Level 2: $\Delta r = 0.005$; $\Delta z = 0.005$ and

Level 3: $\Delta r = 0.0025$; $\Delta z = 0.0025$.

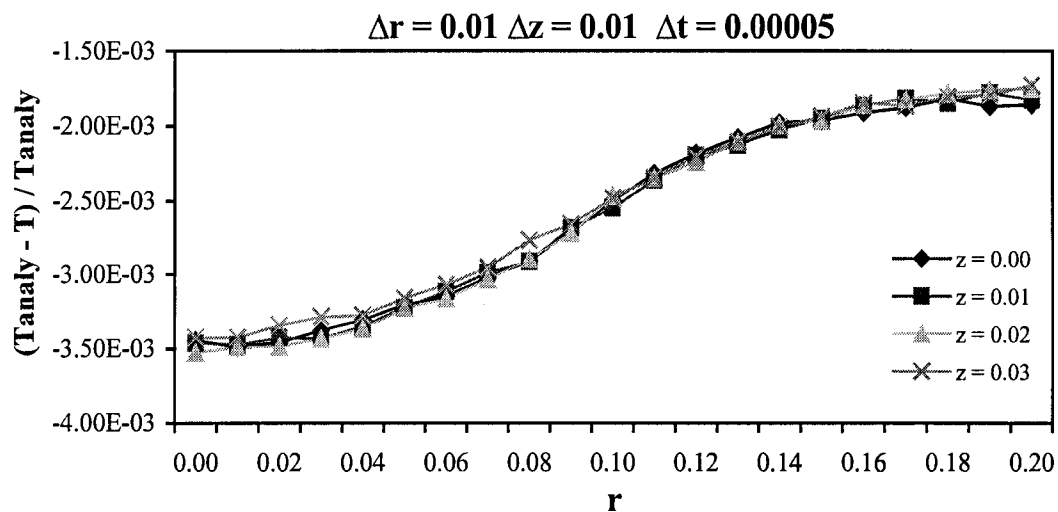


Figure 4.17 Relative error: variable flux – simulation 2 level 1, $t = 0.025 \text{ s}$

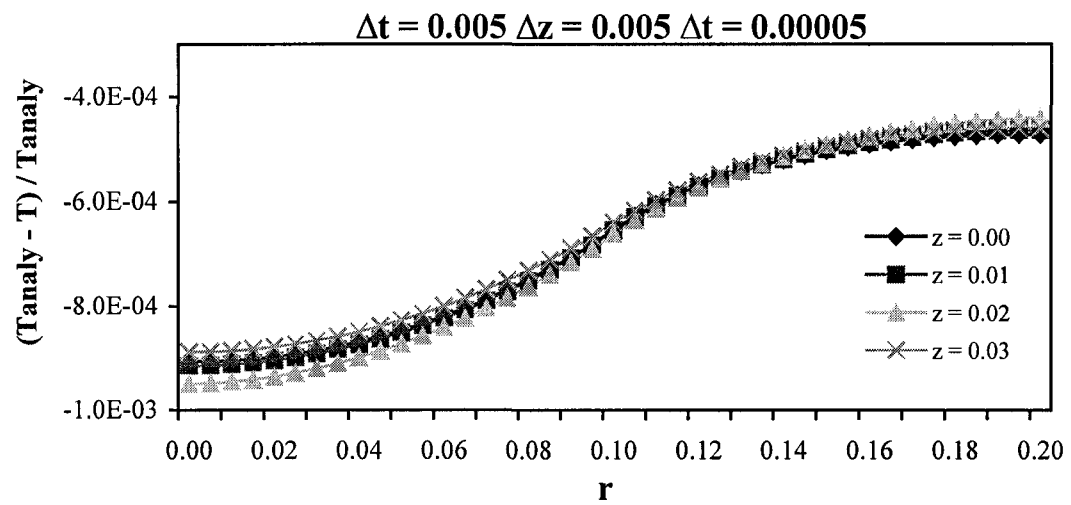


Figure 4.18 Relative error: variable flux – simulation 2 level 2, $t = 0.025s$

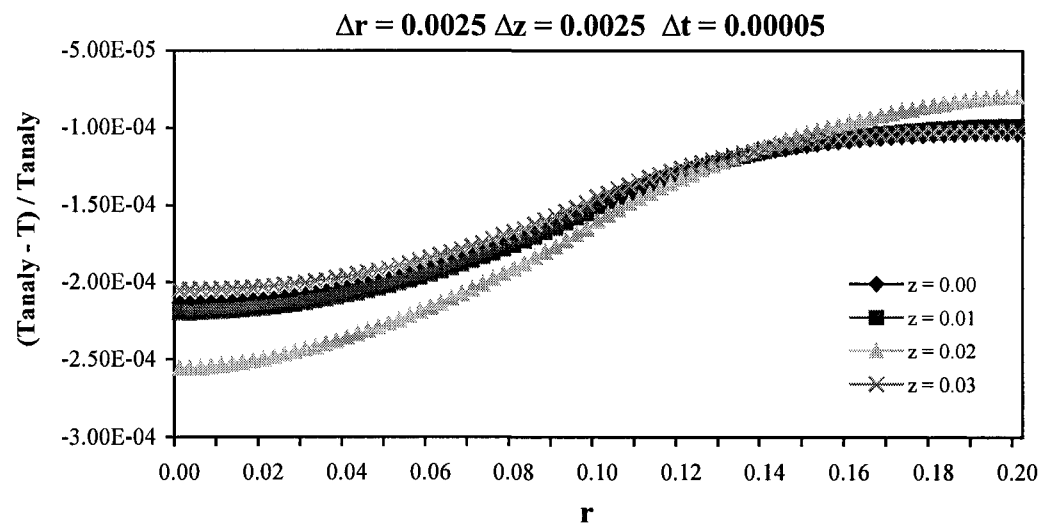


Figure 4.19 Relative error: variable flux – simulation 2 level 3, $t = 0.025s$

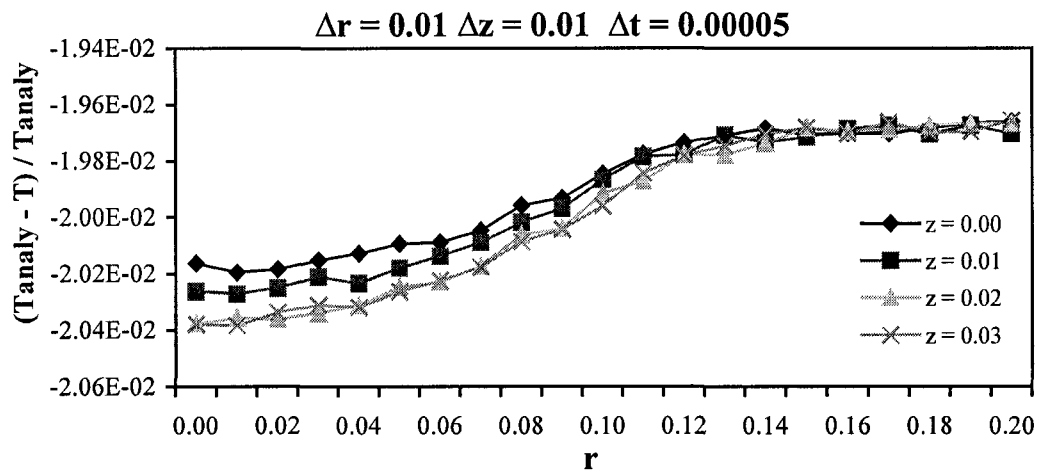


Figure 4.20 Relative error: variable flux – simulation 2 level 1, $t = 0.5s$

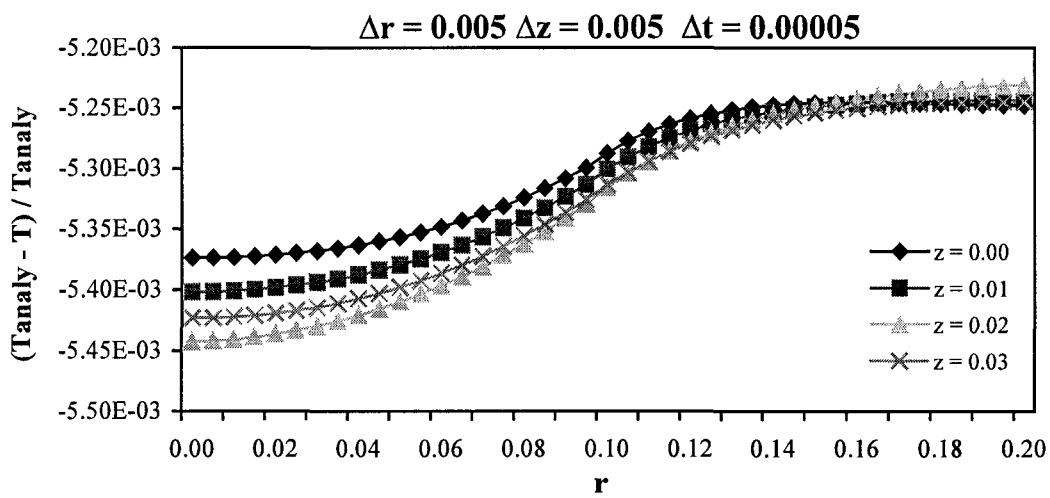


Figure 4.21 Relative error: variable flux – simulation 2 level 2, $t = 0.5s$

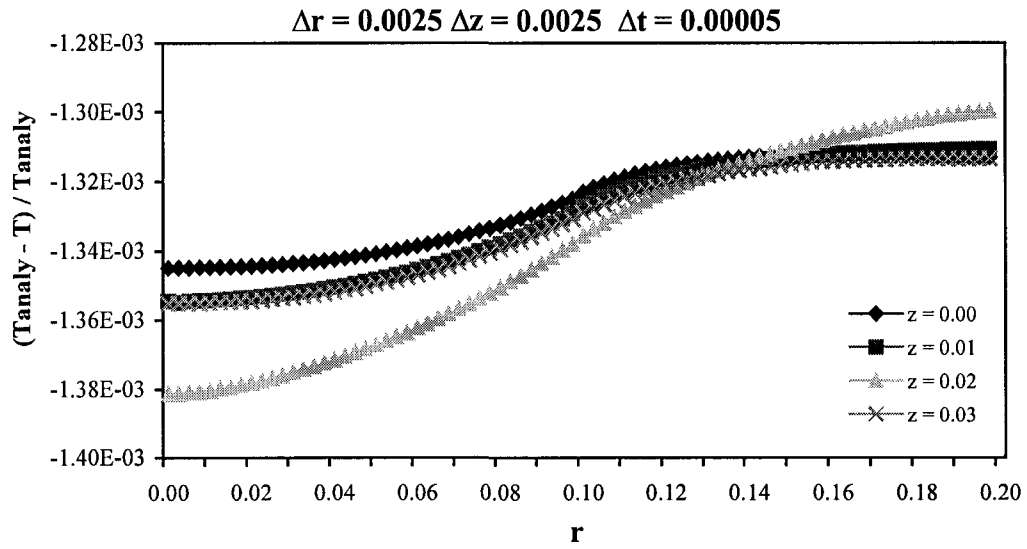


Figure 4.22 Relative error: variable flux – simulation 2 level 3, $t = 0.5s$

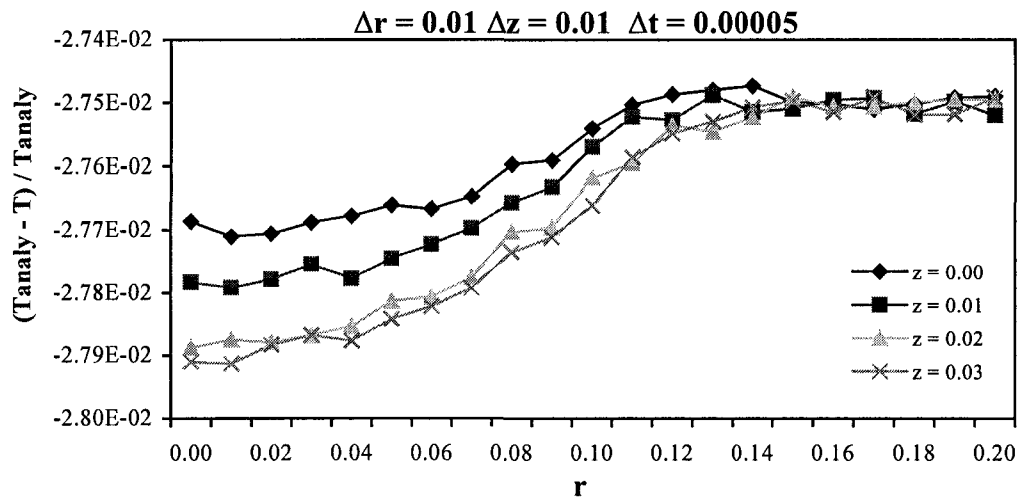


Figure 4.23 Relative error: variable flux – simulation 2 level 1, $t = 1.0s$

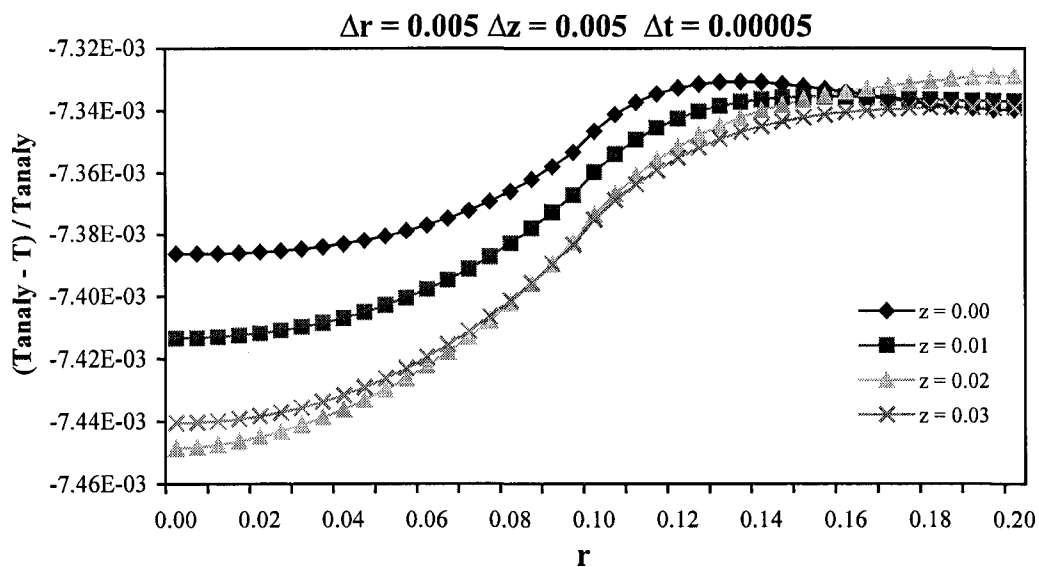


Figure 4.24 Relative error: variable flux – simulation 2 level 2, $t = 1.0s$

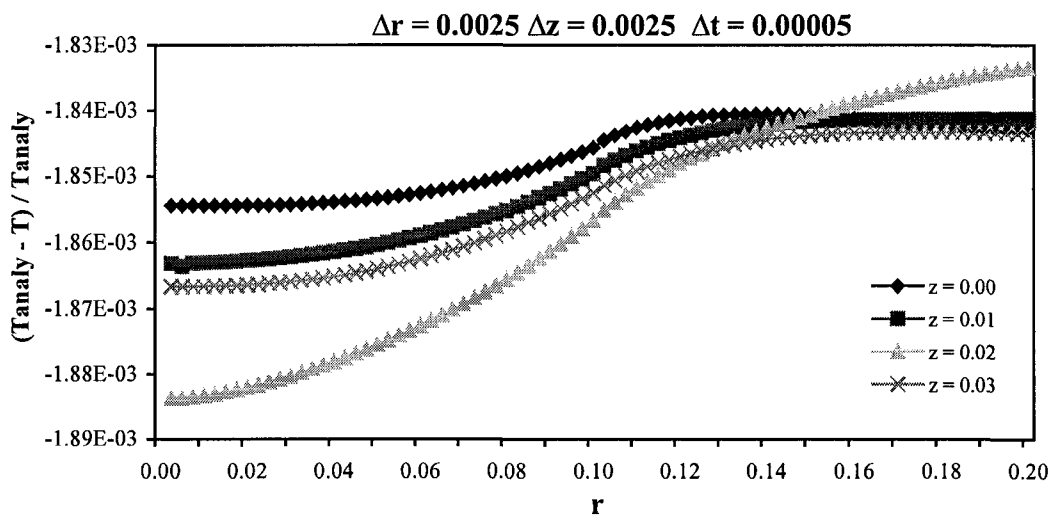


Figure 4.25 Relative error: variable flux – simulation 2 level 3, $t = 1.0s$

The results from this simulation show the same characteristics as the earlier simulation 1 results. With a higher power used in this case the relative errors are higher compared to the simulation 1 case. For the $t = 0.025\text{s}$ case it is seen from Figs. 4.17 – 4.19, that the maximum relative error is 0.35% for the coarse discretization and improves to 0.02% for the finer grid. As for the longer time results these numbers deteriorates a little bit, which is understandable due to the accumulation of error. For the $t = 0.5\text{s}$ case given by Figs. 4.20 - 4.22 these numbers varies from 2% to 0.14%, and for the $t = 1.0\text{s}$ case given by Figs. 4.23 - 4.25, it varies from 2.8% to 0.19%. Thus it is seen that the refinement of the grid do bring about an improvement in the relative error and also the fact that the number of time steps increase the accumulation error. Compared to the earlier simulation 1 for very low power, this one has a higher relative error for the each corresponding discretization and the time level. It is also seen that the highest error is near the axis, which has the highest magnitude for the applied heat flux.

4.1.2.3 Variable heat flux - simulation 3

To create a more practically relevant simulation for the variable heat flux case such as found in laser drilling, the following case was done. In this case the physical parameters are for mild steel and the size dimensions of the body with reference to Fig. 4.1 closely resemble the laser drilling of objects. The BEM area was kept small to around 2.5% of the total area to reduce the computational resources.

$$a = 0.001 \text{ m}, d = 5 \times 10^{-6} \text{ m}, b = 5 \times 10^{-5} \text{ m}, k = 52.3 \text{ W / m / K}, \kappa = 1.536 \times 10^{-5} \text{ m}^2 / \text{s}, \\ Q_0 = 10^{10} \text{ W / m}^2, T_0 = 300 \text{ K}$$

As for H , the depth in the z -direction, was chosen such that for all practical purposes it would mimic an infinite domain as explained in Section 4.1.1.1. Similar to the constant flux case given in that section, the computations were done for a time period of 3.0×10^{-6} seconds. As for the spatial discretizations, the following level was initially used for both the BEM and the FDM regions: Level 1 : $\Delta r = 5 \times 10^{-6}$; $\Delta z = 5 \times 10^{-7}$. For this level, the time steps used were $\Delta t = 10^{-7}$ s and 10^{-8} s. The selection of these time steps was dictated by the diffusion length scale limitation on the FDM formulation and also on their ability to capture transient characteristics as explained earlier.

Fig. 4.26 gives the temperature profiles for the different time steps. It also contains the analytical solution for the infinite domain case given in Appendix C. As for the relative errors, Fig. 4.27 gives the segment computed by the BEM while Fig. 4.28 gives the segment computed by the FDM. It is seen from the figures that in the FDM area the absolute maximum relative errors are very much close to each other for the two time steps and it is around less than 1%. On the other hand for the BEM area, the larger time step has the least error of $\sim 1\%$ and the smaller time step has an error of $\sim 4\%$. The reason for this was explained earlier in the constant flux case. As the time step is reduced, it is apparent that the error is not substantially reduced in the FDM area, which remain less than 0.5% in the region away from the matching interface. Reason for this could be adduced to the fact that the diffusion length is nearly the same order or less than the grid size for both the time steps and also the fact that the simulation was run for a small time period could be another reason. On the other hand at the BEM-FDM matching boundary a larger error is seen due to the influence of the error from the BEM side due to the

coupling effect. Therefore further reduction of the time step would not result in reducing the error where both the BEM and the FDM have the same grid discretization. The only alternative is to have different discretizations for the two regions.

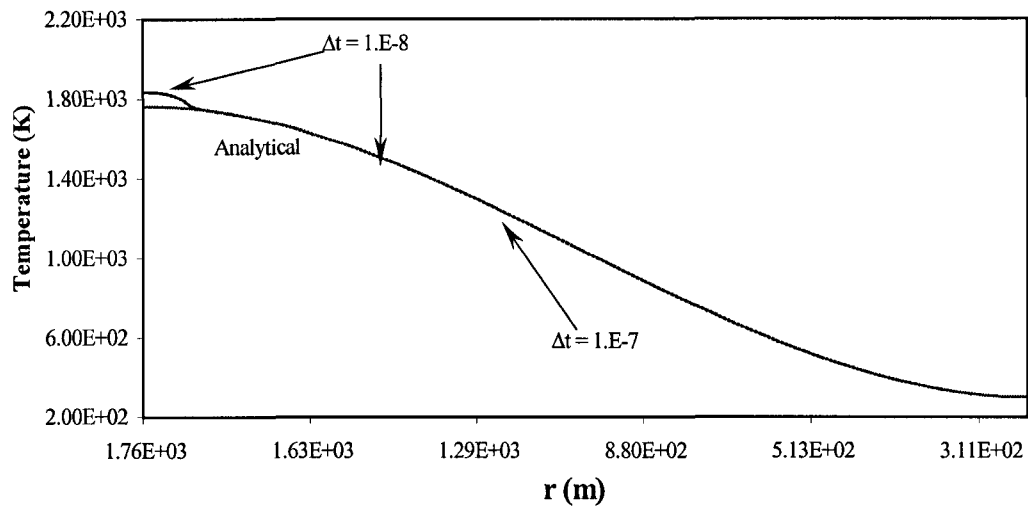


Figure 4.26 Temperature profile: variable heat flux – simulation 3 level 1

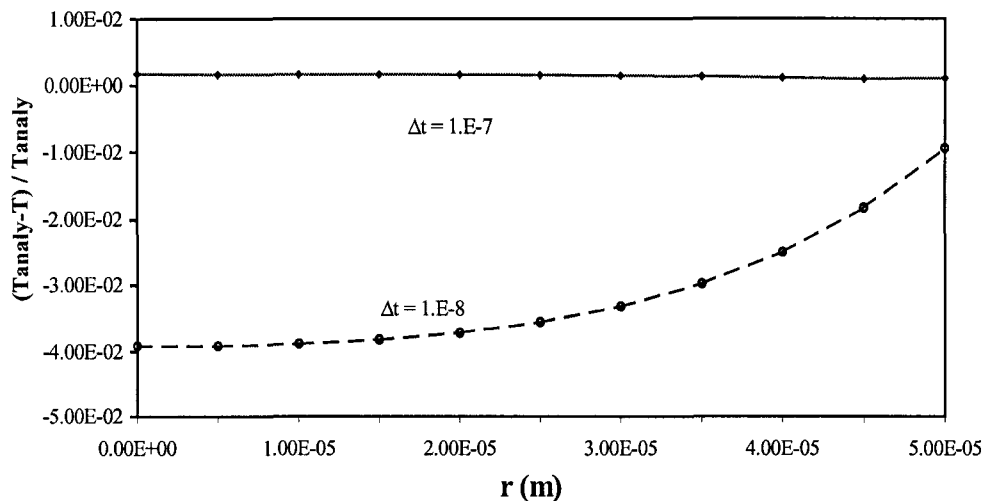


Figure 4.27 Relative error - BEM: variable heat flux – simulation 3 level 1

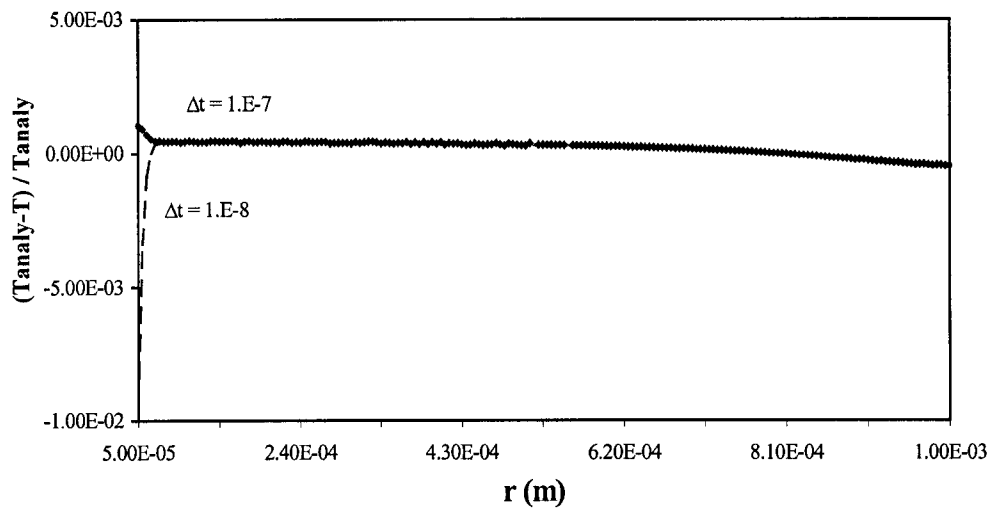


Figure 4.28 Relative error - FDM: variable heat flux – simulation 3 level 1

To further investigate this error, simulations were done where the BEM region and the FDM region utilized different grid discretization with the following refinements of the BEM region:

Level 2 : BEM - $\Delta r = 2.5 \times 10^{-6}$, $\Delta z = 2.5 \times 10^{-7}$; FDM - $\Delta r = 5 \times 10^{-6}$, $\Delta z = 5 \times 10^{-7}$,

Level 3 : BEM - $\Delta r = 1.25 \times 10^{-6}$, $\Delta z = 1.25 \times 10^{-7}$; FDM - $\Delta r = 5 \times 10^{-6}$, $\Delta z = 5 \times 10^{-7}$.

For the level 2, same time steps of $\Delta t = 10^{-7}$ s and 10^{-8} s as the level 1 were used and for the level 3 only $\Delta t = 10^{-8}$ s time step was used. Fig. 4.29 gives the error in the BEM region while Fig. 4.30 gives that of the FDM region. It is seen that the refinement of the BEM region reduced the maximum error in the $\Delta t = 10^{-8}$ s case from 4% to 1% as seen from the level 2. Further refinement as given by the level 3 reduces this error to less than 0.25% except near the BEM-FDM matching boundary. The reasons for this higher error at this boundary could be due to coupling and needs further investigation. As for the

FDM region it remains at very low level of less than 0.5% for the whole region except near the matching boundary. As for the $\Delta t = 10^{-7}$ s case the relative error remains low at less than 0.5% for both the BEM and the FDM regions.

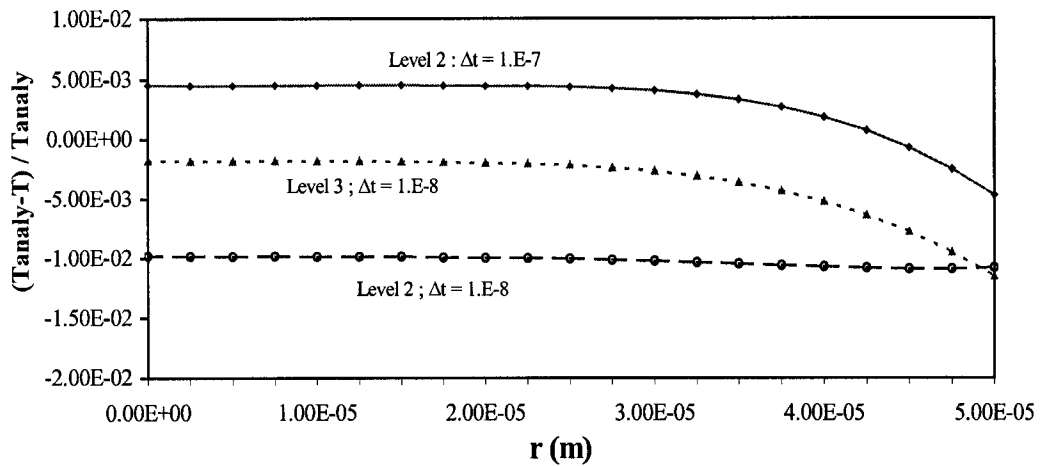


Figure 4.29 Relative error - BEM: variable heat flux – simulation 3 level 2-3

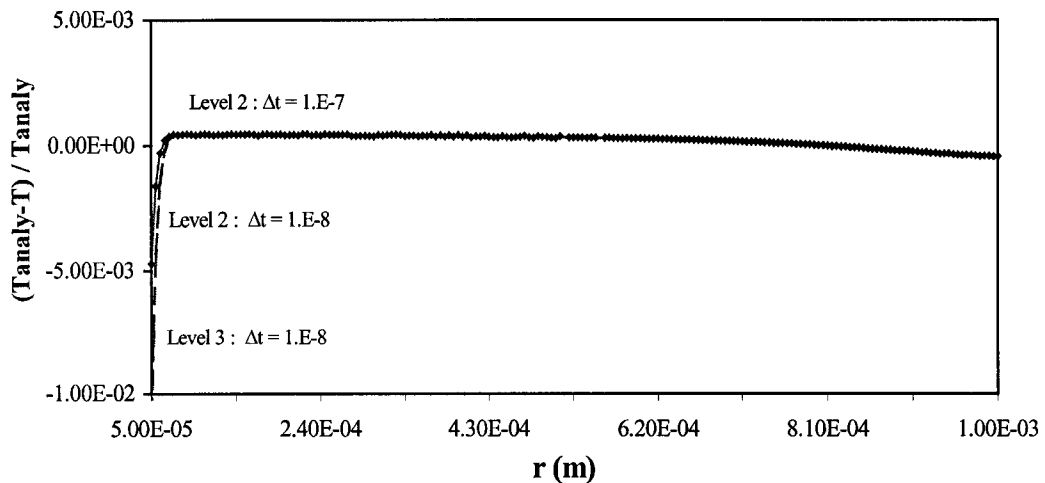


Figure 4.30 Relative error - FDM: variable heat flux – simulation 3 level 2-3

4.3 Convergence test for the conduction regime

To verify the convergence of the numerical scheme for the conduction problem, the data from the BEM-FDM coupled method was plotted with respect to discretization in a log-log plot [Atkinson (1993)]. The data from the simulations of the model for the constant flux case as given in Sec. 4.1.1 were used. The convergence was checked at three radial points along the $z = 0.0$ level, and was done for three time levels. As for comparison, similar convergence checks were computed for the simulations where only the BEM was used for the whole domain given in Fig. 4.1. Similarly, this was repeated where the FDM was used for the whole domain.

4.3.1 Convergence test for the BEM-FDM coupled model

The computations were done for $\Delta t = 0.00005s$ time step and for the three radial positions given by Figs. 4.31 - 4.33. The relative errors were computed for the spatial step sizes of 0.01m, 0.005m and 0.0025m. The plots are done for the three time levels of 0.025s, 0.5s and 1.0s. It is seen that for all the radial positions there is a slight deterioration of the order of convergence as the time level increase. The order of convergence is ~ 1.9 for the coarser spatial discretization computed from the first two points and improves to ~ 2.0 as it becomes finer which is seen from the latter two points.

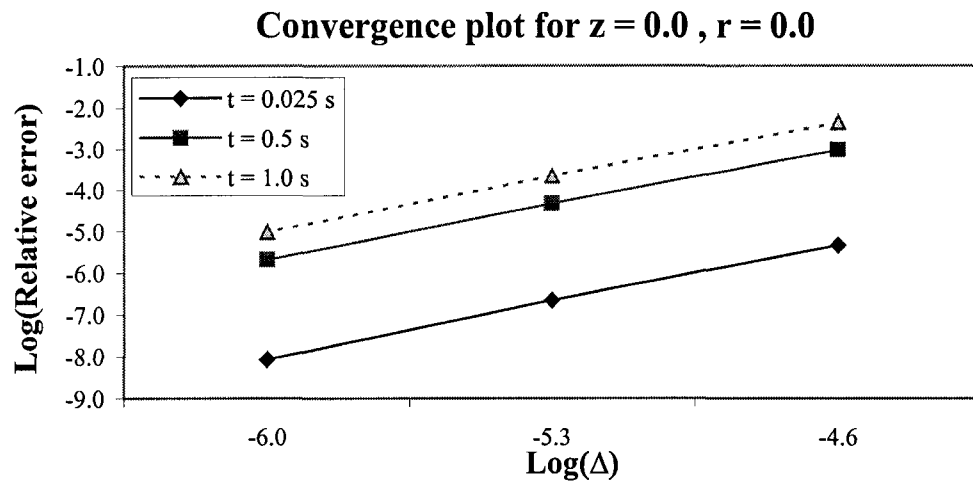


Figure 4.31 Convergence for constant flux BEM-FDM model at $r = 0.0$ m

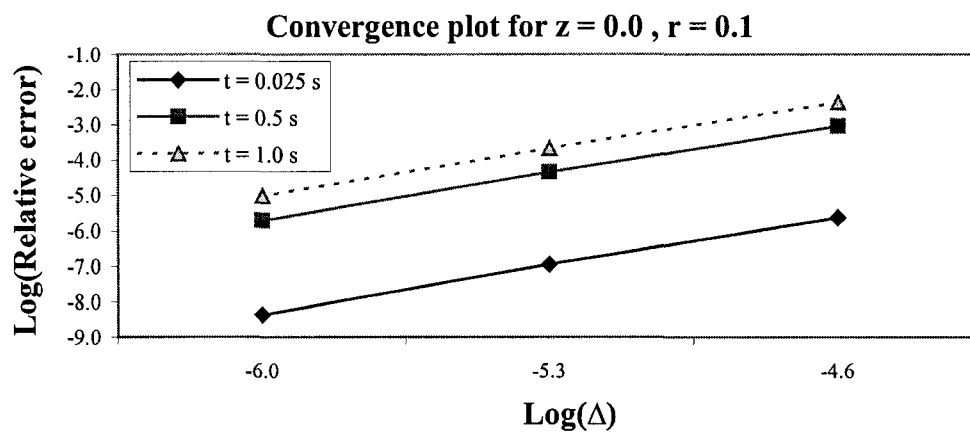


Figure 4.32 Convergence for constant flux BEM-FDM model at $r = 0.1$ m

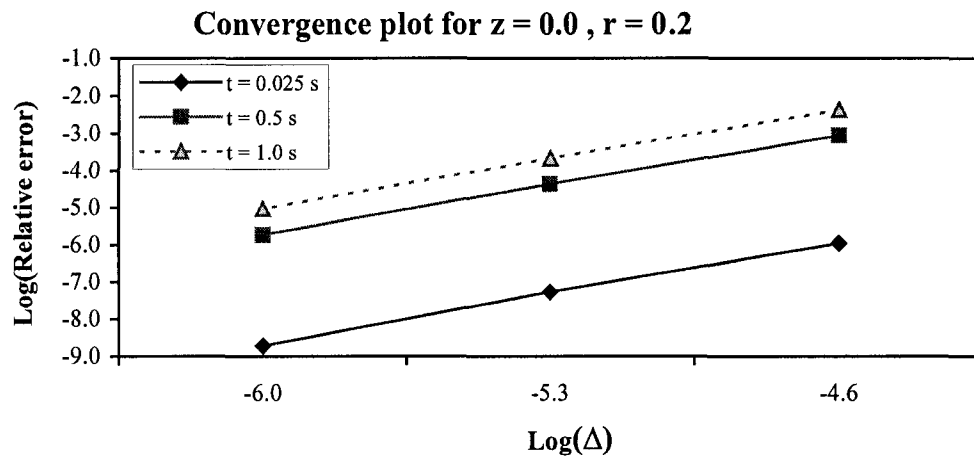


Figure 4.33 Convergence for constant flux BEM-FDM model at $r = 0.2$ m

4.3.2 Convergence test for the BEM model

The relative error was plotted similar to the earlier case. Figs. 4.34 - 4.36 give the log-log plots of relative error versus spatial step size. In this case it is seen that the order of convergence is constant with respect to discretization. This is true for all the time intervals and at all the three radial positions. Thus it is seen that the order of convergence is ~ 2.0 for the BEM method.

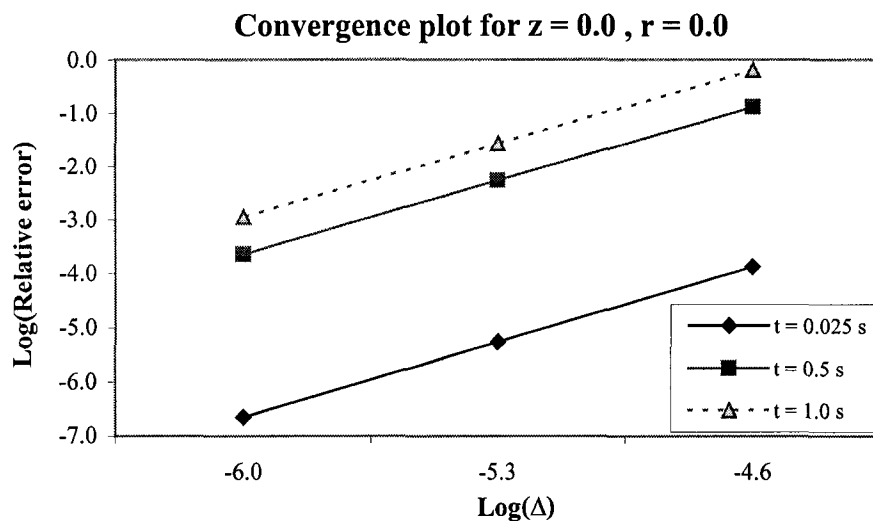


Figure 4.34 Convergence for constant flux BEM model at $r = 0.0 \text{ m}$

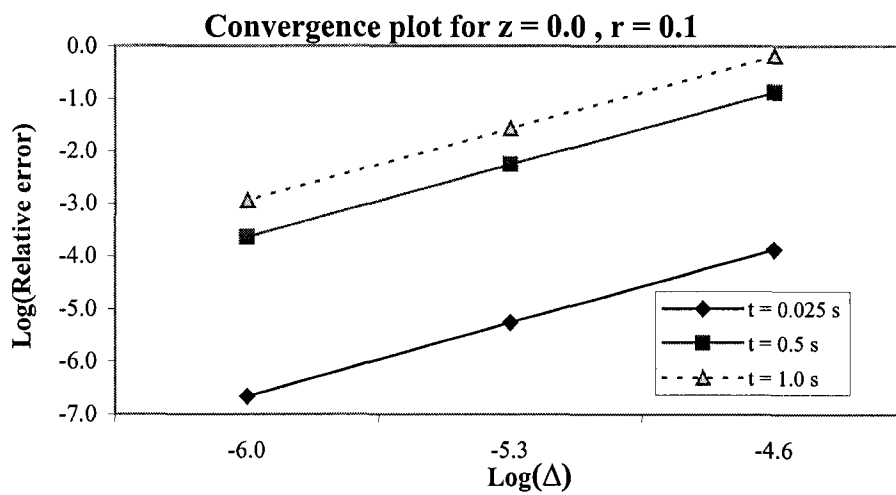


Figure 4.35 Convergence for constant flux BEM model at $r = 0.1 \text{ m}$

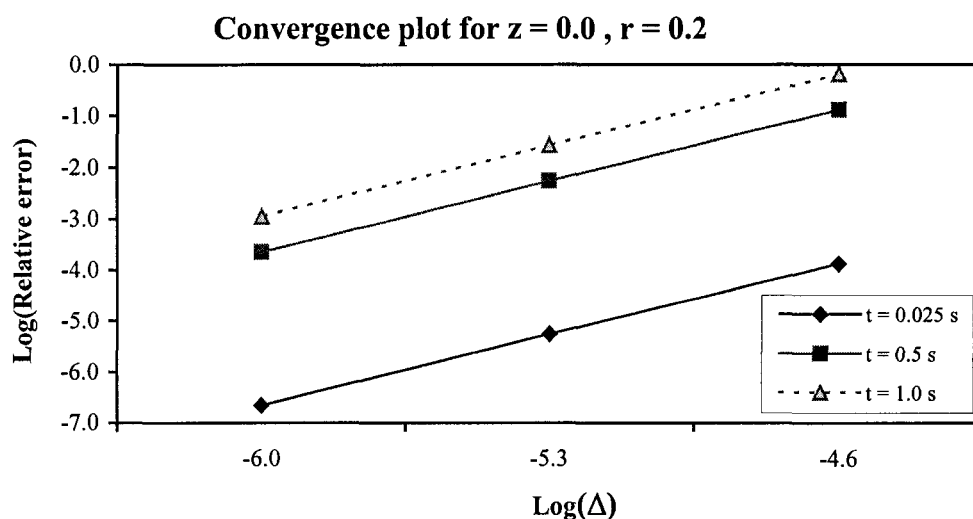


Figure 4.36 Convergence for constant flux BEM model at $r = 0.2$ m

4.3.3 Convergence test for the FDM model

In this case the order of convergence is very good for the coarser discretization with it being ~ 2.1 , and is consistent for all the radial positions and for all the time intervals. But at the finer step size of 0.0025 the order of convergence varies from ~ 1.9 to ~ 0.4 as the time interval goes from 0.025s to 1.0s as seen from Figs. 4.37 - 4.39. At this finer discretization, the step size is less than the diffusion length scale of ~ 0.00707 for the time step of $\Delta t = 1.0E-5$ s, and this allows a greater accumulation of error with the number of time steps. To investigate this further the simulations were run with a smaller time step of $\Delta t = 5E-6$ s and for the grid sizes of 0.01, 0.005, 0.0025 and 0.00125. The results are given in Fig. 4.40. For this time step the diffusion length scale is ~ 0.0022 , and it is seen that the order of convergence for all the time intervals is 2.0 to 2.3 for the

coarser grid size and for the medium refinement it is 2.0 for $t = 0.025$ and 1.6 for $t = 1.0$. For the finest refinement where the diffusion length is violated to a very high degree, it is obvious that there is no convergence, especially at the higher time intervals.

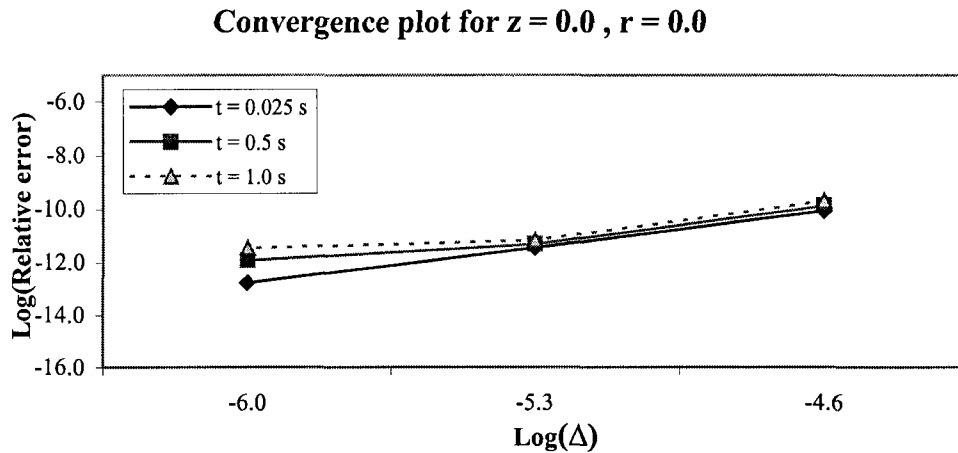


Figure 4.37 Convergence for constant flux FDM model at $r = 0.0$; $\Delta t = 5E-5$

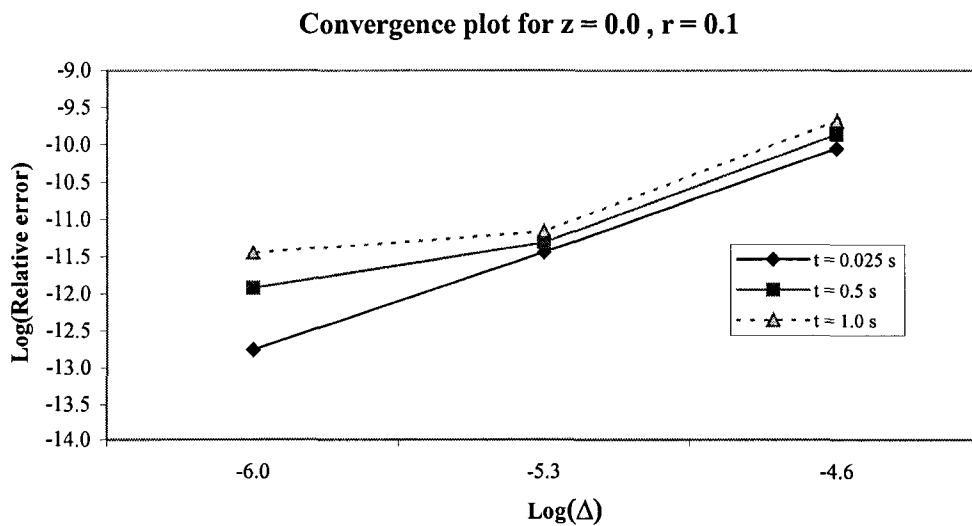


Figure 4.38 Convergence for constant flux FDM model at $r = 0.1$; $\Delta t = 5E-5$

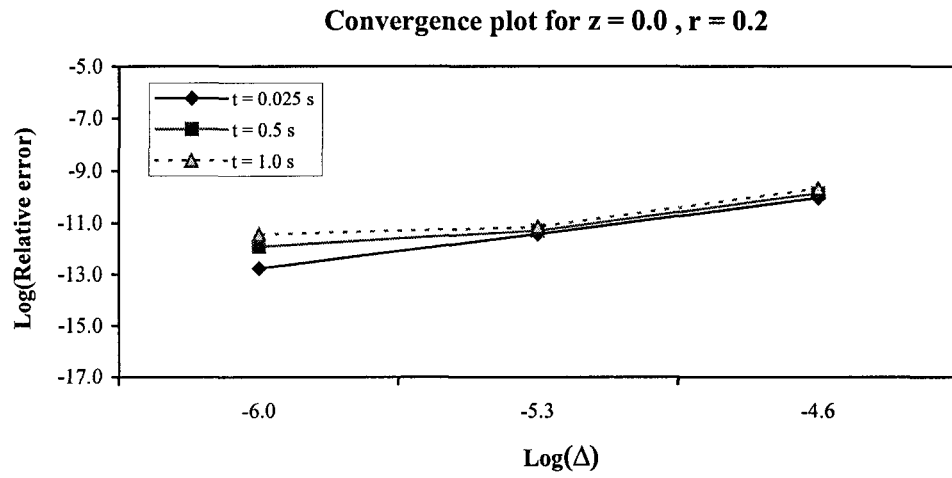


Figure 4.39 Convergence for constant flux FDM model at $r = 0.2$; $\Delta t = 5E-5$

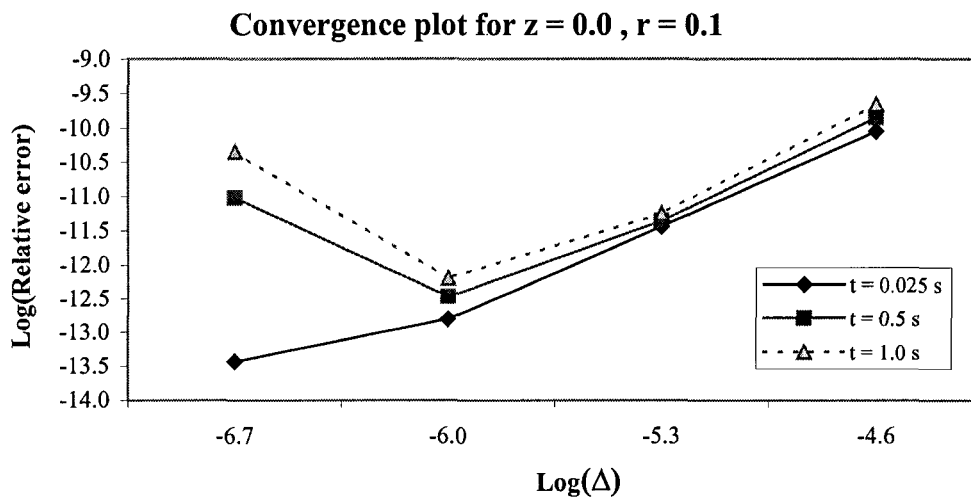


Figure 4.40 Convergence for constant flux FDM model at $r = 0.1$; $\Delta t = 5E-6$

4.4 CPU time comparison

To obtain a relative idea about the cost of using different methods for solving the conduction problem, the CPU times are tabulated below. The computing was done on a Silicon Graphics Origin 2000 machine with Irix 6.1.15F operating system. The methods used for the comparison are the FDM, BEM and the coupled BEM-FDM. The model problem used to evaluate the CPU time is the constant flux case given in Sec. 4.1.1, which is also used for the convergence test in Sec. 4.3. It is seen from Table 4.4 that the FDM method is the least expensive method and the method using BEM alone is the most expensive. This is understandable because in this method boundary and domain integrals need to be evaluated and also the number of these integrals increase geometrically with the increase of the grid points as explained in Sec. 3.1.1. This fact coupled with it being a direct method where the matrix inversion is used necessitates a large CPU time. This is seen by the consumption of the computer resources as given in the table. As for the BEM-FDM coupled model, the domain is decomposed between the two methods, thus the area solved by the BEM is less as shown in Fig. 4.1. This explains the time reduction as compared to the case where the BEM alone is used. Therefore this bolsters the argument for using the coupled model, as otherwise this time factor alone would be an immense constraint. Apart from this fact a copious amount of memory would be required to store the BEM coefficients at finer grid refinements due to the large number of elements and also the system matrix for the solution of the boundary grid points would be prohibitively large. Therefore these factors make it very impractical for the usage of the BEM for the whole domain.

Discretization Δr (m), Δz (m)	FDM method CPU time (min)	BEM method CPU time (min)	BEM-FDM method CPU time (min)
0.01	0.6	23.1	5.7
0.005	4.9	689.4	34.4
0.0025	59.6	7740.9	414.2

Table 4.4 CPU time comparison for different methods

4.5 Moving boundary simulation

To check on the moving part of the code, a constant flux Q_0 was applied on the melting zone perpendicular to the curved melting interface as shown in Fig. 4.41. The object is kept at the constant melting temperature. The analytical solution for the normal velocity of the moving part of the boundary is given by the Stefan's boundary condition,

$$u_n = -Q_0 / H_0 \rho .$$

Initial condition: $T(r, z, 0) = T_m$

Boundary conditions:

$$q_L = Q_0 \text{ for } (r, z) \in \Gamma_m$$

$$\frac{\partial T}{\partial n} = 0 \text{ rest of the boundaries}$$

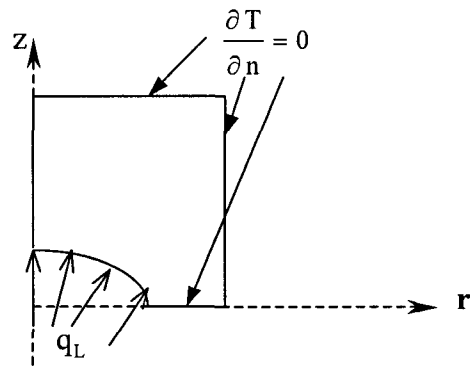


Figure 4.41 Configuration for the moving boundary

Simulations were done for: $H_0 = 1 \text{ J/kg}$, $\rho = 1 \text{ kg/m}^3$, $Q_0 = 1 \text{ W/m}^2$, with the initial

profile of the moving boundary given by an arc of a circle with the equation, $r^2 = 0.0016 - (z + 0.02)^2$. The results given below are for the different time intervals and the analytical result for $u_n = -1.0$ m/s. Tables 4.5 and 4.6 give the coordinate values of the moving boundary profile and the normal boundary velocity at discrete spatial points for the time intervals of 0.01s and 0.03s. Fig. 4.42 gives the geometric profiles at the different time intervals as indicated in the figure. It is seen that the results agree well with the analytical result even though this is somewhat of a special test case. The most error is seen at the point where the moving boundary meets the horizontal boundary. This point is treated as a moving front even though the angle, the moving boundary makes with the horizontal boundary, continuously change with the movement. This is somewhat of a compromise given the fact that there is no clear cut way to handle this point as it has no other constraining conditions in this ideal problem. The relative error varies from 4.5% at $t = 0.01$ s to 5.2% at $t = 0.05$ s for this edge point.

time = 0.01							
r	0.0000	0.0100	0.0200	0.0300	0.03947	0.0400	0.04375
z	0.0300	0.02895	0.0258	0.0200	0.0100	0.0093	0.0000
u_n	-1.0000	-1.0000	-1.0000	-1.0000	-1.0000	-1.0000	-1.0000

Table 4.5 Moving boundary simulation time = 0.01s

time = 0.03									
r	0.0000	0.0100	0.0200	0.0300	0.0362	0.0400	0.0485	0.0500	0.0633
z	0.0500	0.0493	0.0470	0.0432	0.0400	0.0376	0.0300	0.0282	0.0000
u_n	-1.0000	-1.0000	-1.0000	-1.0000	-1.0000	-1.0000	-1.0000	-1.0000	-1.0000

Table 4.7 Moving boundary simulation time = 0.03s

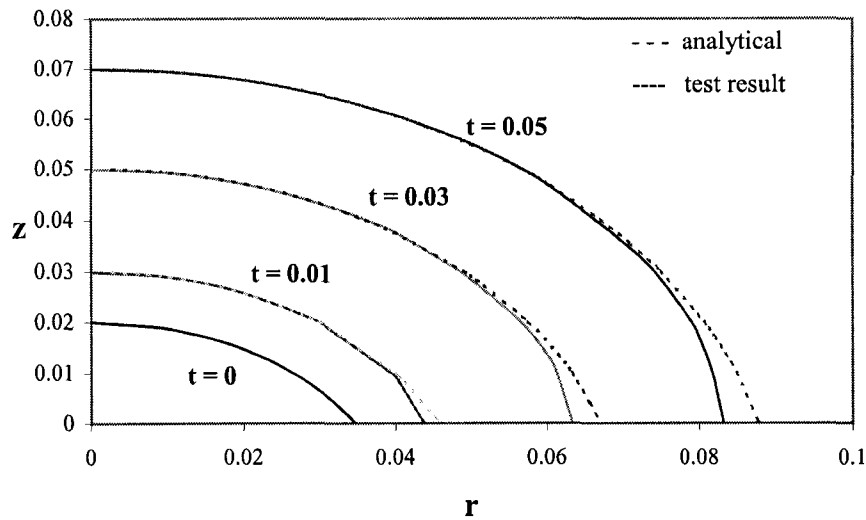


Figure 4.42 Moving boundary profiles

4.6 Thin layer simulation

In these simulations the thin layer formulation is computed as an independent model separate from the solid model. For this the curvature effects were neglected and the solid substrate was considered as a part of the semi-infinite domain where the quasi-steady state temperature distribution could be obtained analytically as given in Batteh , Chen and Mazumder [1999]. With this temperature profile, the simulations were done for the drilling of mild steel. The following physical constants for mild steel were used,

$$H_0 = 2.722 \times 10^5 \text{ J/kg}, H_1 = 6.0949 \times 10^6 \text{ J/kg}, \rho = 7879 \text{ kg/m}^3, \rho_\ell = 6405 \text{ kg/m}^3$$

$$k = 52.3 \text{ W/m/K}, k_\ell = 28.7 \text{ W/m/K}, \mu = 0.0055 \text{ N/m/s}, c = 432 \text{ J/K/kg},$$

$$c_\ell = 743 \text{ J/K/kg}, G = 148.878 \text{ J/kg/K}$$

The laser beam flux is given by $\tilde{q} = I_0 e^{-\frac{2r^2}{R_b^2}}$, which varies in a gaussian manner with respect to r . Here I_0 is the irradiance on the axis and R_b is the radius of the circular area of the laser beam. Simulations were run for the three I_0 values of 1.5×10^{10} , 3.0×10^{10} and $5.0 \times 10^{10} \text{ W/m}^2$ denoted by the laser power levels 1, 2 and 3. The R_b value was kept at 0.001 meters. The initial temperature was kept at a uniform 3300K. The initial drilling velocity and the lateral velocity of the fluid layer were kept at zero. The initial thickness was given a parabolic profile such that it increased with the radius. The simulations were run until steady state was observed. The time step of $\Delta t = 10^{-13} \text{ s}$ was used and in the immobilization transformed coordinate system, discretization was kept at $\Delta \phi = 0.01$. As the numerical scheme utilized was to a large extent an explicit method, a small time step was required for stability in the Courant-Friedrichs-Lewy (CFL) sense. The plots are done for the temperature, liquid layer thickness, lateral velocity of the fluid layer and the drilling velocity for the three different laser power levels. It is seen that the temperature comes to a steady state almost immediately thus it will have only one curve. For the rest, the results of the simulations done for the different time levels are plotted with the time levels indicated in the figure.

It is seen from the plots that there is a dependence of the laser power with the elevated values of the temperature profiles. This is an expected characteristic of laser drilling. This is also true for the drilling velocity and the melt ejecting lateral velocity. The higher power laser flux carries more energy, which manifest in these phenomena. As for the layer thickness, it is seen that it decreases with the laser intensity. This could be

explained by the fact that the higher power brings about a higher temperature at the liquid-vapor interface which brings about a higher vaporization and also a higher recoil pressure which induces a greater removal of ejecting melt by the lateral velocity.

4.6.1 Laser power level 1

The temperature profile given by Fig. 4.43 shows the expected variation with the radial distance given by the beam radius scaled distance. For this power level the evolution of the layer thickness is plotted in two parts. This is to accommodate the fact that initially the thickness increased with time and it is given in Fig. 4.44 and then after this initial stage the thickness decreased with time which is given in Fig. 4.45.

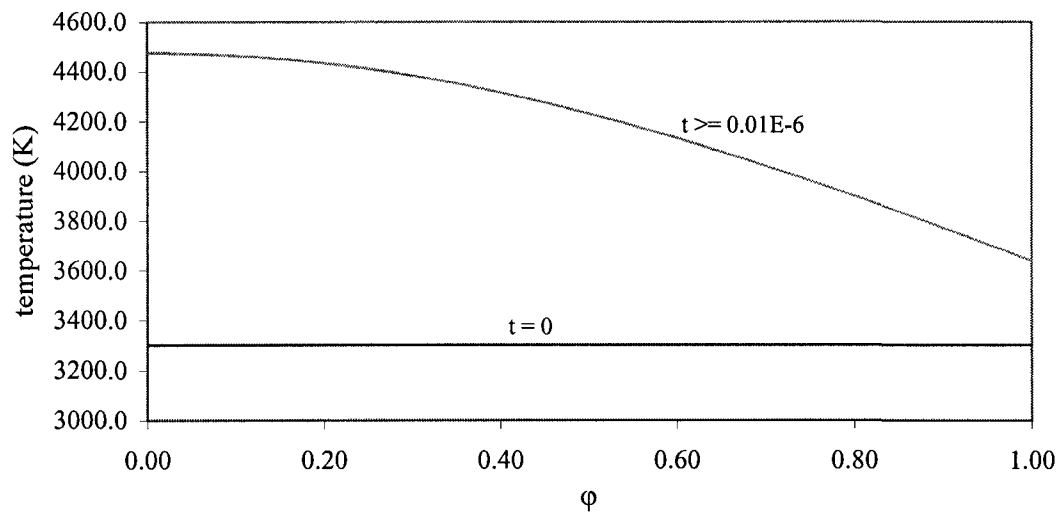


Figure 4.43 Temperature -- Laser power level 1

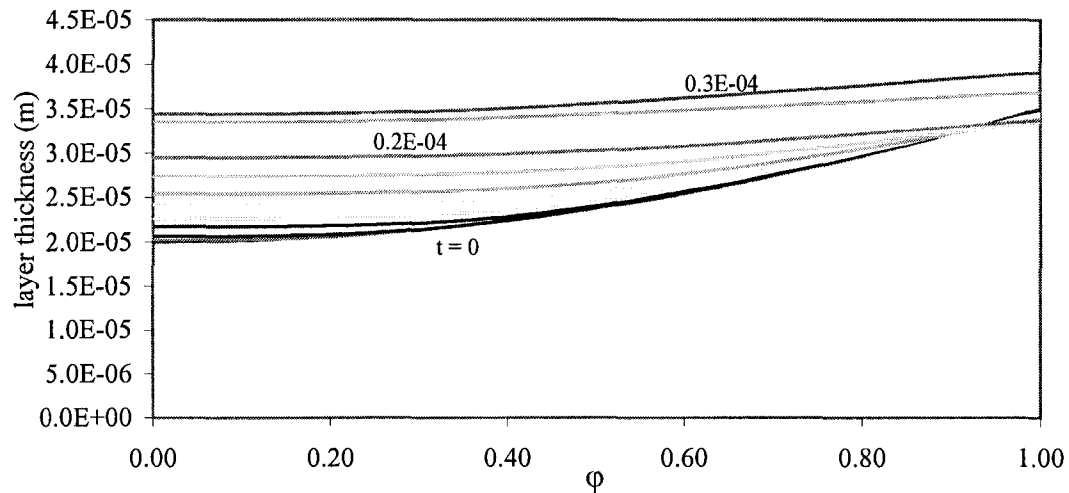


Figure 4.44 Layer thickness part 1 – Laser power level 1

This could be explained by the fact that the initial layer thickness profile, the layer temperature and the temperature in the solid substrate was such that at the center there was melting and at the edge there was solidification. This is seen in Fig. 4.44, where at the initial stage the thickness of the melt pool is increasing at the axis and decreasing at the edge of the beam. As the temperature rose on the liquid top interface, the solidification was turned into melting at the edge thus the apparent crossing of the curves. As the time advanced the lateral ejection velocity of the liquid layer is increased due to recoil pressure gradient as shown in Fig. 4.46, thus removing the melt at a faster rate. This in turn decreased the thickness of the liquid layer and increased the temperature of the liquid layer at the outer edge due to advection. This fact also increased the drilling speed with time after the initial stage is passed as shown in Fig. 4.47.

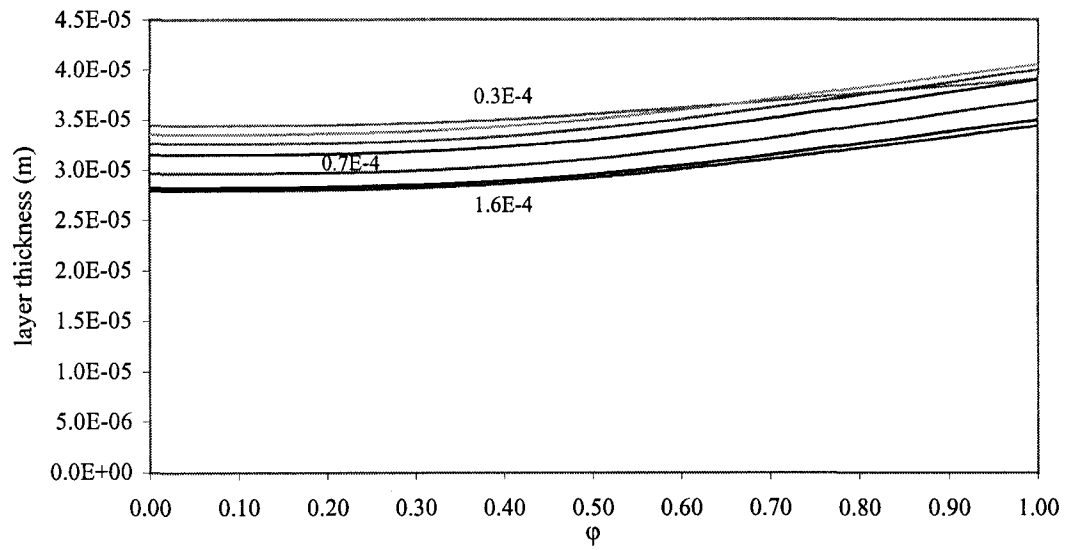


Figure 4.45 Layer thickness part 2 – Laser power level 1

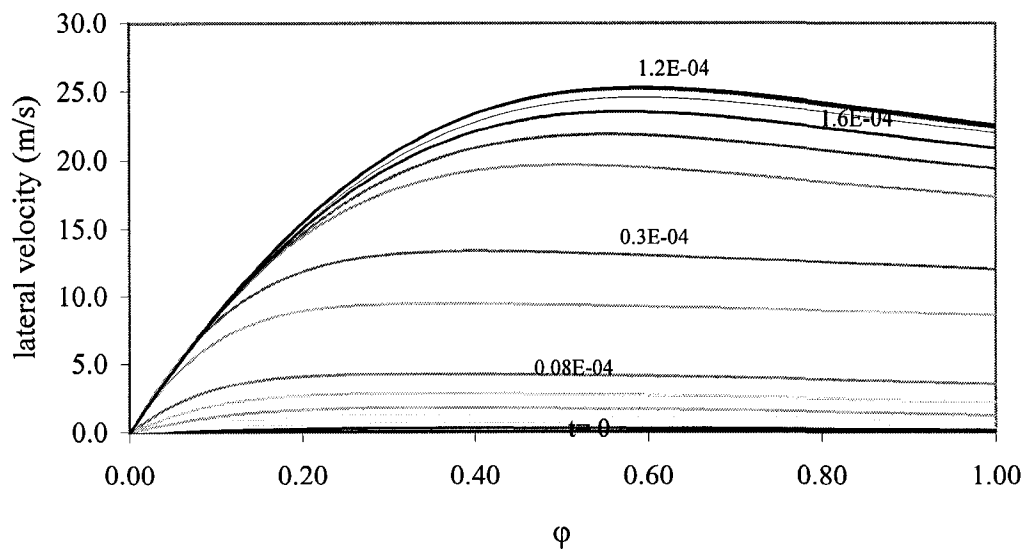


Figure 4.46 Lateral velocity – Laser power level 1

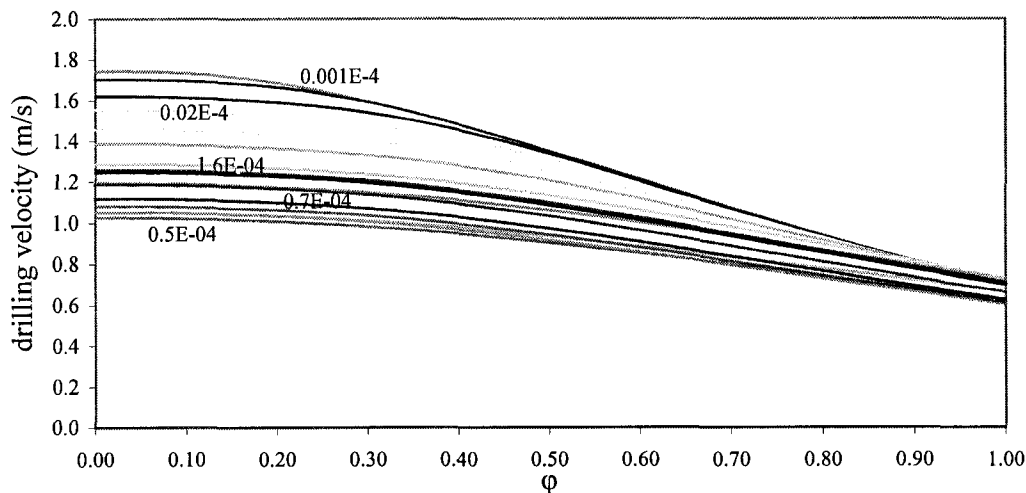


Figure 4.47 Drilling velocity – Laser power level 1

4.6.2 Laser power level 2

The temperature variation given in Fig. 4.48 is similar to the power level 1 but at a higher intensity as expected. The layer thickness shown in Fig. 4.49 has a similar crossing but is not as pronounced as the earlier case. The final melt ejection velocity and the drilling velocity given in Fig. 4.50 and Fig. 4.51 are higher as expected with the increase of the laser power. As for the thickness, it is thinner due to the higher vaporization and lateral velocity as shown in Fig. 4.49. Another salient fact is that the steady state values are reached at a shorter time period than the power level 1. This could be due to the higher lateral velocity from the higher recoil pressure, reducing the transients in an expeditious manner.

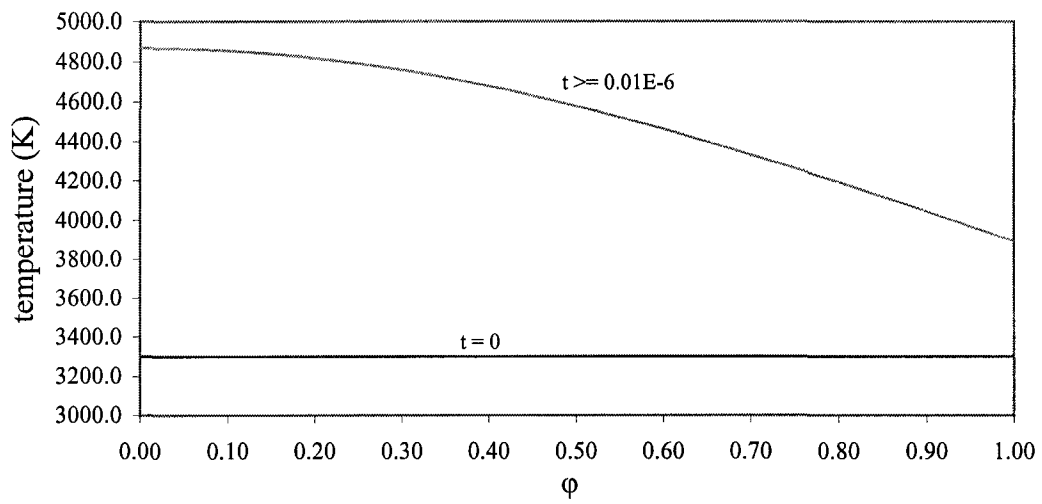


Figure 4.48 Temperature – Laser power level 2

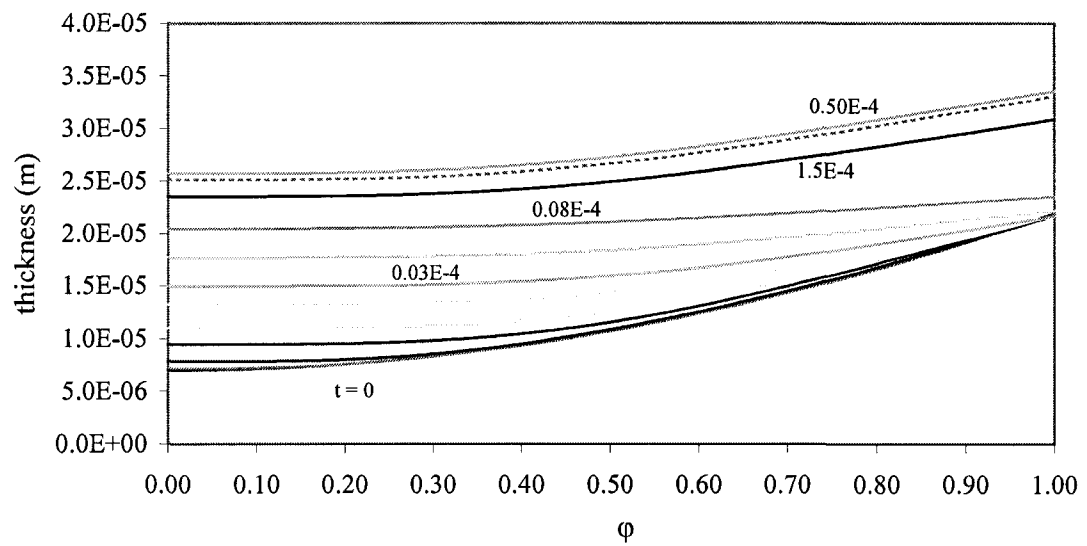


Figure 4.49 Layer thickness – Laser power level 2

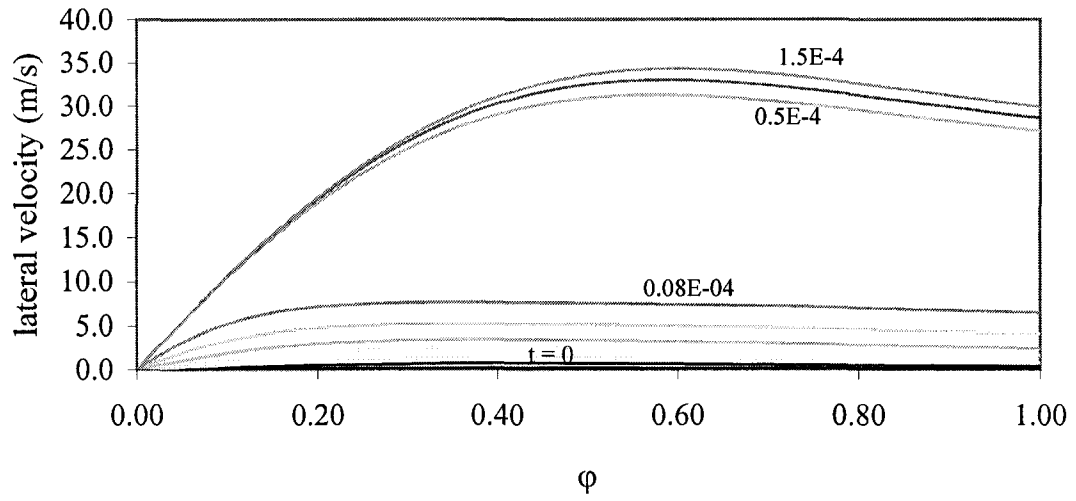


Figure 4.50 Lateral velocity – Laser power level 2

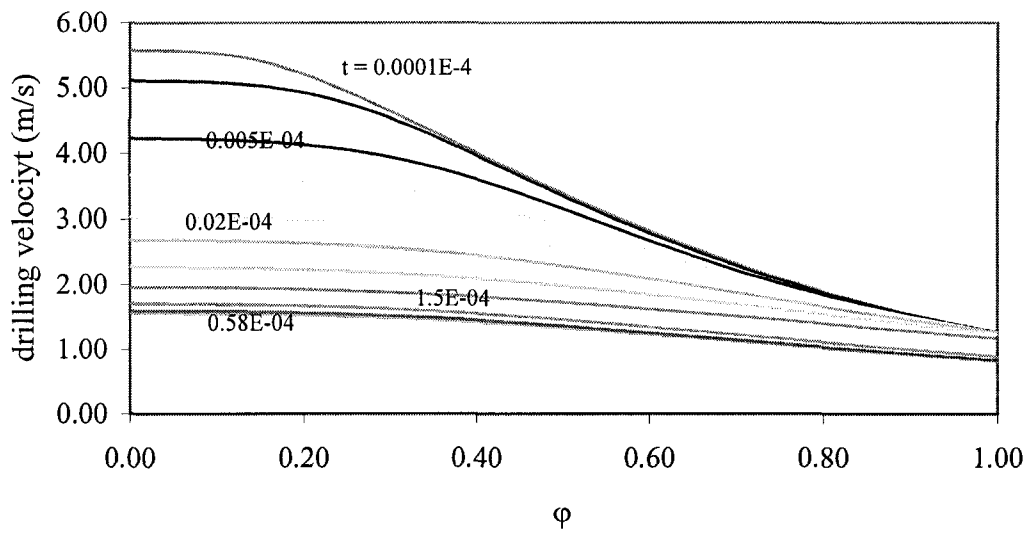


Figure 4.51 Drilling velocity – Laser power level 2

4.6.3 Laser power level 3

For this power level, the temperature profile given by Fig. 4.52 is higher than the earlier two power levels. The steady state drilling velocity and the lateral velocity are higher thus showing the higher energy from the laser is expended to give a higher removal rate of melt ejection and a higher rate of melting of the solid, which translate into a higher drilling velocity as indicated in Fig. 4.55. At steady state a thinner liquid layer is obtained as shown in Fig. 4.53. Simulations show the profiles in the figures starting at $t = 0$ s and advancing to $t = 1.0E - 3$ s in stages.

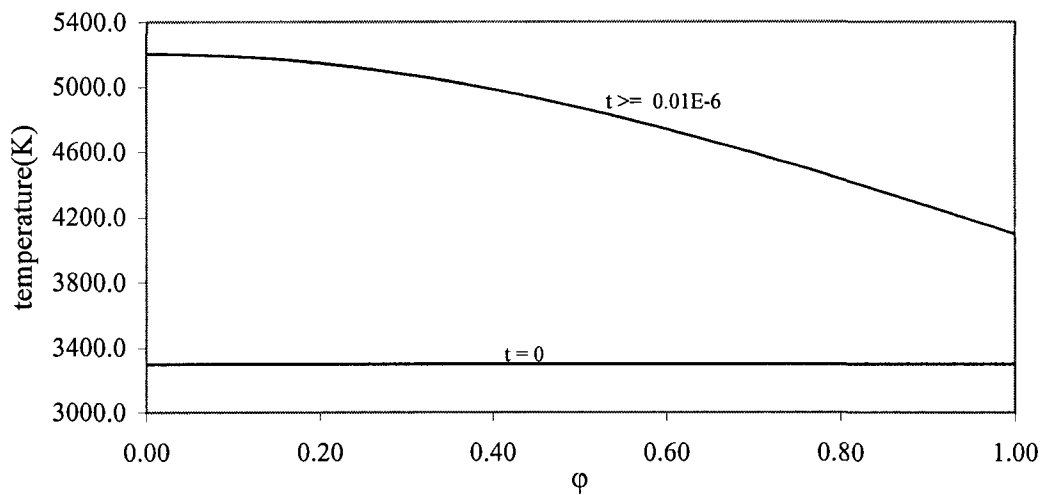


Figure 4.52 Temperature – Laser power level 3

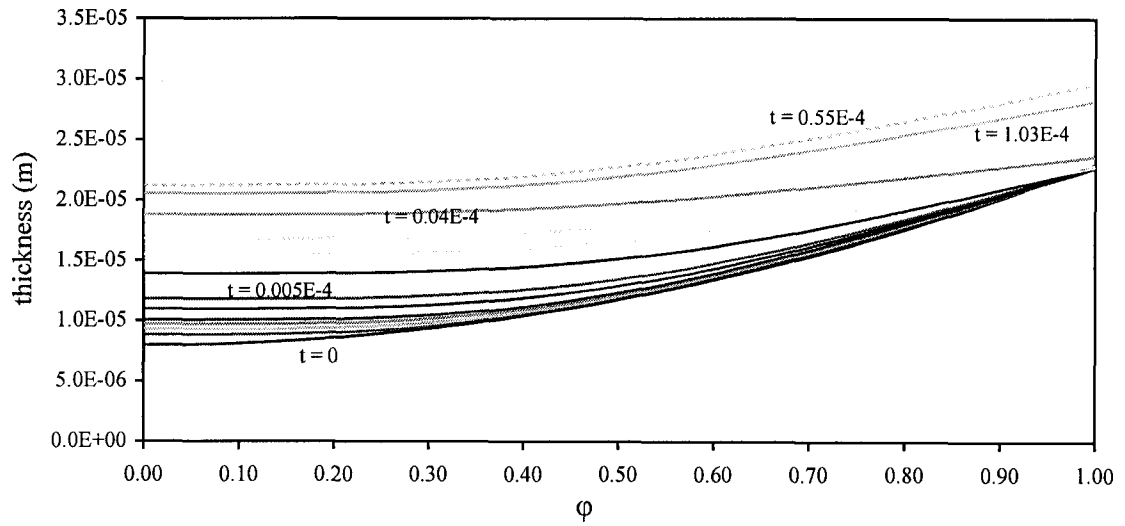


Figure 4.53 Layer thickness – Laser power level 3

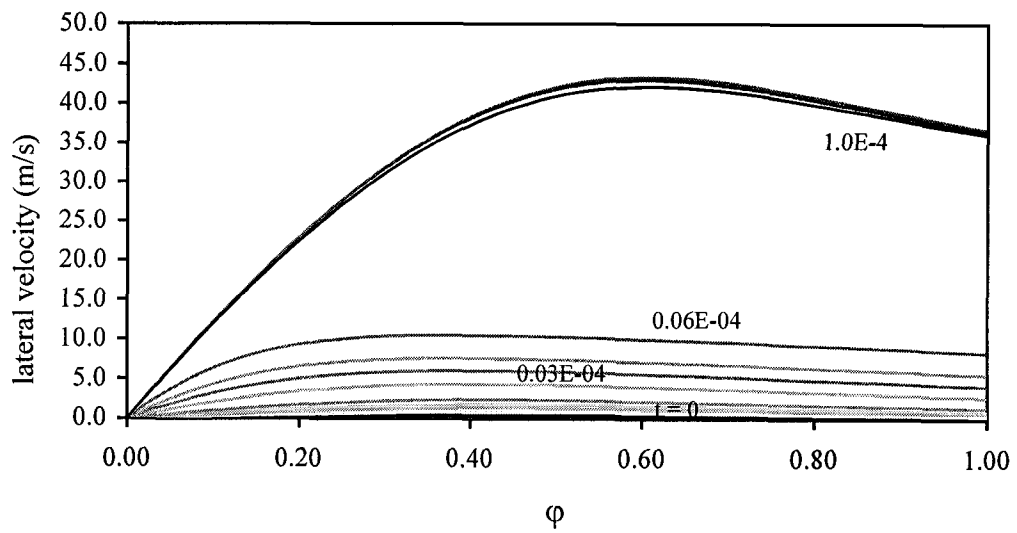


Figure 4.54 Lateral velocity – Laser power level 3

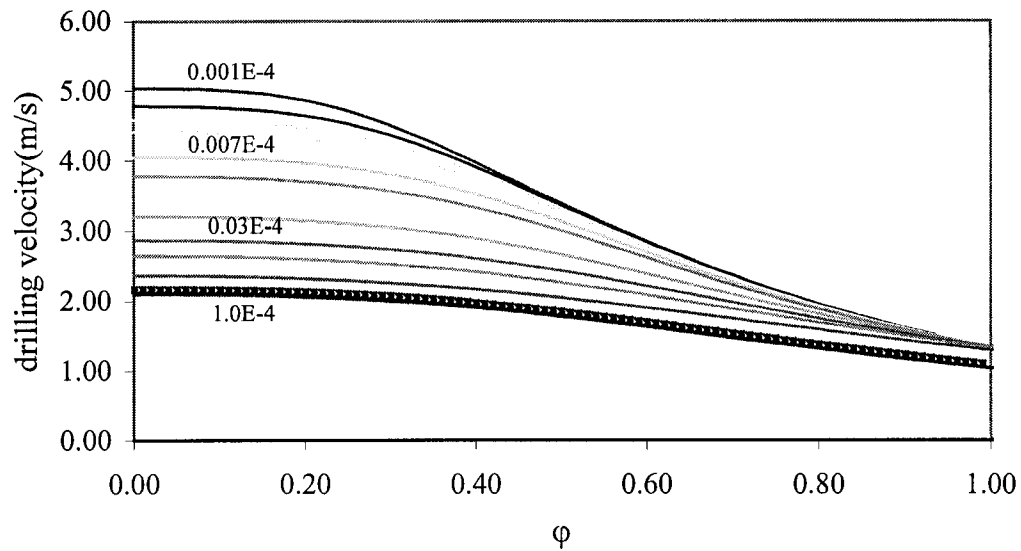


Figure 4.55 Drilling velocity – Laser power level 3

4.7 Comparison with 1-D model

The data from the above simulations were compared with the 1-D laser drilling model of Chan [1999]. The following Table 4.7 gives the results from both the models for laser drilling of mild steel. While the 2-D model was run until steady state, the 1-D model was run with a long pulse of 1.0E-3 seconds for the power cycle.

Laser Power (I_0) Gw / m ²	Temperature (K)		Thickness (μm)		Drilling velocity (m/s)	
	1 - D	2 - D	1 - D	2 - D	1 - D	2 - D
15	4306	4475	27.0	28.0	0.23	1.26
30	4702	4866	17.5	23.0	0.41	1.71
50	5010	5203	12.1	21.0	0.66	2.17

Table 4.7 Comparison of 1-D and 2-D laser drilling models

From the above table it is apparent that the prediction of the surface temperature of the molten layer by both the models are very close to each other. It is also evident that in

both of them the temperatures increase with higher laser power. As for the thickness of the layer it is seen that they are very close at low power but depart as the power is increased. The trends in the change of thickness with power in both the cases are similar. As for the drilling velocity, there is a big difference even though the trends in their changes with power are similar.

In the 1-D code, the laser power is basically averaged over the beam area as opposed to the 2-D model where the beam strength is highest at the axis and varies in a gaussian fashion. This could explain the reason for some of the differences. The other important reason is that different vaporization models were used for the laser material interaction, which would account for the differences in the temperature. Another important factor is the pressure gradient in the 2-D model simulates the melt ejection in a more realistic manner.

4.8 Convergence test for the Space-Time method

A simple test was formulated to check the convergence characteristics of the Space-Time method. For this, the simplified shallow water type equations for the axisymmetric case were derived as given in Appendix D. The simplification of the governing equations were done by neglecting the higher order and the forcing terms. Numerical values were given to the coefficients in these equations to obtain a constant coefficient coupled system of equations. The system of equations are given as follows,

$$\frac{\partial}{\partial t} \begin{bmatrix} \phi_1 \\ \phi_2 \end{bmatrix} + \frac{1}{r} \frac{\partial}{\partial r} r \begin{bmatrix} 2 & -0.75 \\ 1 & 0 \end{bmatrix} \begin{bmatrix} \phi_1 \\ \phi_2 \end{bmatrix} = 0$$

Initial conditions at $t = 0$:

$$\phi_1 = 4^5 r^3 (0.5 - r)^2 \text{ for } r \leq 0.5 \text{ and } \phi_1 = 0 \text{ for } r > 0.5$$

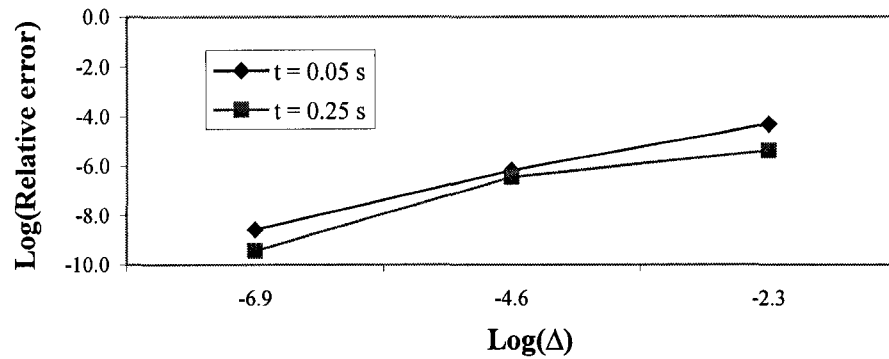
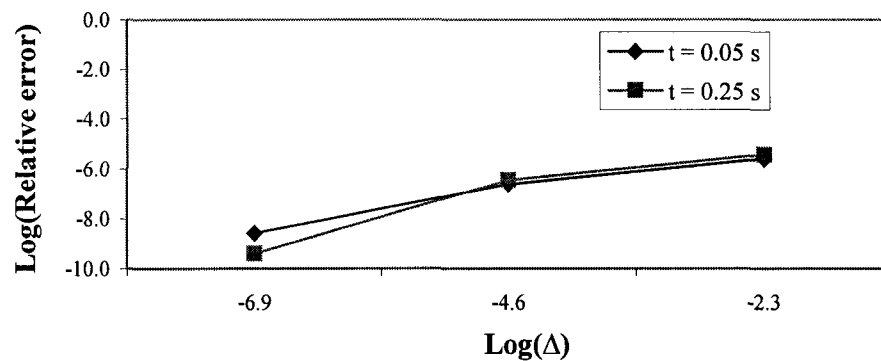
$$\phi_2 = 4^2 r (0.5 - r) \text{ for } r \leq 0.5 \text{ and } \phi_2 = 0 \text{ for } r > 0.5$$

Boundary Conditions,

$$r = 0: \phi_1 = 0; \phi_2 = 0$$

These equations were solved using the Space-Time method with the above given boundary and initial conditions. The results from the numerical simulations are compared to the analytical solutions obtained from the method of characteristics. The whole derivation and the analytical solutions are given in Appendix D.

The results are plotted for the two variables for two time intervals as given in Figs. 4.56 and 4.57. For the above given system of equations the largest eigenvalue is $\lambda_{\max} = 1.5$. Therefore from the CFL condition, the time step was set such that the $\Delta t \leq \Delta r / \lambda_{\max}$. The spatial discretization used in the computations were $\Delta r = 0.1, 0.001$ and 0.0001 and for each corresponding Δr , the respective time steps were $\Delta t = 0.05, 0.005$ and 0.0005 . The results show the order of convergence for both the variables between 0.4 to 0.8 at the coarse grid level and improving to 0.85 - 1.3 for the finer discretization. Therefore it is apparent the refinement of the grid will improve the accuracy of the results in the Space-Time method.

Convergence plot for φ_1 at $r = 0.2$ Figure 4.56 Convergence for φ_1 at $r = 0.2$ - Space-Time method**Convergence plot for φ_2 at $r = 0.2$** Figure 4.57 Convergence for φ_2 at $r = 0.2$ - Space-Time method

5.0 CONCLUSION AND FUTURE WORK

5.1 Conclusion

A coupled BEM-FDM formulation for the conduction regime in a solid that incorporated a moving interface with the melting or the solidifying problem was developed successfully in the first phase. In this part of the model the domain is subdivided into the BEM and the FDM sub-domains to exploit the strengths and capabilities of the two methods. The BEM sub-domain is solved symbolically for the boundary solution and then incorporated into the FDM equations as a flux condition thus coupling the two methods. Consequently, the modified FDM equation where the BEM part is incorporated indirectly could be solved alone. This part of the conduction regime was tested for a number of realistic test cases involving the constant heat flux boundary condition and also the boundary condition of heat flux varying with radius. The model was also tested using very high heat flux conditions, both constant and radially varying, thus approaching levels of intensity encountered in laser drilling. The results were compared with analytical solutions and were found to give a very satisfactory performance. It also enumerated many important factors that need to be addressed in future work. Especially the fact, that the BEM being an integral method does not have a limit on the grid refinement, and on the other hand the FDM with this limitation that depends on the time step, creates some interesting challenges for the future work. This will require some effort to increase the accuracy without increasing the cost of computing.

As for the moving boundary interface, the temperature along the BEM-FDM interface which comes from the FDM part and with the conjunction of heat flux from the solid-liquid interface, were used to calculate the normal boundary velocity of the solid-liquid interface. This part of the formulation was tested by a simple case of a melting interface which was given an initial profile of a circular arc and also where the whole domain was initially kept at the melting temperature. The time evolution of the moving boundary profile and the normal boundary velocity were found to be acceptable even though this test case is somewhat ideal.

In the next phase of the development a thin layer model was developed to simulate the behavior of the molten metal liquid layer when it is subjected to a laser flux and also its interaction with the solid substrate. Towards this endeavor, a transient set of equations for the thin layer model was developed from the free surface, mass, momentum and the energy equations in body fitted axisymmetric coordinate system. The governing equations were simplified by neglecting small order terms due to the curvature of the boundary and also by comparing the significance of each term, evaluated using typical scale values for laser drilling. These transient equations were then further simplified by using integral techniques where characteristic profiles for the temperature and the velocity were assumed and then integrated in the thickness direction. Combined with the constitutive equations that govern the laser interaction with material, these transient hyperbolic equations for the thickness, velocity and the temperature were solved using the Space-Time method of Solution Element and Conservation Element. This part of the model was tested using different laser power levels that are typically used in laser

drilling. The evolution of the liquid-vapor interface temperature, layer thickness, drilling velocity and the lateral velocity show the expected characteristic for laser drilling from similar work done by others and also from the 1-D model. The prediction of lateral velocity is higher than the 1-D model, but this is to be expected as the 2-D model incorporates the radial variation of the laser beam intensity and thus able to model the driving pressure gradient in a more realistic manner. This model is a fully transient model as opposed to quasi-steady state models that are seen in the literature. As opposed to simpler models, this one incorporates more realistic physics with respect to the interaction of the laser with the liquid layer given by the Langmuir theory. As for the computational work from this model, due to the requirement of a very small time step, raises some important practical questions that has to be faced in the future when this is coupled with the BEM-FDM model.

It is seen that the adaptation of the Space-Time method to an axisymmetric problem with this method's ability to solve transient hyperbolic systems and its simplicity in implementation, is a very effective extension of this method. It has been successfully demonstrated of having the necessary robustness and stability to be used in such complex governing equations found in the modeling of the liquid layer created in laser drilling with its strong hyperbolic nature. The convergence characteristics of the method were also found to be satisfactory when checked for the test case.

Finally the TLM is coupled to the solid side by the interface velocity, Stefan's boundary condition, interface melting temperature and the mass conservation. As the TLM is solved by the Space-Time method that also incorporates an immobilization

transformation, the nodal values from this method and the BEM at their common interface are matched by linear interpolation. This combined BEM-FDM-TLM model is implicit in nature therefore an iteration scheme has to be employed to solve for the solution at the next time step. The combined model incorporates all aspects of laser drilling. It models the material interaction with the laser at the top surface that culminates in vaporization and melt ejection. It also models the solid-liquid interface movement and the heat lost in the substrate, thus accounting for all the energy input. The model is a complex one that attempts to model a very complex phenomenon using many analytical and numerical techniques. Due to its complexity, it needs a large computer memory and processing time. This turns out to be its Achilles heel. Even though many simplifications were incorporated in the derivation phase of the model, it still turned out to be a very formidable task in formulating the model, numerical implementation and coding. It also raises many practical questions in running the code and verification of the results that needs to be addressed in the future.

5.2 Future work

As part of the future work many important factors that arose in this work need to be investigated to improve the accuracy and efficiency. One of the main points is the coupling of the BEM and the FDM and the discretisation limit that was encountered. One way to overcome this is to have different levels of discretisation for the two regions where the two methods are implemented. This was demonstrated in a limited fashion and needs to be studied further. The other important point to investigate is the high error that

is encountered in the BEM when the time step is reduced for a fixed spatial grid size. It needs to be investigated if linear interpolation functions especially near the heat flux boundary should be replaced by a higher order one that would be able to capture the steep variations of temperature more accurately.

As for the combined BEM-FDM-TLM model, it needs to be verified with practical results. It also raises some very pertinent questions with regard to the time step selection. As the TLM part of the code needs extremely small time steps, it makes sense to investigate the possibility of increasing it by going to a more implicit formulation for the Space-Time method. The other strategy is to run the two methods at two different time steps with the BEM-FDM model time step being an integer multiple of the TLM time step. But this creates a somewhat of a challenging task to couple the two.

As for the general improvement of the model, it needs to incorporate the radiation loss of heat from the laser incident surface and also the absorptivity parameter for the laser irradiation. The other modification that needs to be thought about is the extension of it to deep holes where the curvature effects are more pronounced and also where the effects of multiple reflections of the laser beam from the walls of the hole can not be neglected.

APPENDIX A

A1 Integral representation of the coefficients in the BEM equation

The BEM equations are discretized using linear elements for the solid boundary and cubic elements for the moving elements. For time, linear interpolation functions are used.

First Eqn. (3.2), admits a Green's function, as given in Beck (1992), of the form,

$$G(r, z, t; r_i, z_i, \tau) = \frac{-1}{8[\pi\kappa(\tau-t)]^{3/2}} \exp\left[-\frac{(r-r_i)^2 + (z-z_i)^2}{4\kappa(\tau-t)}\right] \exp\left[-\frac{r r_i}{2\kappa(\tau-t)}\right] I_0\left[\frac{r r_i}{2\kappa(\tau-t)}\right]$$

Its normal derivative is given by,

$$\left(-\frac{\partial G}{\partial n}\right) = \frac{G}{2\kappa(\tau-t)} \left[(r-r_i)n_r + (z-z_i)n_z + n_r r_i \left(1 - \frac{I_1\left(\frac{r r_i}{2\kappa(\tau-t)}\right)}{I_0\left(\frac{r r_i}{2\kappa(\tau-t)}\right)} \right) \right]$$

Here I_0 and I_1 are the modified Bessel functions of the 0th and 1st order respectively.

A1.1 Types of Integrals

As for the moving boundary, for a given time step, each node of interest is advanced in a number of sub-intervals. At each sub-interval the position is computed and a cubic spline is fitted. Thus the boundary integrals have to be done along this curved path. Let $S(r)$ gives the spline function, where the radial co-ordinate is the independent variable. The interpolation functions of time and space for the 'j'th element as denoted by Fig. A.1, are given by,

$$\text{Time : } \phi^1 = \frac{\tau - t}{\tau} \quad ; \quad \phi^2 = \frac{t}{\tau}$$

$$\text{Space : } \phi^1 = \frac{L_j - \ell(r)}{L_j} ; \phi^2 = \frac{\ell(r)}{L_j}$$

$$\text{where } L_j = \int_{r_j(t)}^{r_{j+1}(t)} \sqrt{1 + S'(r)^2} \, dr ; \quad \ell = \int_{r_j(t)}^{r(t)} \sqrt{1 + S'(r)^2} \, dr$$

For the moving interface we see the following integrals. For the source point at 'i', the integral for the 'j' th element would be given as follows.

$$P_{j,i}^{mn} = \int_0^\tau \phi^m \int_{r_j(t)}^{r_{j+1}(t)} \phi^n G 2\pi r \sqrt{1 + S'(r)^2} \, dr \, dt$$

$$Q_{j,i}^{mn} = \int_0^\tau \phi^m \int_{r_j(t)}^{r_{j+1}(t)} \phi^n \left(-\frac{\partial G}{\partial n} \right) 2\pi r \sqrt{1 + S'(r)^2} \, dr \, dt \quad m=1,2 ; n=1,2$$

For the solid boundary the 'j th' straight-line element is mapped to $[-1,1]$, thus r and z could be expressed in the new co-ordinates $\xi \in [-1,1]$. Then the spatial interpolation functions are,

$$\phi^1 = \frac{L_j - \ell}{L_j} = \frac{1 - \xi}{2} ; \phi^2 = \frac{\ell}{L_j} = \frac{1 + \xi}{2}$$

$$r = \frac{1}{2} \{ (1 - \xi)r_j + (1 + \xi)r_{j+1} \} ; \quad z = \frac{1}{2} \{ (1 - \xi)z_j + (1 + \xi)z_{j+1} \} ;$$

$$L_j = \sqrt{(r_{j+1} - r_j)^2 + (z_{j+1} - z_j)^2} \quad ; \quad \ell = \sqrt{(r - r_j)^2 + (z - z_j)^2}$$

Similarly the integrals are given by,

$$H_{j,i}^{mn} = \kappa \int_0^\tau \phi^m \int_0^{L_j} \varphi^n \left(-\frac{\partial G}{\partial n} \right) 2\pi r \, d\ell \, dt = \kappa \frac{L_j}{2} \int_0^\tau \phi^m \int_{-1}^1 \varphi^n \left(-\frac{\partial G}{\partial n} \right) 2\pi r \, d\xi \, dt$$

$$G_{j,i}^{mn} = \kappa \int_0^\tau \phi^m \int_0^{L_j} \varphi^n G \, 2\pi r \, d\ell \, dt = \kappa \frac{L_j}{2} \int_0^\tau \phi^m \int_{-1}^1 \varphi^n G \, 2\pi r \, d\xi \, dt$$

The domain integrals are evaluated by integrating over quadrilateral and triangular elements. The triangular elements are found adjacent to the moving boundary and the rest are quadrilateral elements. The shape functions correspond to the nodes of the element and J is the Jacobian from mapping of the domain element to the computational element $[-1,1] \times [-1,1]$ for the quadrilateral elements and as for triangular elements it would be the vertices of the triangle: $(-1,-1)$, $(1,-1)$ and $(-1,1)$. The Green's function kernel in the integrand for very small time step would take the characteristics of a delta function thus making the integration not that accurate. To overcome this it was regularized by using the polar coordinate form for the 2-D integration (Brebia [1984], Brebia et al [1989]). For the 'k'th element the general form of the integral will be as follows, where the number of nodal points for each element will be 3 or 4 depending on the triangular or the quadrilateral element respectively.

$$\text{For the triangular element: } {}^n \mathfrak{S}_{i,k}^1 = \int_{-1}^1 \int_{-1}^{1-\eta} J \varphi^n G(r, z, 0; r_i, z_i, \tau) 2\pi r \, d\xi \, d\eta \quad n = 1, 3$$

$$\text{For the quadrilateral element: } {}^n \mathfrak{Q}_{i,k}^1 = J \int_{-1}^1 \int_{-1}^1 \varphi^n G(r, z, 0; r_i, z_i, \tau) 2\pi r \, d\xi \, d\eta \quad n = 1, 4$$

Using the above integrals, coefficients of the BEM system of equations could be formed. For the boundary integrals the contribution to a node comes from the two elements that have it in common. As for the domain integral, it is summed over its elements which

correspond to their respective nodal coefficients been multiplied by their nodal initial temperature. Let the number of triangular and quadrilateral elements be ‘KT’ and ‘KQ’ respectively. Here the superscript ‘m’ stands for the time and it is 1 for the initial time and 2 for the present time.

The coefficients are given by,

$$A_{j,i}^m = H_{j-1,i}^{m2} + H_{j,i}^{m1} \quad ; \quad B_{j,i}^m = G_{j-1,i}^{m2} + G_{j,i}^{m1}$$

$$E_{j,i}^m = \left(\frac{\kappa L \rho}{k} + T_m \right) (P_{j-1,i}^{m2} + P_{j,i}^{m1}) \quad ; \quad F_{j,i}^m = \kappa (Q_{j-1,i}^{m2} + Q_{j,i}^{m1}) \quad ; \quad C_{j,i}^m = \frac{\kappa}{k} (P_{j-1,i}^{m2} + P_{j,i}^{m1})$$

$$D_i^1 = \sum_{k=1}^{KT} \sum_{n=1}^3 {}^n \mathfrak{S}_{i,k}^1 \quad {}^n T_k^1 + \sum_{k=1}^{KQ} \sum_{n=1}^4 {}^n \mathfrak{Q}_{i,k}^1 \quad {}^n T_k^1$$

The detailed description of computing the boundary element integrals that are singular and near singular will be given in the coming subsections.

A2 Computational details of the coefficients

The details of matrix coefficients coming out of the boundary integrals are given below. Each boundary integral contributes two coefficients with respect to the two nodes of the element. The following quantities are defined with respect to the following figure.

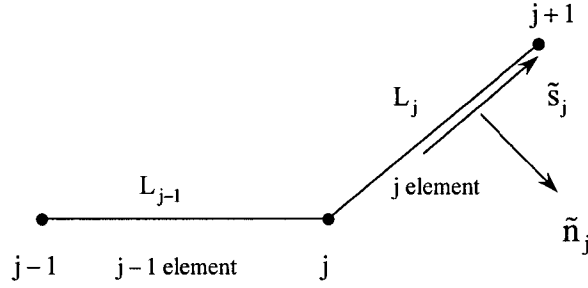


Figure A.1 Nodes and elements for the computation of BEM coefficients

For the 'j' th element, the normal and tangent vectors are defined as follows, where \tilde{i}_r and \tilde{i}_z are unit vectors in r and z coordinate directions respectively.

$$\tilde{n}_j = n_{jr}\tilde{i}_r + n_{jz}\tilde{i}_z ; \quad \tilde{s}_j = s_{jr}\tilde{i}_r + s_{jz}\tilde{i}_z$$

$$n_{jr} = \frac{z_{j+1} - z_j}{L_j} ; \quad n_{jz} = -\frac{r_{j+1} - r_j}{L_j} ; \quad s_{jr} = -n_{jz} ; \quad s_{jz} = n_{jr}$$

And, for any source point 'i' and for field point (r,z) define,

$$\tilde{d} = (r - r_i)\tilde{i}_r + (z - z_i)\tilde{i}_z ; \quad d = \sqrt{(r - r_i)^2 + (z - z_i)^2}$$

A2.1 Boundary elements on the symmetric axis ($r = 0$)

For source point $i \neq$ corner point where the axis meets either of the two boundaries, and for the 'j' th element,

$$G_{j,i}^{mn} = 0 ; H_{j,i}^{ln} = 0 ; H_{j,i}^{21} = \frac{1}{2}\delta(i, j) ; H_{j,i}^{22} = 0$$

$$G_{j-1,i}^{mn} = 0 ; H_{j-1,i}^{ln} = 0 ; H_{j-1,i}^{21} = 0 ; H_{j-1,i}^{22} = \frac{1}{2}\delta(i, j)$$

For $i =$ corner point where the axis intersects either the top or the bottom boundary,

$$G_{j,i}^{mn} = 0; \quad H_{j,i}^{ln} = 0; \quad H_{j,i}^{21} = \left(\frac{\text{interior } \angle_i}{2\pi} \right) \delta(i, j); \quad H_{j,i}^{22} = 0$$

$$G_{j-1,i}^{mn} = 0; \quad H_{j-1,i}^{ln} = 0; \quad H_{j-1,i}^{21} = 0; \quad H_{j-1,i}^{22} = \left(\frac{\text{interior } \angle_i}{2\pi} \right) \delta(i, j)$$

A2.2 Source point 'i' on the symmetric axis ($r_i = 0$)

For this case the Green function simplify as follows,

$$G = -\frac{1}{8[\pi\kappa(\tau-t)]^{3/2}} \exp\left[-\frac{r^2 + (z-z_i)^2}{4\kappa(\tau-t)}\right]; \quad \left(-\frac{\partial G}{\partial n}\right) = \frac{G}{2\kappa(\tau-t)}[\tilde{\mathbf{d}} \cdot \tilde{\mathbf{n}}]$$

The following integrals are evaluated analytically.

$$\int_0^\tau \frac{1}{(\tau-t)^{3/2}} \exp\left[-\frac{d^2}{4\kappa(4\tau-t)}\right] dt = \frac{2\sqrt{\kappa}}{d} \Gamma\left(\frac{1}{2}, \frac{d^2}{4\kappa\tau}\right)$$

$$\int_0^\tau \left(\frac{\tau-t}{\tau}\right) \frac{1}{(\tau-t)^{3/2}} \exp\left[-\frac{d^2}{4\kappa(4\tau-t)}\right] dt = \frac{1}{\sqrt{\tau}} \left(\frac{d}{2\sqrt{\kappa\tau}}\right) \Gamma\left(-\frac{1}{2}, \frac{d^2}{4\kappa\tau}\right)$$

$$\int_0^\tau \frac{1}{(\tau-t)^{5/2}} \exp\left[-\frac{d^2}{4\kappa(4\tau-t)}\right] dt = \left(\frac{2\sqrt{\kappa}}{d}\right)^3 \Gamma\left(\frac{3}{2}, \frac{d^2}{4\kappa\tau}\right)$$

Now the boundary integrals could be evaluated using the above expressions. Here the complimentary incomplete gamma functions have been replaced by analytic and

therefore well-behaved, Tricommi gamma functions with the following definition (Abramowitz and Stegun [1970]),

$$\gamma^*(a, x) = x^{-a} - \frac{x^{-a}\Gamma(a, x)}{\Gamma(a)}$$

$$\begin{aligned} G_{j,i}^{1n} &= \kappa \int_0^\tau \phi^1 \int_0^{L_j} \varphi^n G 2\pi r \, d\ell \, dt = -\frac{1}{4(\pi\kappa)^{1/2}} \int_0^{L_j} r \varphi^n \int_0^\tau \left(\frac{\tau-t}{\tau}\right) \frac{1}{(\tau-t)^{3/2}} \exp\left[-\frac{d^2}{4\kappa(4\tau-t)}\right] dt \, d\ell \\ &= -\frac{1}{8\kappa\tau\sqrt{\pi}} \int_0^{L_j} r \varphi^n d \Gamma\left(-\frac{1}{2}, \frac{d^2}{4\kappa\tau}\right) d\ell = -\frac{1}{2\kappa\sqrt{\tau}} \int_0^{L_j} r \varphi^n (-1) \left[\frac{d}{2\sqrt{\kappa\tau}} - \gamma^*\left(-\frac{1}{2}, \frac{d^2}{4\kappa\tau}\right)\right] d\ell \end{aligned}$$

$$\begin{aligned} G_{j,i}^{2n} &= \kappa \int_0^\tau \phi^2 \int_0^{L_j} \varphi^n G 2\pi r \, d\ell \, dt = -\frac{1}{2\sqrt{\pi}} \int_0^{L_j} \frac{r \varphi^n}{d} \Gamma\left(-\frac{1}{2}, \frac{d^2}{4\kappa\tau}\right) d\ell - G_{j,i}^{1n} \\ &= -\frac{1}{4\sqrt{\kappa\tau}} \int_0^{L_j} r \varphi^n \left[\frac{2\sqrt{\kappa\tau}}{d} - \gamma^*\left(\frac{1}{2}, \frac{d^2}{4\kappa\tau}\right)\right] d\ell - G_{j,i}^{1n} \end{aligned}$$

$$\begin{aligned} H_{j,i}^{1n} &= \kappa \int_0^\tau \phi^1 \int_0^{L_j} \varphi^n \left(-\frac{\partial G}{\partial n}\right) 2\pi r \, d\ell \, dt \\ &= -\frac{1}{8\kappa(\pi\kappa)^{1/2}} \int_0^{L_j} r \varphi^n \int_0^\tau \left(\frac{\tau-t}{\tau}\right) \frac{\tilde{d} \cdot \tilde{n}}{(\tau-t)^{5/2}} \exp\left[-\frac{d^2}{4\kappa(4\tau-t)}\right] dt \, d\ell \\ &= -\frac{1}{4\kappa\tau\sqrt{\pi}} \int_0^{L_j} \frac{r \varphi^n}{d} \tilde{d} \cdot \tilde{n} \Gamma\left(\frac{1}{2}, \frac{d^2}{4\kappa\tau}\right) d\ell \\ &= -\frac{1}{8(\kappa\tau)^{3/2}} \int_0^{L_j} r \varphi^n \tilde{d} \cdot \tilde{n} \left[\frac{2\sqrt{\kappa\tau}}{d} - \gamma^*\left(\frac{1}{2}, \frac{d^2}{4\kappa\tau}\right)\right] d\ell \end{aligned}$$

$$\begin{aligned}
H_{j,i}^{2n} &= \kappa \int_0^\tau \phi^2 \int_0^{L_j} \varphi^n \left(-\frac{\partial G}{\partial n} \right) 2\pi r \, d\ell \, dt = -\frac{1}{\sqrt{\pi}} \int_0^{L_j} r \varphi^n \frac{\tilde{d} \cdot \tilde{n}}{d^3} \Gamma\left(\frac{3}{2}, \frac{d^2}{4\kappa\tau}\right) d\ell - H_{j,i}^{1n} \\
&= -\frac{1}{16(\kappa\tau)^{3/2}} \int_0^{L_j} r \varphi^n \tilde{d} \cdot \tilde{n} \left[\left(\frac{2\sqrt{\kappa\tau}}{d} \right)^3 - \gamma^* \left(\frac{3}{2}, \frac{d^2}{4\kappa\tau} \right) \right] d\ell - H_{j,i}^{1n}
\end{aligned}$$

A2.2.1 Integration of singular and near singular elements

In the above integrals, out of the two integrands, the first one could cause problems during integration. Therefore they are treated with special care and where possible done analytically. For the element next to the axis, due to the source point being on the element, as the field point approaches the axis, $d \rightarrow 0$ but r/d will be a constant. Also for this element $\tilde{d} \cdot \tilde{n} = 0$, therefore,

$$\int_0^{L_j} \frac{r \varphi^n}{d} d\ell = \int_0^{L_j} \frac{|r_{j+1} - r_j|}{L_j} \varphi^n d\ell = \frac{|r_{j+1} - r_j|}{2} ; \quad \int_0^{L_j} r d \varphi^n d\ell \sim \text{regular integral}$$

$$H_{j,i}^{1n} = 0 ; \quad H_{j,i}^{21} = \left(\frac{\text{interior } \sphericalangle_i}{2\pi} \right) \delta(i, j) ; \quad H_{j,i}^{22} = \left(\frac{\text{interior } \sphericalangle_i}{2\pi} \right) \delta(i, j+1)$$

For all the other elements, 'd' can be very small and therefore near singular, thus creating a problem for the numerical integration. Therefore these terms are integrated analytically.

For the 'j'th element, 'r' and 'd' could be parameterized as,

$$r = r_j + s_{jr} \ell ; \quad z = z_j + s_{jz} \ell , \text{ therefore,}$$

$$\begin{aligned}
\int_0^{L_j} \frac{r \varphi^n}{d} dl &= \int_0^{L_j} \frac{r_j + s_{jr} \ell}{\sqrt{(r_j + s_{jr} \ell)^2 + (z_j + s_{jz} \ell - z_i)^2}} \varphi^n dl \\
&= \int_0^{L_j} \frac{r_j + s_{jr} \ell}{\sqrt{(s_{jr}^2 + s_{jz}^2) \ell^2 + 2(s_{jr} r_j + s_{jz} (z_j - z_i)) \ell + r_j^2 + (z_j - z_i)^2}} \varphi^n dl \\
&= \int_0^{L_j} \frac{r_j + s_{jr} \ell}{\sqrt{a \ell^2 + b \ell + c}} \varphi^n dl
\end{aligned}$$

For the denominator of the above integrand,

$$\Delta = 4ac - b^2 = 4[s_{jz} r_j - s_{jr} (z_j - z_i)]^2 \geq 0$$

As for the $\tilde{\mathbf{d}} \cdot \tilde{\mathbf{n}}$, after simplification could be given as,

$$\begin{aligned}
\tilde{\mathbf{d}} \cdot \tilde{\mathbf{n}} &= r n_{jr} + (z - z_i) n_{jz} = (r_j + s_{jr} \ell) n_{jr} + (z_j + s_{jz} \ell - z_i) n_{jz} \\
&= [s_{jz} r_j - s_{jr} (z_j - z_i)] = \frac{\sqrt{\Delta}}{2}
\end{aligned}$$

Thus the following integral could be expressed as,

$$\int_0^{L_j} \tilde{\mathbf{d}} \cdot \tilde{\mathbf{n}} \frac{r}{d^3} \varphi^n dl = \frac{\sqrt{\Delta}}{2} \int_0^{L_j} \frac{r_j + s_{jr} \ell}{(a \ell^2 + b \ell + c)^{3/2}} \varphi^n dl$$

Define the following integrals (Gradshteyn and Ryzhik [1980]),

$$I_1 = \int_0^{L_j} \frac{1}{\sqrt{a \ell^2 + b \ell + c}} dl = \frac{1}{\sqrt{a}} \ln \left\{ \frac{2\sqrt{a} (a L_j^2 + b L_j + c)^{1/2} + 2a L_j + b}{2\sqrt{ac} + b} \right\}$$

$$I_2 = \int_0^{L_j} \frac{\ell}{\sqrt{a \ell^2 + b \ell + c}} dl = \frac{1}{a} \left[(a L_j^2 + b L_j + c)^{1/2} - \sqrt{c} \right] - \frac{b}{2a} I_1$$

$$I_3 = \int_0^{L_j} \frac{\ell^2}{\sqrt{a\ell^2 + b\ell + c}} d\ell = \frac{1}{2a} \left[\left(L_j - \frac{3b}{2a} \right) (aL_j^2 + bL_j + c)^{1/2} + \frac{3b}{2a} \sqrt{c} + \left(\frac{3b^2}{4a} - c \right) I_1 \right]$$

$$I_4 = \int_0^{L_j} \frac{1}{(a\ell^2 + b\ell + c)^{3/2}} d\ell = \frac{2}{\Delta} \left[\frac{2aL_j + b}{(aL_j^2 + bL_j + c)^{1/2}} - \frac{b}{\sqrt{c}} \right]$$

$$I_5 = \int_0^{L_j} \frac{\ell}{(a\ell^2 + b\ell + c)^{3/2}} d\ell = -\frac{2}{\Delta} \left[\frac{2c + bL_j}{(aL_j^2 + bL_j + c)^{1/2}} - \frac{2c}{\sqrt{c}} \right]$$

$$I_6 = \int_0^{L_j} \frac{\ell^2}{(a\ell^2 + b\ell + c)^{3/2}} d\ell = -\frac{1}{a\Delta} \left[\frac{(\Delta - b^2)L_j - 2cb}{(aL_j^2 + bL_j + c)^{1/2}} + \frac{2cb}{\sqrt{c}} \right] + \frac{1}{a} I_1$$

Now the required integrals could be expressed using the above integral expression as following,

$$\int_0^{L_j} \frac{\mathbf{r}}{d} \phi^2 d\ell = \frac{1}{L_j} (r_j I_2 + s_{jr} I_3) ; \int_0^{L_j} \frac{\mathbf{r}}{d} \phi^1 d\ell = \frac{1}{L_j} (r_j I_1 + s_{jr} I_2) - \int_0^{L_j} \frac{\mathbf{r}}{d} \phi^2 d\ell$$

$$\int_0^{L_j} \tilde{\mathbf{d}} \cdot \tilde{\mathbf{n}} \frac{\mathbf{r}}{d^3} \phi^2 d\ell = \frac{\sqrt{\Delta}}{2L_j} (r_j I_5 + s_{jr} I_6) ; \int_0^{L_j} \tilde{\mathbf{d}} \cdot \tilde{\mathbf{n}} \frac{\mathbf{r}}{d^3} \phi^1 d\ell = \frac{\sqrt{\Delta}}{2L_j} (r_j I_4 + s_{jr} I_5) - \int_0^{L_j} \tilde{\mathbf{d}} \cdot \tilde{\mathbf{n}} \frac{\mathbf{r}}{d^3} \phi^2 d\ell$$

A2.3 Source point not on the symmetric axis ($r_i \neq 0$)

In this case the modified Bessel's functions I_0 and I_1 are expanded as given in Zang and Jin [1996]. The expansions are done for the small argument and for the large argument. With these expansions, integrals could be done in close form with respect to

time. This technique was used for the singular elements (elements that contained the source point) only.

The small argument expansion is valid for:

$$\frac{r r_i}{2\kappa(\tau-t)} \leq 18 \text{ and therefore } 0 \leq t \leq t_s = \tau - \frac{r r_i}{f} \text{ where } f = 36\kappa.$$

Thus the limiting 'r' for this to be valid, $r \leq r_{\text{limt}} = \tau f / r_i$. For the elements where this is valid or for the part of that this is valid, the integration with respect to time from 0 to t_s was done using the small expansion, and from t_s to τ using the large expansion. For the elements or the part of the element where $r > r_{\text{limt}}$, only the large expansion was used for the time integration from 0 to τ .

From the Zang and Jin [1996] the small expansion could be expressed where the coefficients are given for the I_0 and the I_1 , and let them be denoted as \tilde{C}_n^s and \tilde{F}_n^s respectively.

$$I_0 \left(\frac{r r_i}{2\kappa(\tau-t)} \right) = \sum_{n=0}^{N_s} \tilde{C}_n^s \left(\frac{r r_i}{36\kappa(\tau-t)} \right)^{2n}$$

$$I_1 \left(\frac{r r_i}{2\kappa(\tau-t)} \right) = \frac{r r_i}{2\kappa(\tau-t)} \sum_{n=0}^{N_s} \tilde{F}_n^s \left(\frac{r r_i}{36\kappa(\tau-t)} \right)^{2n}$$

Define $C_n^s = \tilde{C}_n^s / f^{2n}$ and $F_n^s = \tilde{F}_n^s / f^{2n}$, then,

$$I_0 \left(\frac{r r_i}{2\kappa(\tau-t)} \right) = \sum_{n=0}^{N_s} C_n^s \left(\frac{r r_i}{\tau-t} \right)^{2n}$$

$$I_1\left(\frac{r r_i}{2\kappa(\tau-t)}\right) = \frac{r r_i}{2\kappa(\tau-t)} \sum_{n=0}^{N_s} F_n^s \left(\frac{r r_i}{\tau-t}\right)^{2n}$$

Similarly for the large expansion let \tilde{C}_n^l and \tilde{F}_n^l are the given numerical coefficients and define, $C_n^l = \tilde{C}_n^l f^n$ and $F_n^l = \tilde{F}_n^l f^n$,

$$\sqrt{\frac{r r_i}{2\kappa(\tau-t)}} e^{-\left(\frac{r r_i}{2\kappa(\tau-t)}\right)} I_0\left(\frac{r r_i}{2\kappa(\tau-t)}\right) = \sum_{n=0}^{N_L} \tilde{C}_n^l \left(\frac{36\kappa(\tau-t)}{r r_i}\right)^n = \sum_{n=0}^8 C_n^l \left(\frac{\tau-t}{r r_i}\right)^n$$

$$\sqrt{\frac{r r_i}{2\kappa(\tau-t)}} e^{-\left(\frac{r r_i}{2\kappa(\tau-t)}\right)} I_1\left(\frac{r r_i}{2\kappa(\tau-t)}\right) = \sum_{n=0}^{N_L} \tilde{F}_n^l \left(\frac{36\kappa(\tau-t)}{r r_i}\right)^n = \sum_{n=0}^8 F_n^l \left(\frac{\tau-t}{r r_i}\right)^n$$

With these expansions now it is possible to express the Green's function. The parameters N_s and N_L , which are the numbers of elements in the two expansions, were chosen to give the maximum accuracy. In this case they were set at 32 and 26 respectively.

For the small expansion,

$$G = \frac{-1}{8[\pi\kappa(\tau-t)]^{3/2}} \exp\left[-\frac{r^2 + r_i^2 + (z-z_i)^2}{4\kappa(\tau-t)}\right] \sum_{n=0}^{N_s} C_n^s \left(\frac{r r_i}{\tau-t}\right)^{2n}$$

$$\left(-\frac{\partial G}{\partial n}\right) = \frac{-1}{16\kappa[\pi\kappa(\tau-t)]^{3/2}(\tau-t)} \exp\left[-\frac{r^2 + r_i^2 + (z-z_i)^2}{4\kappa(\tau-t)}\right]$$

$$\times \left\{ \tilde{d} \cdot \tilde{n} \sum_{n=0}^{N_s} C_n^s \left(\frac{r r_i}{\tau-t}\right)^{2n} + n_{jr} r_i \sum_{n=0}^{N_s} C_n^s \left(\frac{r r_i}{\tau-t}\right)^{2n} - \frac{r r_i}{2\kappa(\tau-t)} F_n^s \left(\frac{r r_i}{\tau-t}\right)^{2n} \right\}$$

For the large expansion,

$$G = \frac{-\sqrt{2}}{8\pi^{3/2}\kappa(\tau-t)\sqrt{r r_i}} \exp\left[-\frac{(r-r_i)^2+(z-z_i)^2}{4\kappa(\tau-t)}\right] \sum_{n=0}^{N_L} C_n^l \left(\frac{\tau-t}{r r_i}\right)^n$$

$$\begin{aligned} \left(-\frac{\partial G}{\partial n}\right) &= \frac{-\sqrt{2}}{16\pi^{3/2}\kappa^2(\tau-t)^2\sqrt{r r_i}} \exp\left[-\frac{(r-r_i)^2+(z-z_i)^2}{4\kappa(\tau-t)}\right] \\ &\times \left\{ \tilde{d} \cdot \tilde{n} \sum_{n=0}^{N_L} C_n^l \left(\frac{r r_i}{\tau-t}\right)^n + n_{j,r_i} \sum_{n=1}^{N_L} (C_n^l - F_n^l) \left(\frac{\tau-t}{r r_i}\right)^n \right\} \end{aligned}$$

For the small expansion the following integrals are evaluated, where expression for t_s is substituted and the following definitions are used.

$$D_s = \frac{36\kappa[r^2+r_i^2+(z-z_i)^2]}{4r r_i \kappa}; \quad D_\tau = \frac{r^2+r_i^2+(z-z_i)^2}{4\kappa\tau}$$

$$\begin{aligned} g_{j,i}^s(m) &= \int_0^{t_s} \frac{(r r_i)^{2n}}{[(\tau-t)]^{1/2+2n+m}} \exp\left[-\frac{r^2+r_i^2+(z-z_i)^2}{4\kappa(\tau-t)}\right] dt \\ &= \Gamma\left(2n-\frac{1}{2}+m\right) \left[\frac{1}{(r r_i)^{m-\frac{1}{2}}} f^{2n-\frac{1}{2}+m} \gamma^*\left(2n-\frac{1}{2}+m, \frac{r^2+r_i^2+(z-z_i)^2}{4\kappa(\tau-t_s)}\right) - \right. \\ &\quad \left. \frac{(r r_i)^{2n}}{\tau^{2n-\frac{1}{2}+m}} \gamma^*\left(2n-\frac{1}{2}+m, \frac{r^2+r_i^2+(z-z_i)^2}{4\kappa\tau}\right) \right] \\ &= \Gamma\left(2n-\frac{1}{2}+m\right) \left[\frac{1}{(r r_i)^{m-\frac{1}{2}}} f^{2n-\frac{1}{2}+m} \gamma^*\left(2n-\frac{1}{2}+m, D_s\right) - \right. \\ &\quad \left. \frac{(r r_i)^{2n}}{\tau^{2n-\frac{1}{2}+m}} \gamma^*\left(2n-\frac{1}{2}+m, D_\tau\right) \right] \end{aligned}$$

$$\int_0^{t_s} \phi^1 G dt = \frac{-1}{8(\pi\kappa)^{3/2}} \sum_{\tau, n=0}^{N_s} C_n^s g_{j,i}^s(0); \quad \int_0^{t_s} \phi^2 G dt = \frac{-1}{8(\pi\kappa)^{3/2}} \sum_{n=0}^{N_s} C_n^s g_{j,i}^s(1) - \int_0^{t_s} \phi^1 G dt$$

$$\int_0^{t_s} \phi^1 \left(-\frac{\partial G}{\partial n} \right) dt = \frac{-1}{16\kappa(\pi\kappa)^{3/2}} \sum_{\tau, n=0}^{N_s} \tilde{d} \cdot \tilde{n}_j C_n^s g_{j,i}^s(1) + n_{j,r} r_i \left(C_n^s g_{j,i}^s(1) - \frac{\Gamma_i}{2\kappa} F_n^s g_{j,i}^s(2) \right)$$

$$\begin{aligned} \int_0^{t_s} \phi^2 \left(-\frac{\partial G}{\partial n} \right) dt &= \frac{-1}{16\kappa(\pi\kappa)^{3/2}} \sum_{n=0}^{N_s} \tilde{d} \cdot \tilde{n}_j C_n^s g_{j,i}^s(2) + n_{j,r} r_i \left(C_n^s g_{j,i}^s(2) - \frac{\Gamma_i}{2\kappa} F_n^s g_{j,i}^s(3) \right) \\ &\quad - \int_0^{t_s} \phi^1 \left(-\frac{\partial G}{\partial n} \right) dt \end{aligned}$$

For the large expansion, following integrals are evaluated where E_n is the exponential integral of 'n'th order.

$$\int_{t_s}^{\tau} (\tau-t)^{n-2} \exp \left[-\frac{(r-r_i)^2 + (z-z_i)^2}{4\kappa(\tau-t)} \right] dt = (\tau-t)^{n-1} E_n \left(\frac{\bar{d}^2}{\tau-t_s} \right)$$

$$\text{where } \bar{d}^2 = \frac{(r-r_i)^2 + (z-z_i)^2}{4\kappa}$$

$$\int_{t_s}^{\tau} \phi^1 G dt = \frac{-\sqrt{2}}{8\pi^{3/2}\kappa\tau} \sum_{n=0}^{N_l} \frac{C_n^1}{(r_i r_i)^{n+1/2}} (\tau-t_s)^{n+1} E_{n+2} \left(\frac{\bar{d}^2}{\tau-t_s} \right);$$

$$\int_{t_s}^{\tau} \phi^2 G dt = \frac{-\sqrt{2}}{8\pi^{3/2}\kappa} \sum_{n=0}^{N_l} \frac{C_n^1}{(r_i r_i)^{n+1/2}} (\tau-t_s)^n E_{n+1} \left(\frac{\bar{d}^2}{\tau-t_s} \right) - \int_{t_s}^{\tau} \phi^1 G dt$$

$$\int_{t_s}^{\tau} \phi^1 \left(-\frac{\partial G}{\partial \mathbf{n}} \right) dt = \frac{-\sqrt{2}}{16\pi^{3/2} \kappa^2 \tau \sqrt{r_i}} \left[\begin{aligned} & \tilde{\mathbf{d}} \cdot \tilde{\mathbf{n}}_j \sum_{n=0}^{N_L} \frac{C_n^1}{(r_i)^n} (\tau - t_s)^n E_{n+1} \left(\frac{\bar{d}^2}{\tau - t_s} \right) \\ & + n_{jr} r_i \sum_{n=1}^{N_L} \frac{C_n^1 - F_n^1}{(r_i)^n} (\tau - t_s)^n E_{n+1} \left(\frac{\bar{d}^2}{\tau - t_s} \right) \end{aligned} \right]$$

$$\int_{t_s}^{\tau} \phi^2 \left(-\frac{\partial G}{\partial \mathbf{n}} \right) dt = \frac{-\sqrt{2}}{16\pi^{3/2} \kappa^2 \sqrt{r_i}} \left[\begin{aligned} & \tilde{\mathbf{d}} \cdot \tilde{\mathbf{n}}_j \sum_{n=0}^{N_L} \frac{C_n^1}{(r_i)^n} (\tau - t_s)^{n-1} E_n \left(\frac{\bar{d}^2}{\tau - t_s} \right) \\ & + n_{jr} r_i \sum_{n=1}^{N_L} \frac{C_n^1 - F_n^1}{(r_i)^n} (\tau - t_s)^{n-1} E_n \left(\frac{\bar{d}^2}{\tau - t_s} \right) \end{aligned} \right] - \int_{t_s}^{\tau} \phi^1 \left(-\frac{\partial G}{\partial \mathbf{n}} \right) dt$$

Now if , $r \leq r_{lm}$

$$\int_{t_s}^{\tau} \phi^1 G dt = \frac{-\sqrt{2} r_i}{8\pi^{3/2} \kappa f \tau} \sum_{n=0}^{N_L} \frac{C_n^1}{f^n} E_{n+2} (d_s^2);$$

$$\int_{t_s}^{\tau} \phi^2 G dt = \frac{-\sqrt{2}}{8\pi^{3/2} \kappa \sqrt{r_i}} \sum_{n=0}^{N_L} \frac{C_n^1}{f^n} E_{n+1} (d_s^2) - \int_{t_s}^{\tau} \phi^1 G dt$$

$$\int_{t_s}^{\tau} \phi^1 \left(-\frac{\partial G}{\partial \mathbf{n}} \right) dt = \frac{-\sqrt{2}}{16\pi^{3/2} \kappa^2 \tau \sqrt{r_i}} \left[\begin{aligned} & \tilde{\mathbf{d}} \cdot \tilde{\mathbf{n}}_j \sum_{n=0}^{N_L} \frac{C_n^1}{f^n} E_{n+1} (d_s^2) \\ & + n_{jr} r_i \sum_{n=1}^{N_L} \frac{C_n^1 - F_n^1}{f^n} E_{n+1} (d_s^2) \end{aligned} \right]$$

$$\int_{t_s}^{\tau} \phi^2 \left(-\frac{\partial G}{\partial \mathbf{n}} \right) dt = \frac{-\sqrt{2} f}{16\pi^{3/2} \kappa^2 r_i \sqrt{r_i}} \left[\begin{aligned} & \tilde{\mathbf{d}} \cdot \tilde{\mathbf{n}}_j \sum_{n=0}^{N_L} \frac{C_n^1}{f^n} E_n (d_s^2) \\ & + n_{jr} r_i \sum_{n=1}^{N_L} \frac{(C_n^1 - F_n^1)}{f^n} E_n (d_s^2) \end{aligned} \right] - \int_{t_s}^{\tau} \phi^1 \left(-\frac{\partial G}{\partial \mathbf{n}} \right) dt$$

Else if , $r > r_{imt}$

$$\int_0^\tau \phi^1 G dt = \frac{-\sqrt{2}}{8\pi^{3/2} \kappa \sqrt{r r_i}} \sum_{n=0}^{N_i} \frac{C_n^1}{(r r_i)^n} \tau^n E_{n+2}(d_\tau^2);$$

$$\int_0^\tau \phi^2 G dt = \frac{-\sqrt{2}}{8\pi^{3/2} \kappa \sqrt{r r_i}} \sum_{n=0}^{N_i} \frac{C_n^1}{(r r_i)^n} \tau^n E_{n+1}(d_\tau^2) - \int_0^\tau \phi^1 G dt$$

$$\int_0^\tau \phi^1 \left(-\frac{\partial G}{\partial n} \right) dt = \frac{-\sqrt{2}}{16\pi^{3/2} \kappa^2 \tau \sqrt{r r_i}} \left[\begin{array}{l} \tilde{d} \cdot \tilde{n}_j \sum_{n=0}^{N_i} \frac{C_n^1}{(r r_i)^n} \tau^n E_{n+1}(d_\tau^2) \\ + n_{jr} r_i \sum_{n=1}^{N_i} \frac{C_n^1 - F_n^1}{(r r_i)^n} \tau^n E_{n+1}(d_\tau^2) \end{array} \right]$$

$$\int_0^\tau \phi^2 \left(-\frac{\partial G}{\partial n} \right) dt = \frac{-\sqrt{2}}{16\pi^{3/2} \kappa^2 \tau \sqrt{r r_i}} \left[\begin{array}{l} \tilde{d} \cdot \tilde{n}_j \sum_{n=0}^{N_i} \frac{C_n^1}{(r r_i)^n} \tau^n E_n(d_\tau^2) \\ + n_{jr} r_i \sum_{n=1}^{N_i} \frac{C_n^1 - F_n^1}{(r r_i)^n} \tau^n E_n(d_\tau^2) \end{array} \right] - \int_0^\tau \phi^1 \left(-\frac{\partial G}{\partial n} \right) dt$$

$$\text{Where } d_s^2 = \frac{f \left[(r - r_i)^2 + (z - z_i)^2 \right]}{4r r_i \kappa}; \quad d_\tau^2 = \frac{(r - r_i)^2 + (z - z_i)^2}{4\kappa \tau}$$

Finally considering the most general case where L_{jimt} correspond to r_{imt} and also considering that for the singular elements, $\tilde{d} \cdot \tilde{n} = 0$ and the only contribution comes from the E_0 which becomes a Dirac delta function as the argument tends to zero, the spatial integration could be denoted as follows.

$$\begin{aligned}
G_{j,i}^{1m} &= \kappa \int_0^\tau \phi^1 \int_0^{L_j} \varphi^m G 2\pi r \, d\ell \, dt = \int_0^\tau \phi^1 \int_0^{L_{j\text{limt}}} \varphi^m G 2\pi r \, d\ell \, dt + \int_0^\tau \phi^1 \int_{L_{j\text{limt}}}^{L_j} \varphi^m G 2\pi r \, d\ell \, dt \\
&= \frac{-1}{4\sqrt{\pi\kappa\tau}} \sum_{n=0}^{N_s} C_n^s \int_0^{L_{j\text{limt}}} \varphi^m r g_{j,i}^s(0) \, d\ell - \frac{\sqrt{2r_i}}{4f\tau\sqrt{\pi}} \sum_{n=0}^{N_L} \frac{C_n^1}{f^n} \int_0^{L_{j\text{limt}}} \varphi^m r \sqrt{r} E_{n+2}(d_s^2) \, d\ell \\
&\quad - \frac{\sqrt{2}}{4\sqrt{\pi}} \sum_{n=0}^{N_L} C_n^1 \tau^n \int_{L_{j\text{limt}}}^{L_j} \frac{r}{(r_i)^{n+\frac{1}{2}}} \varphi^m E_{n+2}(d_\tau^2) \, d\ell
\end{aligned}$$

$$\begin{aligned}
G_{j,i}^{2m} &= \kappa \int_0^\tau \phi^2 \int_0^{L_j} \varphi^m G 2\pi r \, d\ell \, dt = \int_0^\tau \phi^2 \int_0^{L_{j\text{limt}}} \varphi^m G 2\pi r \, d\ell \, dt + \int_0^\tau \phi^2 \int_{L_{j\text{limt}}}^{L_j} \varphi^m G 2\pi r \, d\ell \, dt \\
&= \frac{-1}{4\sqrt{\pi\kappa\tau}} \sum_{n=0}^{N_s} C_n^s \int_0^{L_{j\text{limt}}} \varphi^m r g_{j,i}^s(1) \, d\ell - \frac{\sqrt{2}}{4\sqrt{\pi}\sqrt{r_i}} \sum_{n=0}^{N_L} \frac{C_n^1}{f^n} \int_0^{L_{j\text{limt}}} \varphi^m \sqrt{r} E_{n+1}(d_s^2) \, d\ell \\
&\quad - \frac{\sqrt{2}}{4\sqrt{\pi}} \sum_{n=0}^{N_L} \frac{C_n^1}{(r_i)^{n+\frac{1}{2}}} \tau^n \int_{L_{j\text{limt}}}^{L_j} \frac{\sqrt{r}}{r^n} \varphi^m E_{n+1}(d_\tau^2) \, d\ell - G_{j,i}^{1m}
\end{aligned}$$

Similarly,

$$\begin{aligned}
H_{j,i}^{1m} &= \kappa \int_0^\tau \phi^1 \int_0^{L_j} \varphi^m \left(-\frac{\partial G}{\partial n} \right) 2\pi r \, d\ell \, dt = \frac{-n_{jr} r_i}{8\kappa\sqrt{\pi\kappa\tau}} \sum_{n=0}^{N_s} C_n^s \int_0^{L_{j\text{limt}}} \varphi^m r \left(C_n^s g_{j,i}^s(1) - \frac{r_i}{2\kappa} F_n^s g_{j,i}^s(2) \right) \, d\ell \\
&\quad - \frac{\sqrt{2r_i} n_{jr}}{8\kappa\tau\sqrt{\pi}} \sum_{n=1}^{N_L} \frac{C_n^1 - F_n^1}{f^n} \int_0^{L_{j\text{limt}}} \varphi^m \sqrt{r} E_{n+1}(d_s^2) \, d\ell - \frac{\sqrt{2r_i} n_{jr}}{8\kappa\tau\sqrt{\pi}} \sum_{n=1}^{N_L} \frac{C_n^1 - F_n^1}{r_i^n} \tau^n \int_{L_{j\text{limt}}}^{L_j} \varphi^m \frac{\sqrt{r}}{r^n} E_{n+1}(d_\tau^2) \, d\ell
\end{aligned}$$

$$\begin{aligned}
H_{j,i}^{2m} &= \kappa \int_0^\tau \phi^2 \int_0^{L_j} \varphi^m \left(-\frac{\partial G}{\partial n} \right) 2\pi r \, d\ell \, dt = \frac{-n_{jr} r_i}{8\kappa\sqrt{\pi\kappa\tau}} \sum_{n=0}^{N_s} C_n^s \int_0^{L_{j\text{limt}}} \varphi^m r \left(C_n^s g_{j,i}^s(2) - \frac{r_i}{2\kappa} F_n^s g_{j,i}^s(3) \right) \, d\ell \\
&\quad - \frac{\sqrt{2} f n_{jr}}{8\sqrt{\pi}\sqrt{r_i}\kappa\tau} \sum_{n=1}^{N_L} \frac{C_n^1 - F_n^1}{f^n} \int_0^{L_{j\text{limt}}} \varphi^m \sqrt{r} E_n(d_s^2) \, d\ell - \frac{\sqrt{2r_i} n_{jr}}{8\kappa\tau\sqrt{\pi}} \sum_{n=1}^{N_L} \frac{C_n^1 - F_n^1}{r_i^n} \tau^n \int_{L_{j\text{limt}}}^{L_j} \varphi^m \frac{\sqrt{r}}{r^n} E_n(d_\tau^2) \, d\ell \\
&\quad - H_{j,i}^{1m}
\end{aligned}$$

Similar derivations could be obtained for the (j-1) th element.

Due to the Dirac delta function arising from the singularity these should be modified as,

$$H_{j,i}^{21} = H_{j,i}^{21} + \left(\frac{\text{interior } \angle_i}{4\pi} \right) \delta(i, j); H_{j-1,i}^{22} = H_{j-1,i}^{22} + \left(\frac{\text{interior } \angle_i}{4\pi} \right) \delta(i, j)$$

A3 Upper Bounds of the Integral Coefficients

Define $r_{\max} = \max\{r_j, r_{j+1}\}$ and $d_{\min}^2 = \min\{(r_j - r_i)^2 + (z_j - z_i)^2, (r_{j+1} - r_i)^2 + (z_{j+1} - z_i)^2\}$

$$dn_{\max} = \max\left\{ |(r_j - r_i)n_r + (z_j - z_i)n_z| + r_{\max}|n_r|, |(r_{j+1} - r_i)n_r + (z_{j+1} - z_i)n_z| + r_{\max}|n_r| \right\}$$

$$|G_{j,i}^{1n}| = \left| \kappa \int_0^\tau \phi^1 \int_0^{L_j} \varphi^n G 2\pi r \, d\ell \, dt \right| \leq \frac{r_{\max} L_j \sqrt{d_{\min}^2}}{8\kappa\tau\sqrt{\pi}} \Gamma\left(-\frac{1}{2}, \frac{d_{\min}^2}{4\kappa\tau}\right)$$

$$|G_{j,i}^{2n}| = \left| \kappa \int_0^\tau \phi^2 \int_0^{L_j} \varphi^n G 2\pi r \, d\ell \, dt \right| \leq \frac{r_{\max} L_j}{2\sqrt{d_{\min}^2} \sqrt{\pi}} \Gamma\left(\frac{1}{2}, \frac{d_{\min}^2}{4\kappa\tau}\right)$$

$$|H_{j,i}^{1n}| = \left| \kappa \int_0^\tau \phi^1 \int_0^{L_j} \varphi^n \left(-\frac{\partial G}{\partial n} \right) 2\pi r \, d\ell \, dt \right| \leq \frac{r_{\max} L_j dn_{\max}}{4\kappa\tau\sqrt{d_{\min}^2} \sqrt{\pi}} \Gamma\left(\frac{1}{2}, \frac{d_{\min}^2}{4\kappa\tau}\right)$$

$$|H_{j,i}^{2n}| = \left| \kappa \int_0^\tau \phi^2 \int_0^{L_j} \varphi^n \left(-\frac{\partial G}{\partial n} \right) 2\pi r \, d\ell \, dt \right| \leq \frac{r_{\max} L_j dn_{\max}}{(d_{\min}^2)^{3/2} \sqrt{\pi}} \Gamma\left(\frac{3}{2}, \frac{d_{\min}^2}{4\kappa\tau}\right)$$

$$L_{\max} = \left\{ \max\left[|r_{j+1}(t) - r_j(t)| + |z_{j+1}(t) - z_j(t)| \right], t \in [0, \tau] \right\}$$

$$r_{\max} = \left\{ \max\left[r_j(t), r_{j+1}(t) \right], t \in [0, \tau] \right\}$$

$$d_{\min}^2 = \left\{ \min \left[(r - r_i)^2 + (z - z_i)^2 \right], r \in [r_j(t), r_{j+1}(t)], \forall t \in [0, \tau] \right\}$$

$$dn_{\max} =$$

$$\left\{ \max \left[\left| [r - r_i] n_r(r) + [z_j(r) - z_i] n_z(r) \right| + r_{\max} |n_r(r)| \right], r \in [r_j(t), r_{j+1}(t)], \forall t \in [0, \tau] \right\}$$

$$|P_{j,i}^{1n}| = \left| \int_0^\tau \phi^1 \int_{r_j(t)}^{r_{j+1}(t)} \varphi^n G 2\pi r \sqrt{1 + S'(r)^2} dr dt \right| \leq \frac{r_{\max} L_{\max} \sqrt{d_{\min}^2}}{8\kappa\tau\sqrt{\pi}} \Gamma\left(-\frac{1}{2}, \frac{d_{\min}^2}{4\kappa\tau}\right)$$

$$|P_{j,i}^{2n}| = \left| \int_0^\tau \phi^2 \int_{r_j(t)}^{r_{j+1}(t)} \varphi^n G 2\pi r \sqrt{1 + S'(r)^2} dr dt \right| \leq 2\sqrt{d_{\min}^2} \frac{r_{\max} L_{\max}}{\sqrt{\pi}} \Gamma\left(\frac{1}{2}, \frac{d_{\min}^2}{4\kappa\tau}\right)$$

$$|Q_{j,i}^{1n}| = \left| \int_0^\tau \phi^1 \int_{r_j(t)}^{r_{j+1}(t)} \varphi^n \left(-\frac{\partial G}{\partial n}\right) 2\pi r \sqrt{1 + S'(r)^2} dr dt \right| \leq \frac{r_{\max} L_{\max} dn_{\max}}{4\kappa\tau\sqrt{d_{\min}^2}\sqrt{\pi}} \Gamma\left(\frac{1}{2}, \frac{d_{\min}^2}{4\kappa\tau}\right)$$

$$|Q_{j,i}^{2n}| = \left| \int_0^\tau \phi^2 \int_{r_j(t)}^{r_{j+1}(t)} \varphi^n \left(-\frac{\partial G}{\partial n}\right) 2\pi r \sqrt{1 + S'(r)^2} dr dt \right| \leq \frac{r_{\max} L_{\max} dn_{\max}}{(d_{\min}^2)^{3/2}\sqrt{\pi}} \Gamma\left(\frac{3}{2}, \frac{d_{\min}^2}{4\kappa\tau}\right)$$

APPENDIX B

B1 Spatial Integral Coefficients

The following definitions are used for the coefficients found in Eqns. (3.37) and (3.40). For the node given by the spatial index i and $t = n$:

$$[A_0^+]_i^n = \int_{\varphi_i}^{\varphi_{i+1/2}} r(\varphi) d\varphi \quad ; \quad [A_0^-]_i^n = \int_{\varphi_{i-1/2}}^{\varphi_i} r(\varphi) d\varphi$$

$$[A_1^+]_i^n = \int_{\varphi_i}^{\varphi_{i+1/2}} (\varphi - \varphi_i) r(\varphi) d\varphi \quad ; \quad [A_1^-]_i^n = \int_{\varphi_{i-1/2}}^{\varphi_i} (\varphi - \varphi_i) r(\varphi) d\varphi$$

For the node $i - 1/2$ and $t = n - 1/2$:

$$[A_0^-]_{i-1/2}^{n-1/2} = \int_{\varphi_{i-1/2}}^{\varphi_i} r(\varphi) d\varphi \quad ; \quad [A_1^-]_{i-1/2}^{n-1/2} = \int_{\varphi_{i-1/2}}^{\varphi_i} (\varphi - \varphi_{i-1/2}) r(\varphi) d\varphi$$

$$[A_2^-]_{i-1/2}^{n-1/2} = \int_{\varphi_{i-1/2}}^{\varphi_i} d\varphi \quad ; \quad [A_3^-]_{i-1/2}^{n-1/2} = \int_{\varphi_{i-1/2}}^{\varphi_i} (\varphi - \varphi_{i-1/2}) d\varphi$$

For the node $i + 1/2$ and $t = n - 1/2$:

$$[A_0^+]_{i+1/2}^{n-1/2} = \int_{\varphi_i}^{\varphi_{i+1/2}} r(\varphi) d\varphi \quad ; \quad [A_1^+]_{i+1/2}^{n-1/2} = \int_{\varphi_i}^{\varphi_{i+1/2}} (\varphi - \varphi_{i+1/2}) r(\varphi) d\varphi$$

$$[A_2^+]_{i+1/2}^{n-1/2} = \int_{\varphi_i}^{\varphi_{i+1/2}} d\varphi \quad ; \quad [A_3^+]_{i+1/2}^{n-1/2} = \int_{\varphi_i}^{\varphi_{i+1/2}} (\varphi - \varphi_{i+1/2}) d\varphi$$

B2 Partial Time derivative: f_{jt}

From the conservation Eqn. (3.31),

$$\frac{\partial}{\partial t}[\phi_k] = -\frac{1}{r} \frac{\partial}{\partial \varphi} r [f_k] + [S_k] + \frac{1}{r} [R_k] = -\frac{1}{r} \frac{\partial r}{\partial \varphi} [f_k] - [f_{k\varphi}] - \left(\frac{\partial f_k}{\partial \phi_m} \right) \left(\frac{\partial \phi_m}{\partial \varphi} \right) + [S_k] + \frac{1}{r} [R_k]$$

$$[f_{jt}] = \frac{\partial f_j}{\partial \phi_k} \frac{\partial}{\partial t} [\phi_k],$$

Substituting gives,

$$[f_{jt}] = \frac{\partial f_j}{\partial \phi_k} \left(-\frac{1}{r} \frac{\partial r}{\partial \varphi} [f_k] - [f_{k\varphi}] - \left(\frac{\partial f_k}{\partial \phi_m} \right) \left(\frac{\partial \phi_m}{\partial \varphi} \right) + [S_k] + \frac{1}{r} [R_k] \right)$$

B3 Partial derivatives of [S] and [R]

$$[S_{j\varphi}] = \left(\frac{\partial S_j}{\partial \phi_k} \right) [\phi_{k\varphi}] \quad ; \quad [R_{j\varphi}] = \left(\frac{\partial R_j}{\partial \phi_k} \right) [\phi_{k\varphi}]$$

$$[S_{jt}] = \left(\frac{\partial S_j}{\partial \phi_k} \right) [\phi_{kt}] = \left(\frac{\partial S_j}{\partial \phi_k} \right) \left(-\frac{1}{r} \frac{\partial r}{\partial \varphi} [f_k] - [f_{k\varphi}] - \left(\frac{\partial f_k}{\partial \phi_m} \right) \left(\frac{\partial \phi_m}{\partial \varphi} \right) + [S_k] + \frac{1}{r} [R_k] \right)$$

$$[R_{jt}] = \left(\frac{\partial R_j}{\partial \phi_k} \right) [\phi_{kt}] = \left(\frac{\partial R_j}{\partial \phi_k} \right) \left(-\frac{1}{r} \frac{\partial r}{\partial \varphi} [f_k] - [f_{k\varphi}] - \left(\frac{\partial f_k}{\partial \phi_m} \right) \left(\frac{\partial \phi_m}{\partial \varphi} \right) + [S_k] + \frac{1}{r} [R_k] \right)$$

B4 Spatial gradient of [f]

$$\left[\frac{\partial f_k}{\partial \varphi} \right] \equiv [f_{k\varphi}] = \begin{bmatrix} -\frac{\phi_1 \dot{s}}{s} \\ -\frac{\phi_2 \dot{s}}{s} \\ -\frac{\phi_3 \dot{s}}{s} \end{bmatrix}$$

B5 Jacobian of [f]

$$\left[\frac{\partial f_j}{\partial \phi_k} \right] \equiv [J_f] = \begin{bmatrix} -\frac{\varphi \dot{s}}{s} & \frac{2}{3s} & 0 \\ \left(-\frac{4\phi_2^2}{5\phi_1^2} + \frac{3p}{2\rho_\ell} + \frac{3\phi_1}{2\rho_\ell} \frac{\partial p}{\partial \phi_1} \right) \frac{1}{s} & \left(\frac{8\phi_2}{5\phi_1} - \varphi \dot{s} \right) \frac{1}{s} & \frac{3\phi_1}{2\rho_\ell s} \frac{\partial p}{\partial \phi_3} \\ -\frac{5\phi_3\phi_2}{6\phi_1^2 s} & \left(\frac{5\phi_3}{6\phi_1} - \frac{T_0}{6} \right) \frac{1}{s} & \left(\frac{5\phi_2}{6\phi_1} - \varphi \dot{s} \right) \frac{1}{s} \end{bmatrix}$$

B6 Jacobean of [S] and [R]

$$[J_s] \equiv \left[\frac{\partial S_j}{\partial \phi_k} \right] \text{ where,}$$

$$S_{11} = -\frac{\dot{s}}{s} \frac{\partial \tilde{v}_1}{\partial \phi_1} + \frac{\partial v_0}{\partial \phi_1} \quad ; \quad S_{12} = 0 \quad ; \quad S_{13} = -\frac{\partial \tilde{v}_1}{\partial \phi_3} + \frac{\partial v_0}{\partial \phi_3}$$

$$S_{21} = \frac{3}{2\rho_\ell s} \frac{\partial \phi_1}{\partial \varphi} \frac{\partial p}{\partial \phi_1} + \frac{3}{2} \left(\tilde{v}_1 \frac{\phi_2}{\phi_1^2} - \frac{\phi_2}{\phi_1} \frac{\partial \tilde{v}_1}{\partial \phi_1} \right) + \frac{6\mu r^2}{\rho_\ell} \frac{\phi_2}{\phi_1^3} + \frac{3}{2} g_x$$

$$S_{22} = -\frac{\dot{s}}{s} - \frac{3\tilde{v}_1}{2\phi_1} - \frac{3\mu}{\rho_\ell \phi_1^2} \quad ; \quad S_{23} = \frac{3}{2\rho_\ell s} \frac{\partial \phi_1}{\partial \varphi} \frac{\partial p}{\partial \phi_3} - \frac{3\phi_2}{2\phi_1} \frac{\partial \tilde{v}_1}{\partial \phi_3}$$

$$S_{31} = \frac{2\phi_3 \tilde{v}_1}{\phi_1^2} - \frac{2\phi_3}{\phi_1} \frac{\partial \tilde{v}_1}{\partial \phi_1} + T_0 \left(\frac{\partial \tilde{v}_1}{\partial \phi_1} + \frac{\partial v_0}{\partial \phi_1} \right) + 4\kappa_\ell \frac{\phi_3}{\phi_1^3} - 2\kappa_\ell \frac{T_0}{\phi_1^2} + \frac{\partial}{\partial \phi_1} \left(\kappa_\ell \frac{\partial T_\ell}{\partial y} \Big|_{\ell-v} \right) - \frac{\mu}{\rho_\ell c_\ell} \left(\frac{4\phi_2^2}{\phi_1^4} \right)$$

$$S_{32} = \frac{\mu}{\rho_\ell c_\ell} \left(\frac{8 \phi_2}{3 \phi_1^3} \right)$$

$$S_{33} = -\frac{\dot{s}}{s} - \frac{2\tilde{v}_1}{\phi_1} - \frac{2\phi_3}{\phi_1} \frac{\partial \tilde{v}_1}{\partial \phi_3} + T_0 \left(\frac{\partial \tilde{v}_1}{\partial \phi_3} + \frac{\partial v_0}{\partial \phi_3} \right) - \frac{2\kappa_\ell}{\phi_1^2} + \frac{\partial}{\partial \phi_3} \left(\kappa_\ell \frac{\partial T_\ell}{\partial y} \Big|_{\ell-v} \right)$$

$$[J_R] \equiv \left[\frac{\partial R_j}{\partial \phi_k} \right] = \begin{bmatrix} -\frac{\partial r}{\partial \phi} \frac{\phi \dot{s}}{s} & 0 & 0 \\ \frac{3}{2\rho_\ell s} \left(p + \phi_1 \frac{\partial p}{\partial \phi_1} \right) \frac{\partial r}{\partial \phi} & -\frac{\partial r}{\partial \phi} \frac{\phi \dot{s}}{s} & 0 \\ -\frac{\phi \dot{s}}{s} \frac{\partial r}{\partial \phi} & 0 & 0 \end{bmatrix}$$

B7 Partial derivative of physical variables

$$\frac{\partial p}{\partial \phi_1} = -p \left(\frac{H_1}{G} \right) \frac{2\phi_3}{(2\phi_3 - \phi_1 T_0)^2} ; \quad \frac{\partial p}{\partial \phi_2} = 0 ; \quad \frac{\partial p}{\partial \phi_3} = p \left(\frac{H_1}{G} \right) \frac{2\phi_1}{(2\phi_3 - \phi_1 T_0)^2}$$

$$\frac{\partial \tilde{v}_1}{\partial \phi_1} = \tilde{v}_1 \left[\frac{\phi_3}{\phi_1 (2\phi_3 - \phi_1 T_0)} - \frac{H_1}{G} \frac{2\phi_3}{(2\phi_3 - \phi_1 T_0)^2} \right] ; \quad \frac{\partial \tilde{v}_1}{\partial \phi_2} = 0$$

$$\frac{\partial \tilde{v}_1}{\partial \phi_3} = \tilde{v}_1 \left[\frac{-1}{(2\phi_3 - \phi_1 T_0)} + \frac{H_1}{G} \frac{2\phi_1}{(2\phi_3 - \phi_1 T_0)^2} \right] ; \quad \frac{\partial v_0}{\partial \phi_1} = \frac{2\kappa_\ell}{H_0 \rho_\ell} \left[\frac{(\phi_1 T_0 - 2\phi_3)}{\phi_1^3} \right] ; \quad \frac{\partial v_0}{\partial \phi_2} = 0$$

$$\frac{\partial v_0}{\partial \phi_3} = \frac{2\kappa_\ell}{H_0 \rho_\ell} \frac{1}{\phi_1^2} ; \quad \frac{\partial}{\partial \phi_1} \left(\kappa_\ell \frac{\partial T_\ell}{\partial y} \Big|_{\ell-v} \right) = -\frac{H_1}{c_\ell} \frac{\partial \tilde{v}_1}{\partial \phi_1} ; \quad \frac{\partial}{\partial \phi_3} \left(\kappa_\ell \frac{\partial T_\ell}{\partial y} \Big|_{\ell-v} \right) = -\frac{H_1}{c_\ell} \frac{\partial \tilde{v}_1}{\partial \phi_3}$$

APPENDIX C

C1 Analytical solution for the constant heat flux case

For the finite domain:

$$\tilde{T}^1(r, z, t) = \left(\frac{Q_0}{kH} \right) \left(\kappa t - Hz + \frac{z^2}{2} \right) + \frac{Q_0 H}{3k} - \frac{2Q_0 H}{k} \sum_{m=1}^{\infty} \frac{1}{(m\pi)^2} \cos\left(\frac{m\pi z}{H} \right) \exp\left(-\frac{\kappa m^2 \pi^2 t}{H^2} \right)$$

For the semi infinite domain in the z-direction:

$$\tilde{T}^2(r, z, t) = \frac{Q_0 \sqrt{\kappa}}{k} \left[2\sqrt{\frac{t}{\pi}} \exp\left(-\frac{z^2}{4\kappa t} \right) - \frac{z}{\sqrt{\kappa}} \operatorname{erfc}\left(\frac{z}{2\sqrt{\kappa t}} \right) \right]$$

Solution to the constant heat flux model problem:

$$T_{\text{const}}(r, z, t) = \tilde{T}^j(r, z, t) + T_0 \quad j=1 \text{ or } 2$$

C2 Analytical solution for the variable flux case

For the finite domain:

$$\begin{aligned} T^3(r, z, t) = & \tilde{T}^1(r, z, t) - \left[\frac{7Q_0 \kappa t}{10Hk} + \frac{14Q_0 H}{60k} - \frac{Q_0}{Hk} \left(3\left(\frac{r}{a} \right)^2 - 2\left(\frac{r}{a} \right)^3 \right) \left(Hz - \frac{z^2}{2} \right) \right. \\ & + \left(\frac{12Q_0 H}{a^5 k} \right) \sum_{n=1}^{\infty} \frac{1}{\mu_n^4 J_0^2(\mu_n a)} \left\{ \left[\frac{3}{\mu_n^2 H^2} \right] \left[1 - \exp(-\kappa \mu_n^2 t) \right] + 1 \right\} (a J_0(\mu_n a) - I_n) J_0(\mu_n r) \\ & - \left(\frac{7Q_0 H}{5\pi^2 k} \right) \sum_{m=1}^{\infty} \frac{1}{m^2} \exp\left(-\frac{\kappa m^2 \pi^2 t}{H^2} \right) \cos\left(\frac{m\pi z}{H} \right) \\ & - \left(\frac{72Q_0 H}{\pi^2 a^5 k} \right) \sum_{m=1}^{\infty} \sum_{n=1}^{\infty} \frac{1}{m^2 \mu_n^4 \left(\mu_n^2 + \frac{m^2 \pi^2}{H^2} \right) J_0^2(\mu_n a)} \left\{ \mu_n^2 + \frac{m^2 \pi^2}{H^2} \exp\left[-\kappa \left(\mu_n^2 + \frac{m^2 \pi^2}{H^2} \right) t \right] \right\} \\ & \left. \times (a J_0(\mu_n a) - I_n) J_0(\mu_n r) \cos\left(\frac{m\pi z}{H} \right) \right] \end{aligned}$$

For the semi infinite domain in the z-direction:

$$\begin{aligned} \tilde{T}^4(r, z, t) = \tilde{T}^2(r, z, t) & - \left[\frac{7Q_0\sqrt{\kappa}}{10k} \left\{ 2\sqrt{\frac{t}{\pi}} \exp\left(-\frac{z^2}{4\kappa t}\right) - \frac{z}{\sqrt{\kappa}} \operatorname{erfc}\left(\frac{z}{2\sqrt{\kappa t}}\right) \right\} \right. \\ & + \left. \left(\frac{72Q_0\sqrt{\kappa}}{a^5 k} \right) \sum_{n=1}^{\infty} \frac{(aJ_0(\mu_n a) - I_n)J_0(\mu_n r)}{\mu_n^4 J_0^2(\mu_n a)} \left\{ \sqrt{t} \exp\left(-\frac{z^2}{4\kappa t}\right) \exp(\kappa\mu_n t) \right. \right. \\ & \quad - \kappa\mu_n \left(\frac{z^2}{4\kappa}\right)^{3/2} \sum_{m=0}^{\infty} \frac{1}{m!} \left(\frac{z^2\mu_n}{4}\right)^m \Gamma\left(-m - \frac{3}{2}, \frac{z^2}{4\kappa t}\right) \\ & \quad \left. \left. - \left(\frac{z^2}{4\kappa}\right)^{1/2} \sum_{m=0}^{\infty} \frac{1}{m!} \left(\frac{z^2\mu_n}{4}\right)^m \Gamma\left(-m + \frac{1}{2}, \frac{z^2}{4\kappa t}\right) \right\} \right] \end{aligned}$$

Solution to the variable heat flux model problem:

$$T_{\text{variable}}(r, z, t) = \tilde{T}^j(r, z, t) + T_0 \quad j = 3 \text{ or } 4$$

Where μ_n are the zeros of Bessel function $J_1(\mu a)$ and I_n is defined by,

$$I_n = \int_0^a J_0(\mu_n r) dr$$

APPENDIX D

D1 Derivation of the Shallow-Water Equations in Axisymmetric Coordinates

Kinematic equation at the surface:

$$\frac{\partial \delta}{\partial t} + u_{\delta} \frac{\partial \delta}{\partial r} - v_{\delta} = 0$$

Continuity equation:

$$\frac{\partial ru}{\partial r} + \frac{\partial rv}{\partial z} = 0$$

Here δ is the height to the free surface and v_{δ} is the velocity of it in the z-direction.

Integrating the continuity equation:

$$\int_0^{\delta} \frac{\partial ru}{\partial r} dz + v_{\delta} = 0$$

Using the Leibnitz rule and free surface equation, where u_1 is the depth averaged velocity,

$$\frac{\partial \delta}{\partial t} + \frac{1}{r} \frac{\partial u_1 \delta r}{\partial r} = 0 \tag{D.1}$$

Momentum equation, where forcing terms are neglected,

$$\frac{\partial u}{\partial t} + u \frac{\partial u}{\partial r} + v \frac{\partial u}{\partial z} = 0$$

Integrating across the layer,

$$\int_0^{\delta} \frac{\partial u}{\partial t} dz + \frac{1}{r} \int_0^{\delta} \left[\frac{\partial ru^2}{\partial r} \right] dz + ru_{\delta} v_{\delta} = 0$$

Using the Leibnitz rule and the free surface equation,

$$\frac{\partial u_1 \delta}{\partial t} + \frac{1}{r} \frac{\partial u_1^2 \delta r}{\partial r} = 0 \quad (\text{D.2})$$

Linearise Eqns. (D.1) and (D.2),

$$r u_1 \delta = Q = Q_0 + Q' \quad ; \quad r \delta = A = A_0 + A'$$

$$\frac{\partial \delta}{\partial t} + \frac{1}{r} \frac{\partial r(u_1 \delta)}{\partial r} = 0 \quad (\text{D.3})$$

$$\frac{\partial u_1 \delta}{\partial t} + \frac{1}{r} \left[\frac{2Q_0}{A_0} \frac{\partial r u_1 \delta}{\partial r} - \frac{Q_0^2}{A_0^2} \frac{\partial r \delta}{\partial r} \right] = 0 \quad (\text{D.4})$$

D2 Space-Time system of equations

Using numerical values for the coefficients, Eqns. (D.3) and (D.4) could be represented as follows.

$$\frac{\partial}{\partial t} \begin{bmatrix} \phi_1 \\ \phi_2 \end{bmatrix} + \frac{1}{r} \frac{\partial}{\partial r} r \begin{bmatrix} 2 & -0.75 \\ 1 & 0 \end{bmatrix} \begin{bmatrix} \phi_1 \\ \phi_2 \end{bmatrix} = 0 \quad (\text{D.5})$$

Here, $\phi_1 = u_1 \delta$ and $\phi_2 = \delta$

Initial conditions for $t = 0$,

$$\phi_1 = 4^5 r^3 (0.5 - r)^2 \text{ for } r \leq 0.5 \text{ and } \phi_1 = 0 \text{ for } r > 0.5$$

$$\phi_2 = 4^2 r (0.5 - r) \text{ for } r \leq 0.5 \text{ and } \phi_2 = 0 \text{ for } r > 0.5$$

Boundary Conditions,

$$r = 0; \phi_1 = 0; \phi_2 = 0$$

D3 Analytical Solution

The analytical solution is based on the method of characteristics. Eqn. (D.5) could be recast as follows.

$$\frac{\partial}{\partial t} \begin{bmatrix} Q \\ A \end{bmatrix} + \frac{\partial}{\partial r} \begin{bmatrix} 2 & -0.75 \\ 1 & 0 \end{bmatrix} \begin{bmatrix} Q \\ A \end{bmatrix} = 0 \quad (\text{D.6})$$

The initial condition for this system of equations would be,

$$Q(r, 0) = 4^5 r^4 (0.5 - r)^2 \text{ for } r \leq 0.5 \text{ and } Q(r, 0) = 0 \text{ for } r > 0.5$$

$$A(r, 0) = 4^2 r^2 (0.5 - r) \text{ for } r \leq 0.5 \text{ and } A(r, 0) = 0 \text{ for } r > 0.5$$

$$\text{Boundary Conditions at } r = 0; Q(0, t) = 0; A(0, t) = 0$$

Diagonalizing Eqn. (D.6),

$$\frac{\partial}{\partial t} \begin{bmatrix} V_1 \\ V_2 \end{bmatrix} + \frac{\partial}{\partial r} \begin{bmatrix} 0.5 & 0 \\ 0 & 1.5 \end{bmatrix} \begin{bmatrix} V_1 \\ V_2 \end{bmatrix} = 0 \quad (\text{D.7})$$

Where,

$$V_1 = -0.5Q + 0.75A \quad ; \quad Q = V_1 + V_2 \quad (\text{D.8})$$

$$V_2 = 1.5Q - 0.75A \quad ; \quad A = 2V_1 + \frac{2V_2}{3}$$

Initial condition:

$$V_1(r, 0) = -0.5Q(r, 0) + 0.75A(r, 0) \quad (\text{D.9})$$

$$V_2(r, 0) = 1.5Q(r, 0) - 0.75A(r, 0)$$

Analytical solutions for Eqn. (D.7) is given by,

$$V_1(r, t) = V_1(r - 0.5t, 0) \quad ; \quad V_2(r, t) = V_2(r - 1.5t, 0) \quad (\text{D.10})$$

Thus the solution for Eqn. (D.6) is given by,

$$Q(r, t) = -\frac{1}{2}Q(r - 0.5t, 0) + \frac{3}{4}A(r - 0.5t, 0) + \frac{3}{2}Q(r - 1.5t, 0) - \frac{3}{4}A(r - 1.5t, 0) \quad (\text{D.11})$$

$$A(r, t) = -Q(r - 0.5t, 0) + \frac{3}{2}A(r - 0.5t, 0) + Q(r - 1.5t, 0) - \frac{1}{2}A(r - 1.5t, 0)$$

Solution for Eqn. (D.5) is given by,

$$\phi_1(r, t) = \frac{Q(r, t)}{r} \quad ; \quad \phi_2(r, t) = \frac{A(r, t)}{r} \quad (\text{D.12})$$

NOMENCLATURE

Symbol	Description
G	- Gas constant for the material.
H_0	- Latent heat of fusion.
H_1	- Latent heat of vaporization respectively.
R	- Beam radius length scale for lateral distances.
\mathfrak{R}	- Curvature of the solid-liquid interface.
T	- Temperature in the solid.
T_1	- Temperature at the top of the liquid layer.
T_0	- Temperature at the bottom of the liquid layer.
\bar{T}	- Average temperature in the liquid layer.
T_b	- Boiling temperature of the liquid.
T_ℓ	- Temperature in the liquid layer.
T_∞	- Ambient temperature.
V	- Drilling velocity scale value.
$V_{\ell v}$	- Normal velocity of the liquid-vapor boundary.
c	- Thermal capacity of the solid.
c_ℓ	- Thermal capacity of the liquid.
g_x	- x component of the gravitational force in the boundary fitted coordinates.
h	- Newton law of cooling coefficient.

$k(T)$	- Thermal conductivity of the solid dependent on temperature.
k_ℓ	- Thermal conductivity of the liquid.
p	- Dynamic pressure in the liquid.
p_a	- Atmospheric pressure.
\tilde{q}	- Laser flux.
q_L	- Heat flux from the liquid layer.
r	- Radial axis in the cylindrical coordinate system.
$s(t)$	- Length of the solid-liquid interface
\dot{s}	- Time derivative of the length of the interface
t	- Time.
u	- Lateral velocity in the liquid layer in the boundary fitted coordinates.
u_1	- Velocity at the top of the liquid layer
u_n	- Normal velocity of the solid-liquid.
v	- Perpendicular velocity in the liquid layer in boundary fitted coordinates.
v_0	- Normal velocity of the liquid relative to solid-liquid interface.
\tilde{v}_1	- Normal velocity of the liquid relative to the liquid-vapor interface.
x	- Lateral axis in boundary fitted coordinate system on the solid-liquid boundary.
y	- Perpendicular axis in the boundary fitted coordinate system on the solid-liquid boundary.
z	- Symmetry axis in the cylindrical coordinate system.

Greek	Description
--------------	--------------------

Symbols	
----------------	--

Φ	- Dissipation function
α	- Angle the tangent to the solid-liquid interface makes with z-axis direction.
δ	- Thickness of the liquid layer.
ε	- Length scale for liquid layer thickness.
ϕ_j	- Primary variables in the Space-Time method, where $j = 1, 3$
φ	- Independent variable of the immobilization transformation
κ	- Thermal diffusivity of the solid.
κ_ℓ	- Thermal diffusivity of the liquid.
μ	- Dynamic viscosity of the liquid.
ν	- Kinematic viscosity of the liquid.
θ	- The angle laser flux vector makes with the normal to liquid-vapor interface.
ρ	- Density of the solid.
ρ_ℓ	- Density of the liquid.
τ	- Pulse length of the laser for time scale.

REFERENCES

1. Abramowitz, M., Stegun, I. A., Hand Book of Mathematical Functions, (1970).
2. Afanas'ev, V. and O. N. Krokhin, "Vaporization of Matter Exposed to Laser Emission", Soviet Physics JETP, Vol. 25, pp. 639 (1967).
3. Allmen, V., "Laser Drilling Velocity in Metals", J. Appl. Physics, Vol. 47, pp. 5460 (1976).
4. Anderson, D. A., Tannehill, J. C. and R. H. Pletcher, Computational Fluid Mechanics and Heat Transfer, Hemisphere Publishing Corporation, New York, (1984).
5. Andrews, G. and D. R. Atthey, "On the Motion of an Intensely Heated Evaporating Boundary", J. Institute of Mathematics and Its Applications, Vol. 15, pp. 59 (1975).
6. Anisimov, S., "Vaporization of Metal Absorbing Laser Radiation", Soviet Physics JETP, Vol. 27, pp. 182-183 (1968).
7. Anisimov, S. and A. K. Rakhmatulina. "The Dynamics of the Expansion of a Vapor when Evaporated into a Vacuum", Soviet Physics JETP, Vol. 37, pp. 441 (1973)
8. Atkinson, K., Elementary Numerical Analysis, John Wiley & Sons, New York, (1993).
9. Banerjee, P.K and Butterfield, R., Boundary Element Methods in Engineering Science, McGraw Hill, London, 1981.
10. Bass, M., Laser materials processing, North-Holland publishing company, (1983).
11. Batteh, J. J., Chen, M. M. and Mazumder, J., "A Stagnation Flow of Keyhole Formation in Laser Drilling", Proceedings of the ASME Heat Transfer Division – 1998: Vol. 4 – Heat Transfer in Material Processing. Ed. Nelson, Jr., R. A. and Chandra, U., pp 29-37.
12. Batteh, J. J., Chen, M. M. and Mazumder, J., "Integral Analysis of the Heat and Momentum Transfer in Laser Drilling", Proceeding of ICALEO 1999, Vol. 87, pp. C31-C40 (1999).
13. Beck, J. V., Cole K. D., Haji-Shaikh, A., Litkouhi, B., Heat Conduction Using Green's Functions, Hemisphere Pub. 1992.

14. Beskos, D. E. (ed), Boundary Element Methods in Mechanics, North-Holland Pub., Amsterdam, (1987).
15. Bhatnagar, P. L, Groos, E. P. and Krook, M., “Model for Collision in Gases, I”, *Physics Review*, Vol. 94, pp 511 (1954).
16. Brebbia, C. A., Telles, J. C. F. and Worbel, L. C., Boundary Element Techniques Theory and Applications in Engineering, Springer-Verlag, Berlin, (1984).
17. Brebbia, C. A., Topics in Boundary Element Research Volume 5 - Viscous Flow Applications, Springer-Verlag, Berlin, pp. 93 (1989).
18. Chan, C. L. and Mazumder, J., “One-dimensional Steady-State Model for Damage by Vaporization and Liquid Expulsion Due to Laser-Material Interaction”, *Journal of Applied Physics*, Vol. 62, No.11, pp. 4579-4586 (1987)
19. Chan, C. L., “Transient 1-D Laser Drilling Model with Variable Properties”, *Proceeding of ICALEO 1999*, Vol. 87, pp. C21-C30 (1999).
20. Chang, S. C., “The Method of Space-Time Conservation Element and Solution Element – A New Approach for Solving the Navier-Stokes and Euler Equations”, *Journal of Computational Physics*, Vol. 119, pp. 295-324 (1995).
21. Crapper, G. D., Introduction to water waves, John Wiley and Sons, New York, (1984).
22. Curran, D. A. S., Lewis, B. A. and Cross, M., “A Boundary Element Method for the Solution of the Transient Diffusion Equation in Two Dimensions”, *App. Math. Modeling*, 10, pp. 107-113 (1986).
23. DeSilva, S. J., Chan, C. L., Chandra, A. and Lim, J., “Boundary element method analysis for the transient conduction – convection in 2-D with spatially variable convective velocity”, *App. Math. Modeling*, 22, pp. 81-112 (1998).
24. Fleuries, J. and Predeleanu, M., “On the Use of Fundamental Solutions in BEM for Thermoelastic Problems”, *Eng. Analysis*, 4, pp. 70-77 (1987).
25. Gradshteyn, I. S. and Ryzhik, I. M., Table of Integrals, Series and Products, Academic Press, Inc. (1980).
26. Hirsch, C., Numerical Computation of INTERNAL AND EXTERNAL FLOWS Volume 2: Computational Methods for Inviscid and Viscous Flows, Wiley, New York (1998).

27. Hassanein, A. M., Kulcinski, G. L. and Wolfer W. G., "Surface Melting and Evaporation During Disruptions in Magnetic Fusion Reactions", Nucl. Eng. Design/Fusion, Vol. 1, pp. 307 (1984).
28. Knight, C. J., "Theoretical Modeling of Rapid Surface Vaporization with Back Pressure", AIAA Journal, Vol. 17, No. 5, pp. 519-523 (1979).
29. Langmuir, I., "The Vapor Pressure of Metallic Tungsten", The Physical Review, Vol. II, No. 5, pp. 329-342 (1913).
30. Mukherjee, S., Boundary Element methods in Creep Fracture, Elsevier Applied Science Pub, Barking, Essex, (1982).
31. Molls, T. and Molls, F., "Space-Time Method Applied to Saint Venant Equations", J. of Hydraulic Engineering, May 1998, pp. 501-508.
32. O'Neill, K., "Boundary Integral Equation Solution of Moving Boundary Phase Change Problems", Int. J. Num. Meth. Eng., 19, pp. 1825-1850 (1983).
33. Ready, F., "Effects Due to Absorption of Laser Radiation", J. Appl. Physics, Vol. 36, pp. 462 (1965)
34. Von Allmen, Martin, Laser-Beam Interactions with Materials Physical Principles and Applications, Springer-Verlag, (1985).
35. Zabaras, N. and Mukherjee, S., "An Analysis of Solidification Problems by the Boundary Element Method", Int. J. Num. Meth. Eng., 24, (1987).
36. Zang, S . and Jin, J., Computation of Special Functions, Wiley, New York (1996).